Experimental and analytical investigation of the aerodynamic noise emitted by generic distributed electric propulsion wing-propellers configurations

Daniel Acevedo Giraldo

ÉCOLE CENTRALE LYON

N° d'ordre NNT: 2024ECDL0015

THÈSE de DOCTORAT DE L'UNIVERSITÉ DE LYON
opérée au sein de l'École Centrale de Lyon

École Doctorale N° 162
Mécanique Énergétique Génie Civil Acoustique

Spécialité de doctorat : Acoustique

Soutenue publiquement le 28/03/2024, par

Daniel Acevedo Giraldo

Experimental and analytical investigation of the aerodynamic noise emitted by generic distributed electric propulsion wing-propellers configurations

---

Devant le jury composé de:

Avallone, Francesco	Professeur	Politecnico di Torino	Rapporteur
Schram, Christophe	Professeur	von Karman Institute	Rapporteur et président
Le Bras, Sophie	Docteure	Siemens PLM Software	Examinatrice
Parisot-Dupuis, Hélène	Docteure	ISAE SUPAERO	Examinatrice
Cotté, Benjamin	Docteur	ENSTA Paris	Examinateur
De Santana, Leandro	Docteur	German-Dutch Wind Tunnels	Examinateur
Roger, Michel	Professeur	École Centrale de Lyon	Directeur de thèse
Jacob, Marc C.	Professeur	École Centrale de Lyon	Co-directeur de thèse
De Laborderie, Hélène	Docteure	Safran Aircraft Engines	Invitée

To my parents, Claudia and Nicolás, my life partner, Paula, and my niece, Macarena.

Acknowledgments

After three years, my PhD research time has ended and undoubtedly it has been one of the most rewarding and unique journeys in my life. From the first, I challenged myself to have a balance between my personal and professional projects but I could not have made it alone. I have many people to thank for their - direct or indirect - invaluable support along this way.

The present investigation has received funding from the European Union's Horizon 2020 research and innovation program under the project ENODISE (ENabling Optimized DISruptivE airframe-propulsion integration concepts), grant agreement No. 860103. This work was performed within the framework of the LABEX CeLyA (ANR-10-LABX-0060) of Lyon University.

First of all, I am deeply grateful to my supervisor Prof. Michel Roger, for allowing me to work on this important project as his last PhD student. Michel, the first time I heard about you was more than five years ago during my master's degree. At that time thinking about working with you was just like a distant dream. Luckily after a while, that dream became a reality and now I can say that it has been a pleasure and an honor for me to work with you. Thank you for sharing with me, throughout this time, your valuable and extensive knowledge with accurate guidance, inspiration, humility, and patience. I will always admire you, more than as a professional, as a person. I wish you all the best in your future endeavors.

Then, I like to thank my co-supervisor, Prof. Marc Jacob, for the valuable support and advice during our internal meetings. Marc, thank you for your positive energy and always having something to contribute to improving my research.

Next, I thank all participants of the ENODISE project for the fruitful technical discussions in our internal project meetings and external conferences. Special thank you to the directors of the project mentioned above, Prof. Christophe Schram and Prof. Julien Christophe from the Von Karman Institute for Fluid Dynamics (VKI), for providing excellent supervision of the project with professionalism, innovative ideas, and deep knowledge. I also thank Hadrien Beriot, Sophie Le Bras, and Korcan Kucukcoskun from Siemens, for our technical exchanges. Your feedback and collaboration have been essential in improving the quality of the analytical work related to this thesis. I am grateful to the German Aerospace Center (DLR) and Delft University of Technology (TUD) for sharing the DRL-F15 airfoil and the XPROP-S propellers, respectively, for our experimental setup. Special thanks also to Maria-Teresa Ramandi for their important and organized administrative support.

I could not leave expressing my greatest gratitude to the permanent staff of the Fluid Mechanics and Acoustics Laboratory (LMFA). The experiments performed in this thesis could not have been possible without the priceless help of the technicians, Jean-Charles Vingiano, Edouard Salze, Emmanuel Jondeau, and Pascal Souchotte. Thank you all of you for the hard work in providing the necessary infrastructure for the development of the experimental part of this research. I am also thankful to Marie-Gabrielle Perriaux for their constant and invaluable administrative assistance.

I also thank Prof. Fernando M. Catalano from the São Carlos School of Engineering of the University of São Paulo for the diffuser design recommendations.

My gratitude to all the staff from Centrale Innovation, especially Emilie Russo. Thank you Emilie for your patience and for going above and beyond for me. Finally, I could have all my French administrative processes finished thanks to you.

My life at the Acoustic Center couldn't have been the same without my colleagues from the LMFA. I feel honored to have worked alongside you, not only the best acousticians in the world but also the kindest people. Thank you all for enriching my time at the lab with unforgettable encounters including early daily lunches, tasty barbecues, amazing outings, sweet Friday cakes, and cheerful conferences.

Now it is the time to thank my parents, Claudia and Nicolás. Mom and Dad, I have many reasons to be grateful to both of you. Thank you from the bottom of my heart for always finding a way to remember me no matter what ambitious my dreams are, I have to follow them regardless of sacrifices and difficulties, and for constantly encouraging me to never give up. Thank you for your unconditional love and support throughout my time away from home. You taught me that love is stronger than distance. I also want to thank you for the strong hugs that always helped me relax and re-energize every time we saw each other after a long time. Lastly, I thank you for the fun Saturday online dinners full of laughter and wine-toasting.

I should also thank my cousin, Ana, and Ronal. Thank you for always waiting for me at the airport when I arrived home, for the worthwhile time you dedicated to me, for the farewell parties too, and of course for making me the happiest uncle. Maca, I have loved you as if you were my niece since before you were born. I will always be by your side to support you in every moment of your life.

I am thankful to my cousin, Yashua, my uncle, Nelson, and Candy. Thank you for always being there for me no matter the situation. I appreciate every Friday we spent laughing together through a video call. Yashua, I am proud of the artist and athlete you are. Remember that I am always just a call away from you.

I also want to thank my hometown friends. Laura, since we moved to different countries some years ago, we have not had the opportunity to share more than online, but fortunately, the friendship is stronger than the last time we saw each other in person. Kevin, you are more than a friend, the brother life gave me. It was always lovely to come back home and spend time with you and Meli in front of delicious food and drinks, just like old times. Thank you all for the joyful moments and for being unconditionally with me.

My thanks to my girlfriend's family too, which soon became my second family. Thank you for the love and for always receiving me as a relative.

Last but not least, I wish to thank my best friend, beautiful girlfriend, and amazing life partner, Paula. When we met, my life completely changed, and your endless love, tender patience, and everyday support quickly became essential for me to overcome the challenges related not only to my PhD life but also to living away from my home country. Thank you for never letting me down and pushing me toward the finish line of this adventure, even with thousands of kilometers in between. I also thank you for everything you have done to be closer to me and for opening the doors of your new place to finish my thesis. I could not have wished for a better person to stand by my side during this journey. The best is yet to come.

"Make of your life a dream, and of a dream a reality."
"Fais de ta vie un rêve, et d'un rêve, une réalité."
Antoine de Saint Exupery

Abstract

The present thesis investigates experimentally and analytically the acoustic installation effects of a pair of six-bladed side-by-side subsonic propellers installed near a wing's trailing edge. In a significant range of low-and-middle frequencies, the propellers' diameter, wing chord, and propeller-wing distance are smaller than the acoustic wavelengths, reaching a compact regime. This generic configuration mimics future Distributed Electric Propulsion urban aircraft architectures, addressed in the framework of the European Union's H2020 project ENODISE. The installation effects refer to the additional sources of aerodynamic noise caused by blade-wing interaction and their scattering by the wing, compared to the case of isolated propellers. This work aims to find an optimum generic configuration concerning aerodynamic and acoustic standpoints through a parametric study. The idea is to demonstrate not only the ability of the experimental approach to determine optimized configurations but also the potential of analytical models to estimate this sound-scattering effect, which is of primary interest for the preliminary design steps of a system. Firstly, wind tunnel tests are performed as a reference. Secondly, an analytical model is implemented and its predictions are validated with the experimental results. Finally, this will help to find interesting options for propulsion-airframe integration.

Wind tunnel tests have been conducted in the anechoic open-jet facility at *École Centrale de Lyon*. Aerodynamic measurements were taken by static pressure taps on the wing, whereas the aero-propulsive performance was evaluated with load cells. In addition, the far-field sound was measured with a rotating microphone antenna, exploring part of a sphere around the setup. The propellers were tested at a constant rate of 7000 rpm in static conditions. Variations in magnitude and directivity of the sound pressure levels at the first blade passing frequency tones were explored comprehensively for the different cases. The spectral content of selected cases of interest was examined in greater detail, showing the impacts of acoustic scattering, diffraction, reflection, and shielding depending on the propeller position. The results show positions at which there is significant potential for noise attenuation by masking both the tonal and broadband noise content. Reductions of up to 5 dB in the overall sound pressure level and 20 dB in the first blade passing frequency were evidenced. Additionally, the data show that the installation effect is crucial for analyzing tonal propeller noise. In particular, sound radiation is significantly increased when the blade tips operate close to the trailing edge. Furthermore, in the analytical formulation, dipole-like noise sources of the propellers are considered, assuming rigid blades. The sound radiation from the propellers is formulated in three dimensions for characteristic spinning modes of tonal noise. In addition, the half-plane Green's function is used to account for the sound scattering by the wing. A finite-chord correction is applied, and validated by numerical simulations. The results confirmed that the installation effect is crucial for analyzing tonal propeller noise. This approach was quantitatively assessed against the far-field wind tunnel sound measurement. Sound pressure maps show that in the presence of the wing, radiation modes that would be evanescent in free-field can be converted into very effectively radiating patterns if the blade tips of the installed propellers are at a compact distance from the wing trailing edge. This effect tends to increase the radiation efficiency of steady-loading noise, which is most often of secondary importance compared to unsteady-loading noise in free field.

Keywords: aeroacoustics, aerodynamic noise, propeller noise, distributed electric propulsion, installation effects, wing-propeller interaction, analytical model, wind tunnel tests.

Résumé

La présente thèse étudie expérimentalement et analytiquement les effets d'installation acoustiques d'une paire d'hélices subsoniques de six pales installées côte à côte et près du bord de fuite d'une aile. Dans une gamme importante de basses et moyennes fréquences, le diamètre des hélices, la corde de l'aile et la distance aile-hélice sont plus petites que les longueurs d'onde acoustiques, atteignant un régime compact. Cette configuration générique imite les futures architectures d'avions urbains à propulsion électrique distribuée, adressée dans le cadre du projet H2020 de l'Union européenne ENODISE. Les effets d'installation se réfèrent aux sources supplémentaires de bruit aérodynamique provoquées par l'interaction pale-aile et à leur diffraction par l'aile, par rapport au cas d'hélices isolées. Ce travail vise à trouver une configuration générique optimale du point de vue aérodynamique et acoustique à travers une étude paramétrique. L'idée est de démontrer non seulement la capacité de l'approche expérimentale à déterminer les configurations optimisées mais aussi le potentiel des modèles analytiques pour estimer l'effet de diffraction du son, qui présente un intérêt primordial pour les étapes préliminaires de conception d'un système. Tout d'abord, des essais en soufflerie sont effectués à titre de référence. Deuxièmement, un modèle analytique est implémenté et ses prédictions sont validées avec les résultats expérimentaux. Enfin, cela permettra de trouver des options intéressantes pour l'intégration propulsion-cellule.

Des essais en soufflerie ont été réalisés dans l'installation à jet ouvert anéchoïque de l'École Centrale de Lyon. Les mesures aérodynamiques ont été faites par des prises de pression statique sur l'aile, alors que les performances aéropropulsives ont été évaluées à l'aide de cellules de pesée. De plus, le bruit en champ lointain était mesuré avec une antenne de microphones rotative, explorant une partie d'une sphère autour de l'installation. Les hélices ont été testées à une vitesse de rotation constante de 7000 tr/min dans des conditions statiques. L'amplitude et la directivité de la pression acoustique aux fréquences de passage des pales ont été explorées de manière exhaustive pour les différents cas. Le contenu spectral de cas sélectionnés a été examiné plus en détail, montrant les impacts de la régénération de son par diffraction ou du masquage en fonction de la position des hélices. Les résultats montrent des positions pour lesquelles il existe un potentiel important d'atténuation du bruit. Des réductions allant jusqu'à 5 dB du niveau de pression acoustique global et 20 dB à la fréquence de passage des pales ont été observées. De plus, les données montrent que l'effet d'installation est crucial pour analyser le bruit tonal des hélices. En particulier, le rayonnement sonore est considérablement augmenté lorsque les extrémités des pales fonctionnent à proximité du bord de fuite de l'aile. De plus, dans le cadre de la formulation analytique, les sources de bruit de type dipolaire des hélices sont prises en compte, en supposant des pales rigides. Le rayonnement sonore des hélices est formulé en trois dimensions, en s'appuyant sur la notion de modes-sources pour représenter le bruit tonal. Par ailleurs, la fonction de Green du demi-plan a permis de prendre en compte la diffraction du son par l'aile. Une correction de corde finie a été appliquée et validée par simulations numériques. Les résultats ont confirmé que l'effet d'installation est crucial pour analyser le bruit tonal. Les calculs ont été comparés favorablement aux mesures du bruit en soufflerie en champ lointain. Les résultats montrent qu'en présence d'une aile, des composantes du bruit évanescentes en champ libre peuvent être converties en modes de rayonnement très efficaces si les sources sont à une distance compacte du bord de fuite de l'aile. Ceci redonne de l'importance au bruit de charge stationnaire, le plus souvent d'importance secondaire en champ libre par rapport au bruit de charge instationnaire.

Mots clés: aéroacoustique, bruit aérodynamique, bruit d'hélice, propulsion électrique distribuée, effets d'installation, interaction aile-hélice, modèle analytique, essais en soufflerie.

List of Figures

List of Tables

Nomenclature

Acronyms

AC	Alternating Current
AFRC	Armstrong Flight Research Center
BEMT	Blade Element Momentum Theory
BLH	Blade-Loading Harmonics
BLI	Boundary-Layer-Injection
BLS	Boundary-Layer Separation
BP	Bottom Propeller
BPF	Blade-Passing Frequency
BVI	Blade–Vortex Interaction
BWB	Blended-Wing-Body
BWI	Blade-Wake Interaction
CCLD	Constant Current Line Drive
CFD	Computational Fluid Dynamics
COR	Co-Rotating
CP	Ceramic-printed Propeller
CROR	Contra-Rotating Open Rotor
CTA	Constant Temperature Anemometer
CTOL	Conventional Take-Off and Landing
CTR	Counter-Rotating
DC	Direct Current
DEP	Distributed Electric Propulsion
DLR	German Aerospace Center
DP	Distributed Propulsion
ECL	École Centrale de Lyon
ENODISE	ENabling Optimized DISruptivE airframe-propulsion integration concepts
EU	European Union
FE	Finite-Element

FEM	Finite-Element Method
GDP	Gross Domestic Product
GRC	Glenn Research Center
HE	Hybrid Electric
$HEIST$	Hybrid-Electric Integrated Systems Testbed
HWA	Hot Wire Anemometry
$ICAO$	International Civil Aviation Organization
$IEPE$	Integrated Electronic Piezoelectric
LBL	Laminar Boundary-Layer
LBM	Lattice Boltzmann Method
LCD	Liquid Crystal Display
LE	Leading Edge
LES	Large-Eddy Simulation
$LFMA$	Fluid Mechanics and Acoustics Laboratory
MP	Metal Propeller
$MSLA$	Masked Stereolithography
$NACA$	National Advisory Committee for Aeronautics
$NASA$	National Aeronautics and Space Administration
$NEAT$	NASA Electric Aircraft Testbed
NF	No Flow
NI	National Instruments
NS	Navier-Stokes
$OASPL$	Overall A-weighted Sound Pressure Level
PAI	Propeller-Airframe potential/viscous Interactions
$PEGS$	Propulsion Electric Grid Simulator
PS	Pressure Side
PSD	Power Spectral Densities
PXI	PCI eXtensions for Instrumentation
$RANS$	Reynolds-Averaged-Navier-Stokes
RMS	Root-Mean-Square
RPM	Revolutions Per Minute

SLA	Stereolithography
SPL	Sound Pressure Level
SS	Suction Side
SST	Shear Stress Transport
$STOL$	Short Take-Off and Landing
TBL	Turbulent Boundary-Layer
TE	Trailing Edge
$TEDS$	Transducer Electronic Data Sheet
TP	Top Propeller
TRL	Technology Readiness Levels
TUD	Delft University of Technology
UAM	Urban Air Mobility
UAV	Unmanned Aerial Vehicle
UV	Ultraviolet
VKI	von Karman Institute for Fluid Dynamics
VS	Vortex Shedding
$VTOL$	Vertical Take-Off and Landing
$WALE$	Wall-Adapting Local Eddy-viscosity
WHO	World Health Organization

Greek characters

α	Angle of attack	deg
α_d	Dipole angle	deg
α_h, α_t	Blade angle of attack at the hub and tip	deg
α_j	Local angle of attack	deg
β	Compressibility parameter	$-$
γ	Blade pitch angle	deg
γ_j	Local stagger angle	deg
κ_t	Kinetic energy	J
λ	Acoustic wavelength	m
λ_r	Local speed ratio	$-$

ν	Kinematic viscosity	m^2/s
Ω	Rotational speed	rpm
ω	Angular frequency	rad/s
Ω_s	Azimuthal phase velocity	rpm
ω_t	Turbulent dissipation	m^2/s^3
ϕ	Propellers offset angle	deg
ϕ_a	Relative angle deviation	deg
ϕ_{obs}	Observer and source angles	deg
ρ	Mass density of the fluid	Kg/m^3
σ_r	Local solidity ratio	–
θ_e	Diffuser conical expansion angle	deg
θ_{obs}, θ_0	Observer and source angles	deg

Latin characters

$\bar{r}$	Distance between the observer and source	–
a, a'	Axial and angular induction factors	–
A	Diffuser cross-section area	m^2
B	Number of blades	–
b	Span length	–
b_s	Segments per blade	–
C	Airfoil chord	m
c	Blade chord	m
c_0	Sound speed	m/s
C_D	Drag coefficient	–
c_j	Blade segment chord	m/s
C_L	Lift coefficient	–
C_P	Pressure coefficient	–
D, d, h	Propellers parametric variations	m
D_b	Drag	N
D_h	Hydraulic diameter	m
E_t	Engineering target accuracy	–

e_X, e_Y, e_Z	Propellers coordinate system	–
e_x, e_y, e_z	Wing coordinate systems	–
f	Frequency	Hz
F_0	Steady-state force component	m
F_s	Blade-loading harmonic	–
F_t, F_d	Dipole strength and amplitude	–
f_{max}	Maximum frequency of interest	Hz
$G_{1/2}^{(0)}$	Half-plane Green's functions without flow	–
$G_{1/2}^{(M_0)}$	Half-plane Green's functions with flow	–
h_d	Diffuser height	m
J	Advanced ratio	–
j	Induced speed on the blade segment	m/s
J_n	Bessel function	–
K, k	Corrected and normal wavenumber	–
K_1^*	Modified Bessel function	–
K_B	Wavenumber at BPF	–
L_b	Lift	N
L_d	Diffuser length	m
m	Blade-passing frequency order	–
M_0	Axial-flow Mach number	–
M_t	Tangential Mach number	–
n	Mode order	–
N_s	Number of segments per wavelength	Hz
$P_{1/2}^{(0)}$	Acoustic pressure field	–
p_{rms}	Sound pressure	Pa
Q	Torque	N
R	Green's function distance variable	–
r	Blade radius	m
R'	Source-to-observer distance	m
r_0	Distance of a point dipole to the edge	m
r_h	Hub blade radius	m

r_j	Mid-span radius of the blade segment	m
r_t	Tip blade radius	m
r_{obs}, r_0	Observer and source radial positions	m
R_{obs}	Observer radial positions	m
Re	Reynolds number	$-$
S	Classical Sears' function	$-$
s	Blade-loading harmonic order	$-$
T	Thrust	N
t	Time	s
T_B	Blade-passage period	$1/Hz$
u_0, u_1	Upper bounds of the Green's function integrals	$-$
U_0	Flow velocity far upstream	m/s
U_0^p	Phase speed	m/s
U_∞	Flow velocity far downstream	m/s
U_{ind}	Induced velocity	m/s
U_{rel}	Relative fluid speed	m/s
u_{rms}	Turbulent velocity	m/s
v_i	Induced speed	m/s
Vr	Absolute velocity downstream	m/s
w_d	Diffuser width	m
$W_{1,2}$	Relative velocities upstream and downstream the blade	m/s
$w_{a,t}$	Axial and tangencial velocity variation	m/s
w_s	Total velocity variation	m/s
X_{obs}, X_0	Observer and source vectors with corrected streamwise coordinate	m
x_{obs}, x_0	Observer and source streamwise positions	m
Y^+	Dimensionless wall distance	$-$
Y_t	First element thickness	m
y_{obs}, y_0	Observer and source positions	m
z_{obs}, z_0	Observer and source positions	m

Contents

1 Introduction

Summary

This chapter introduces the main topic of the research. Due to the necessity of reducing noise and gas emissions while the civil aviation industry continues its growth, a new class of air transport vehicles for Urban Air Mobility (UAM) emerged as a solution for this environmental emergency by integrating electric propulsion systems with the aircraft's airframe. First, section 1.1 presents the background of the novel aircraft concepts and the aspect that makes them unique for future propulsive architectures. The motivation for this investigation and its objectives are explained in section 1.2. Finally, section 1.3 outlines the structure of the manuscript.

Contents

1.1 Novel Aircraft Concepts in Civil Aviation

1.1.1 Current State of Aircraft Noise and Gas Emissions

In the last decades, the constant growth of the aviation industry for satisfying the ever-increasing travel demands has made it become one of the most important worldwide transport industries supporting 4.1% global Gross Domestic Product (GDP) [1]. It is expected to increase shortly as traffic forecast for civil aviation is confirmed to double in the next 15 years with a 4.3% average traffic growth p.a. [2, 3]. In turn, while individual aircraft have become 75% less noisy since the first jets in the 1950s due to technological improvements, the growing air traffic means that an important part of the population is still exposed to problematic noise levels. For example, in the European Union (EU), aircraft noise is the third most significant source of noise exposure after road and rail traffic. At the same time, although aircraft emissions per seat kilometer have decreased by 80%, greenhouse gas emissions from aviation in the EU have more than doubled since 1990, becoming increasingly significant and being the second most important source of transport emissions after road traffic [4]. As a result, international institutions have set quantitative goals for limiting perceived noise and pollution to be fulfilled by future aviation. Specifically, the goals for 2050, relative to the capabilities of typical new aircraft in 2000, are to reduce by 65% the perceived noise emission of flying aircraft and by 75% and 90% CO2 and NOx emissions, respectively, per passenger kilometer [5, 6]. Consequently, the need for environmentally responsible solutions

in aircraft technology has now come to the forefront of global challenges due to community noise and chemical emissions produced by conventional aircraft. Therefore, developing highly innovative concept technologies is essential to guarantee the sustainable development of the air transportation system.

In parallel with the increasing growth of civil air transport, the recent advance in electric and hybrid-electric power plant technology has generated strong interest in aviation due to its economic and environmental potential advantages. Those aircraft promise significant benefits for local air quality, as the CO2 and NOx pollutants emitted during the fuel combustion process are avoided, and noise levels will not have some noise sources, such as combustor, turbine, and jet noise [7]. Because of this, new innovative electric and hybrid-electric aircraft technologies for aviation are developing quickly. Unlike in the past, where aircraft layout and its propulsion system were seen as two different design threads, most of the new aircraft present unconventional characteristics by coupling these two areas into a unique subject [8, 9]. The fulfillment of the 2050 objectives in terms of noise and gas emissions for ensuring improved mobility while protecting the environment will not be achieved without the introduction of radically new ideas. Furthermore, those new sources must be specifically addressed to assess better the gains of evolutionary and disruptive architectures in noise reduction. Consequently, many ongoing projects have been identified globally, ranging from large commercial aircraft to general aviation, *e.g.*, business or regional aircraft, showing the complexity of the aerodynamic and acoustic interactions, affecting both aerodynamic performance and noise emissions, compared with conventional aircraft designs [10, 11, 12].

1.1.2 Summary of New Electric Aircraft Concepts

As seen in Figure 1.1, new conventional air transport aircraft are shown on the left side, whereas the right side displays novel concepts for on-demand UAM. The common denominator of all those concepts is the formidable complexity of the aerodynamic and acoustic interactions, affecting both aerodynamic performance and noise emissions compared with conventional tube-and-wing aircraft.

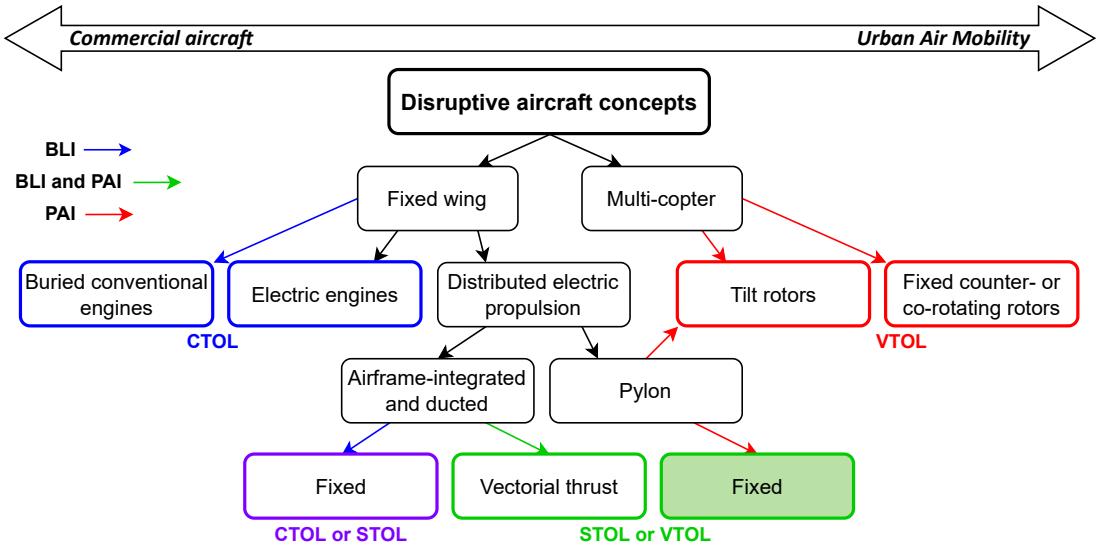

Figure 1.1: Disruptive aircraft concepts [13]. The green background concept is the one investigated in the present thesis.

The non-conventional Blended-Wing-Body (BWB) aircraft seems to be one of the most promising concepts for future subsonic commercial aviation. Conceptually, the novel configuration is aerodynamically compared to the conventional aircraft, *i.e.*, a wing attached to a cylindrical fuselage with a tail that ensures the aircraft's stability and maneuverability [14, 15]. It also has an advantage over the standard configuration, decreasing acoustic impact by using the wing, body, and tail to shield the engine noise from propagating to the ground. Additionally, the BWB layout lends itself well to mounting a Boundary-Layer-Injection (BLI) propulsion system with distributed electric-driven propellers for reducing greenhouse gas emissions [12, 16, 17].

On the other hand, for general aviation, in recent years, the world has seen an unexpectedly fast development of the known UAM concept, which started for naming services between cities and airports using helicopters during the 1940s. Nowadays, UAM represents a disruptive urban/regional air travel technology leading to the development of a new type of aircraft, called electrical Vertical/Short Take-Off and Landing (VTOL/STOL) aircraft, designed for different sectors, such as hobbyists, commercial entities, the military, government agencies, and scientists [18, 19, 20]. The growing interest in UAM aircraft is driven partly by the need for greener air transportation solutions and advancements in batteries, distributed electric propulsion, and autonomous technologies [21]. In addition, these new aircraft are expected to be safer, quieter, and less expensive to operate and maintain than existing VTOL/STOL aircraft, *i.e.*, helicopters, and regional aircraft [22]. Electric propulsion may also result in lower aircraft noise levels, since electric engines will not have some of the noise sources associated with jet or piston engines, such as combustor and turbine noise. Depending on the design of the aircraft, jet noise may be also reduced substantially due to the lower jet speeds required for aircraft operation. The lower noise levels associated with electric aircraft may facilitate its use in densely populated areas [23, 7, 24]. However, in addition to the current aircraft fleet, the UAM is likely to lead to new sources of community noise because of the interactions between propulsive units and airframe [7, 25, 26, 27, 28, 29, 30]. Although the ICAO (International Civil Aviation Organization) does not have specific environmental standards in Annex 16 to cover such aircraft types, for average (day-evening-night-weighted) and night noise exposures, the World Health Organization (WHO) strongly recommends reducing noise levels produced by aircraft below 45 dB and 40 dB, respectively, as aircraft noise above this level features as environmental risks to mental and physical health [31, 32].

One of the most prominent UAM propulsion concepts that seek to meet these aggressive goals and recommended noise levels is the Distributed Electric Propulsion (DEP) system, which relies on thrust generation by multiple fans or propellers installed close to the airframe, such as the propeller-wing configuration which has been extensively studied in terms of aerodynamics but less investigated in terms of noise production [33]. The DEP stands for a specific approach of the more general Distributed Propulsion (DP) concept but with the required electrical power-producing devices, *i.e.*, an electric generator or fuel cell, and energy storage devices, *i.e.*, battery or capacitor, to power the multiple propulsive devices via an electric transmission system, contrasting with the standard mechanical transmission system. Therefore, a DEP system should also enable improvements in efficiency, capabilities, or performance of the air vehicle regarding the system level of classical propulsion systems. In addition, some aircraft have multiple independently electrically driven small propulsors for safety and flight control purposes [10, 34, 35, 36].

In recent years, because of this decoupled feature between the power sources and propulsive devices and the rapid developments in electrical components for aircraft applications, many revolutionary aircraft configurations have been identified as possible only if highly efficient-compact electric machines and transmission systems are employed. However, based on current and near-term electrical limited power or energy density of components and subsystems, most

early adopters of this technology have been found in small aircraft applications. Consequently, because of the enduring interest in increasing efficiency, decreasing operating costs, and encouraging environmental responsibility of larger commercial aircraft applications, several organizations are investing and researching DEP aircraft systems for larger passenger and cargo-carrying capabilities [10, 21].

At NASA (National Aeronautics and Space Administration), many testbed projects address electric power and energy distribution from small-scale to large-transport-class aircraft. To provide a subscale simulation of the entire electric power system, from the turbine engine to the distributed propulsors, the Propulsion Electric Grid Simulator (PEGS) was developed at the NASA Glenn Research Center (GRC) as a desktop experimental testbed [37, 38]. The Hybrid-Electric Integrated Systems Testbed (HEIST) operated at the NASA Armstrong Flight Research Center (AFRC) has also been used to study hybrid-electric DEP hardware integration [39]. Moreover, the NASA Electric Aircraft Testbed (NEAT) platform was developed at NASA GRC to test full-scale electric aircraft powertrain tests. The testbed allows a reconfigurable powertrain architecture and supports a single-aisle aircraft scale geometry. In addition to the NASA testbed development efforts, electric aircraft concepts have been developed, configured, and manufactured worldwide by industry and government research groups for separate applications and markets.

Disruptive aircraft concepts can generally be divided, among others, into conventional, short, and vertical takeoff and landing aircraft (CTOL, STOL, and VTOL, respectively) and Unmanned Aerial Vehicles (UAVs). The electrical aircraft concepts falling into each of these categories will be outlined in the subsequent discussion. Some incorporate BLI propulsion systems, whereas others present Propeller-Airframe potential/viscous Interactions (PAI) or even both simultaneously.

- Notable among CTOL aircraft configurations are NASA's N3-X, N2-B, and STARC-ABL, Airbus E-thrust and E-FanX, ESAero ECO-series, Aurora Flight Sciences' D8, ONERA's NOVA and DRAGON, Alice Commuter, Zunum Aero, and EAG H2ERA. These aircraft, shown in Figure 1.2, have been developed to improve traditional transport aircraft's performance by incorporating BLI, all-electric, or HE (Hybrid Electric) DEP systems into the wings or fuselage.

- In addition, a series of aircraft with STOL capabilities have also been developed as shown in Figure 1.3, where the DEP system is incorporated into the airframe to augment high-lift capabilities at low speed. Two popular examples of STOL aircraft are the aforementioned NASA X-57 Maxwell and ONERA's Ampere.

- Apart from CTOL and STOL aircraft, as shown in Figure 1.4, the VTOL aircraft market has also recently developed as a demand of the near-future urban aerial mobility movement. Several examples of VTOL air vehicles that have been designed for aerial taxi services in crowded urban environments are the CityAirbus, eHang184, Volocopter, Lift HEXA, EMBRAER X-eve, Aurora Flight Sciences' Pegasus, Uber eCRM003, Wisk, Opener BlackFly, Vahana from Airbus, Lilium Jet, Kitty Hawk Heaviside, Joby S2, VA X4, and Bell Nexus 6HX.

- Finally, the XV-24 Lightning Strike and NASA GL-10 also fall into the category of VTOL DEP aircraft, although they are not designed for personal transportation as seen in Figure 1.5.

Each of these configurations is briefly described in the following.

The NASA N3-X concept aircraft uses superconducting electric motors integrated into the upper surface trailing edge of the aircraft center-body region to drive the distributed ducted fans. The power to drive these electric fans is generated by two wing-tip mounted gas-turbine-driven superconducting electric generators, which allows the aircraft to obtain at least a 60% reduction in energy consumption compared to the best in class current generation transport aircraft [40]. The NASA N2-B has three embedded turbofan engines with variable area thrust vectoring/reversing nozzles in each nacelle. Each engine has a gas generator that drives an inline fan and two additional outboard fans through a mechanical transmission system [41]. The N3-X and N2-B configurations have been developed as BWB aircraft, while the following are conventional tube-and-wing airframe configurations.

The STARC-ABL concept is a simplified DEP aircraft configuration actively studied by NASA. This concept features a conventional architecture with two underwing turbofan engines with electric generators used to extract power from the engines and transfer it to a fuselage-mounted BLI electric fan at the aft end of the aircraft resulting in up to a 12% reduction in fuel consumption compared to similar-class aircraft [42]. Airbus proposed a large electric-powered aircraft with hybrid technology called E-thrust. The propulsion system comprises six electrical motors and a centrally placed gas turbine. After reaching cruising altitude, the jet engine is throttled back to where it is only used to generate electricity. The additional source of electricity is then used to power the aircraft's electrical drives, which can be individually switched off at cruising altitude. The E-Fan X was an electric demonstrator aircraft concept developed by Airbus to test the technologies that would help future electric air vehicles. In the test aircraft, one of the four jet engines was planned to be replaced by an electric motor [43]. The D8 "double bubble" aircraft developed by Aurora Flight Sciences merges two aircraft bodies lengthwise and has three turbofan jet engines with an ultra-high bypass ratio on the tail for more efficient thrust [44, 45].

ONERA's NOVA is a concept of medium-haul transport with aft-mounted engines semi-buried in the fuselage for increasing propulsive efficiency with BLI air intake [46, 47]. In contrast, ONERA's DRAGON relies on the distributed thrust via a large number of electric fairings propellers placed under each wing, which improves the propulsive efficiency [48, 49]. The electric motors are powered by electricity generated by turbines located at the aircraft's rear. The turbo-electric ESAero's ECO-150 aircraft concept has eight electric fans and one turbogenerator placed in a split-wing configuration between each wing's upper and lower surfaces. It also presents a cryogenic cooled electrical system [50, 51]. The Eviation Alice is a pure electric commuter aircraft with three motors driving two pusher propellers mounted in its tail. Depending on the model, the energy is stored in a lithium-ion or more powerful aluminum-air battery [52]. Zunum Aero has been working on a hybrid-electric aircraft for the smaller regional market. It has two fuselage-mounted electric propulsors powered by a combined system of a turboelectric generator and batteries. This propulsion system enables a highly efficient and low-cost operation on a conventional airframe [53]. Finally, the H2ERA is a hybrid-electric regional aircraft concept developed by the Electric Aviation Group; it has four propellers on the wings and is expected to have a hydrogen fuel cell-based powertrain for zero fuel emissions [54].

(a) NASA's N3-X

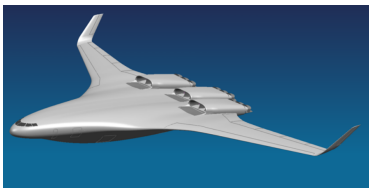

(b) NASA's N2-B

(c) NASA's STARC-ABL

(d) Airbus E-thrust

(e) Airbus E-FanX

(f) Aurora Flight Sciences' D8

(g) ONERA's NOVA

(h) ONERA's DRAGON

(i) ESAero ECO-series

(j) Alice Commuter

(k) Zunum Aero

(l) EAG H2ERA

Figure 1.2: New CTOL aircraft concepts.

Based on the Tecnam P2006T aircraft fuselage, the NASA X-57 Maxwell aircraft stands for a reconfigured model with a much smaller wing than the baseline aircraft. It is equipped with a DEP system of 12 small propellers along the leading edge of the wing. The distributed propellers increment the dynamic pressure, hence the lift, over the wing at low speed. During the takeoff and landing phases, the small propellers provide a high lift, which allows the smaller wing size design. During the cruise segment, two wing-tip-mounted large electric propellers are the main propulsors, whereas the small ones are turned off, providing up to 5 times reduction in energy consumption compared to the original P2006T aircraft [55, 56]. Another aircraft development by ONERA as a general aviation STOL aircraft concept is the Ampere. It features an array of 40 small ducted electric fans powered by a combination of batteries and hydrogen fuel cells. The fans are mounted at the leading edge of the wing's upper surface to provide an upper surface blowing effect to increase the lift at low speed [33].

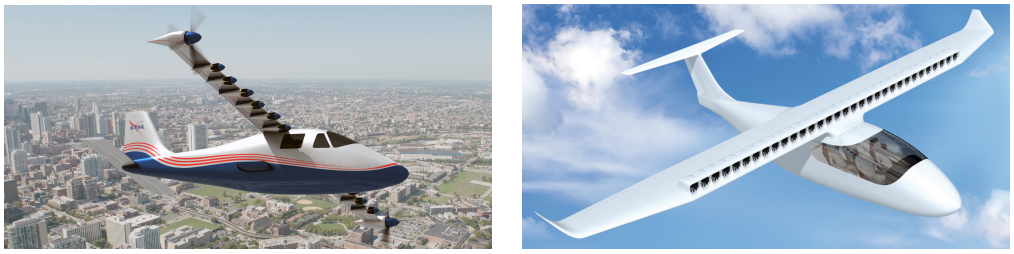

(a) NASA X-57 Maxwell (b) ONERA's Ampere

Figure 1.3: New STOL aircraft concepts.

The CityAirbus [57], eHang184 [58], Volocopter [59], and Lift HEXA [60] configurations are multicopter designs, being the CityAirbus configured with four rotors, the eHang184 with eight, and the Lift HEXA and Volocopter with 18. These configurations can be viewed as an extension of the traditional helicopter or multi-rotor unmanned aerial vehicle approach to vertical flight with the adaptation of multiple smaller rotors enabled by efficient, lightweight electric motor systems. An additional feature of these configurations is that they are entirely battery-powered, ideal for short-range commutes within a crowded city. Unlike these three configurations, some aircraft concepts use different VTOL operation and forward flight rotors to achieve the best trade-off between speed, cost-efficiency, mission performance, and energy consumption. For example, the electrical EMBRAER X-eve [61] and Aurora's Pegasus [62] concepts use eight vertically-mounted rotors for VTOL operation; in contrast, for forwarding thrust, they have behind their fuselage, two and one propellers, respectively. Similarly, the Uber eCRM003 [63] uses four Contra-Rotating Open Rotor (CROR) electrical propellers for vertical flight and one conventional rotor for cruise flight.

The all-electric and self-flying Wisk aircraft also use one propeller for horizontal flight; however, they feature 12 independent rotors with only one moving part for vertical take-off and landing [64]. The desire for eVTOL capabilities coupled with improved cruise efficiency over conventional multi-rotor configurations has also led to the development of novel DEP tilt-wing aircraft concepts such as the Opener BlackFly [65], or the Airbus Vahana [66, 67]. In these concepts, the wing with the propulsors mounted on the leading edge rotates from a vertical direction for VTOL operation to a horizontal direction for cruise operation. The Lilium jet is a different aerial taxi aircraft outfitted with 32 electrically powered ducted fans mounted on the wing and canard flap surfaces. For this aircraft, attitude control and the transition between vertical and horizontal flight are performed through the ducted fans' rotation. This unique aircraft does not have a traditional vertical surface to provide yaw stability as in a CTOL configuration; instead, the yaw control is achieved by introducing asymmetric thrust through the DEP system [68].

The Heaviside from Kitty Hawk features a front wing with two propellers, six propellers on the main forward-swept wing, and a fairly conventional empennage. The propellers are all behind the wings and tilt downward for vertical flight[19]. The small-winged Joby S2 aircraft has four leading-edge foldable propellers on the wing and two on the v-tail to transition from hover to forward flight mode [69]. Similarly, the VA X4 aircraft has eight lift rotors, four at the wing's leading edge and four at the trailing edge, being the ones in the leading edge foldable to ensure a fast and efficient transition from hover to cruise [70]. The same concept is used by the Bell-Nexus6HX [71], which also uses six foldable ducted propellers. In this case, Bell is using its experience and knowledge from the first ducted fan aircraft, the Bell X-22, to the V-22 Osprey tiltrotor and the new V-280 Valor tiltrotor aircraft in making the Nexus VTOL aircraft.

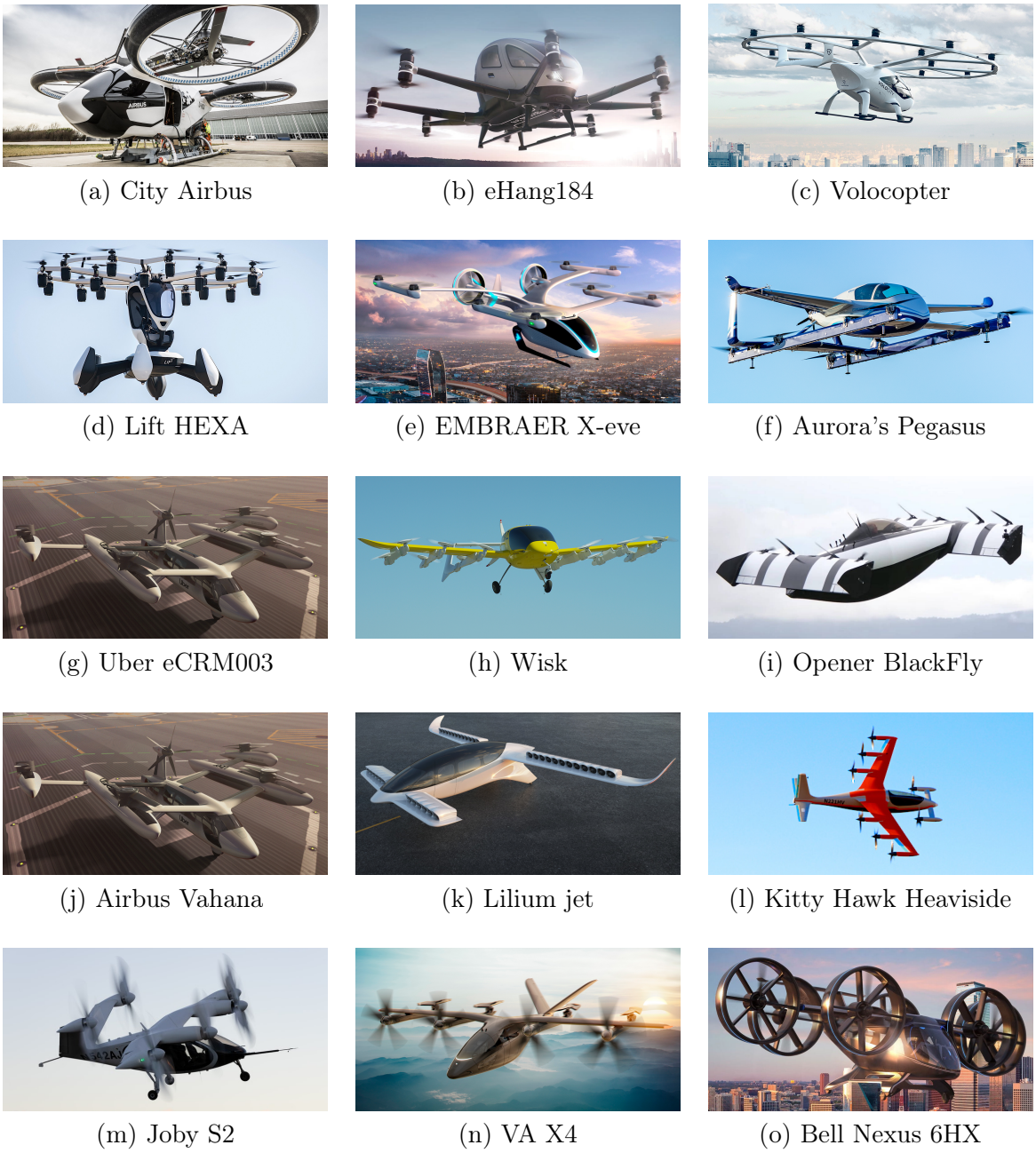

(a) City Airbus (b) eHang184 (c) Volocopter

(d) Lift HEXA (e) EMBRAER X-eve (f) Aurora's Pegasus

(g) Uber eCRM003 (h) Wisk (i) Opener BlackFly

(j) Airbus Vahana (k) Lilium jet (l) Kitty Hawk Heaviside

(m) Joby S2 (n) VA X4 (o) Bell Nexus 6HX

Figure 1.4: New VTOL aircraft concepts.

The Aurora Flight Sciences' LightningStrike is a hybrid-electric vehicle that features a total of 24 ducted fans located between the upper and lower surfaces of the tilting wings and canard [72]. NASA's GL-10 aircraft is a DEP configuration outfitted with ten propellers, eight of which are located across the leading edge of a tilting wing and two on the horizontal stabilizer [73].

(a) Aurora XV-24 Lightning Strike

(b) NASA GL-10

Figure 1.5: New UAV aircraft concepts.

1.1.3 Unique Features of Electric Aircraft

As explained before, the DEP concept utilizes a distribution of electrically powered propulsors across the aircraft to provide both the required thrust for flight and additional advantages associated with propulsion-airframe integration. Several DEP testbed and aircraft concepts with the potential to introduce substantial improvements in future air vehicle performance and efficiency have been introduced, including those used for large-scale commercial transports, regional transports, general aviation vehicles for personal mobility, and unmanned aircraft platforms. These aircraft have also been developed across various conventional, short, and vertical take-off and landing operational capabilities.

Numerous disruptive concepts of DEP are analyzed for their aero-propulsive benefits. One of the advantages of DEP systems is the ability to utilize BLI benefits for improved propulsive efficiency and reduced turbulent kinetic energy losses in the vehicle's wake [74, 75]. Additional benefits include the use of blown surfaces to locally increase dynamic pressure across aerodynamic surfaces and modifications to aircraft-induced drag through interactions between wingtip propulsors and the wing trailing vortex system [10, 34, 35, 36]. A DEP system can also provide new insights to replace or augment control capabilities provided by traditional control surfaces, thus reducing the size of traditional empennage surfaces for decreasing the aircraft weight. Ongoing studies are being performed to provide a basic understanding of how tightly integrated propulsors can be used in an aircraft control architecture, given the strong coupling between the aerodynamic performance of a local wing-body surface and the thrust level of an integrated propulsor. DEP systems can also reduce aircraft noise relative to current air vehicles, particularly during the take-off and landing phases. Decoupling the power-generating components of the propulsion system and the thrust-producing components can enable huge effective bypass ratios of the propulsion systems since the electrically-driven propulsors are only electrically connected to power-producing engine cores. These highly effective bypass ratio systems can substantially reduce vehicle noise. Additionally, strategic placement of propulsors can also be used to take advantage of the noise-shielding effects of wing-body surfaces.

However, apart from the aforementioned DEP advantages and electric power-supply issues, one primary concern with propeller-driven aircraft is their noise emissions. The noise generation mechanisms expected in DEP configurations are divided into tonal noise at harmonics of the so-called Blade Passing Frequency (BPF) [76] (propeller-propeller/-pylon/-wing interaction noise, propeller steady and unsteady loading noise, and thickness noise) and broadband noise [77] (propeller trailing-edge self-noise and propeller-wing interaction noise). Nevertheless, the dominant sources of propeller noise are aerodynamic loading and interaction noise. Therefore, the main challenges inherent to DEP systems include the effects of inflow distortions on propeller efficiency and noise. These effects, of aerodynamic and acoustic nature, will highly depend on the relative

positioning of the propellers on the wing/airframe [78, 79, 80]. The aerodynamic installation effect refers to the interaction of a propeller with mean-flow gradients around the wing and mounting elements, such as pylons, which induces additional aerodynamic noise sources [81, 82, 83]. The acoustic installation effect refers to the scattering of propeller noise by the wing and other surfaces [84, 85, 86, 87, 88]. Both justify dedicated studies to understand, model, and optimize all aspects of propeller-airframe integration, as this new rotating-blade aircraft may imply innovative installation strategies, raising the question of the acoustic signature.

1.2 Motivation and Objectives of the Research

Tighter integration of the propulsion system into the airframe brings both beneficial and detrimental effects. On the positive side, ingesting the airframe boundary layer should, in principle, improve the aircraft's overall performance. Furthermore, one expects that placing the propulsion system closer to the airframe should bring interesting shielding effects, especially if the distance to the airframe can be made small enough compared to the airframe dimensions, leading ultimately to the partly-buried engine concept. The adverse effects concern the structural integrity and possibly noise source reinforcement due to the unsteady loads that result from potential distortion or wake/boundary layer viscous effects. The problem is quite complex, as the blades interact simultaneously with the undisturbed potential flow and the large-scale turbulent boundary layer bringing multiple flow scales into play of the already complicated noise production phenomena. Maximizing the efficiency of the integrated airframe-propulsion system accompanied by minimal noise production rests on the postulate that at least one local minimum does exist. Therefore, interactions between engines and aerodynamic surfaces must be addressed to better assess the gains of evolutionary and disruptive architectures regarding noise reduction.

The diversity of concepts being tested involves complex and largely unexplored aerodynamic and acoustic installation effects, which offer a tremendous opportunity to test disruptive concepts. Noteworthy, such small vehicle platforms show a higher probability of reaching the required maturity to be demonstrated in 2025 than disruptive concepts in civil aviation, where much higher commercial risks are involved. Therefore, the UAM concepts constitute a promising and necessary stepping-stone for the elaboration, validation, and maturation of novel propulsion architectures that should eventually realize their full potential in larger commercial airliners.

Due to the vastness of this field, this research's area of interest needs to be restricted. Therefore, this thesis focuses on the aeroacoustics of rotors in novel aircraft configurations. More specifically, this research aims to analyze and predict the primary sources of propeller noise associated with the propulsion system of novel electrical VTOL/STOL aircraft. A critical issue is the flow distortion induced by a more integrated and distributed propulsion system, causing fluctuating loads on the engine rotor blades that can eventually re-generate noise. These aspects must be balanced against the gains of overall noise emission expected through acoustic shielding. This raises the following questions: what are the flow phenomena influencing the aerodynamic noise of generic configurations of wing-propeller architectures for distributed electric propulsion systems? Furthermore, what is the optimized layout regarding acoustic signature and aerodynamic efficiency?

In past years, prediction methods for computing the noise generated by conventional aircraft have been developed. Nonetheless, new computational approaches are needed to accurately predict the noise radiated by the innovative aircraft configurations because the acoustic signature associated with UAM aircraft might substantially differ from that generated by the ones

of general aviation aircraft [89]. Hence, understanding the new aerodynamic noise generation mechanisms associated with the above-mentioned electric propulsion systems and the availability of computational tools to predict the related noise emissions represents an essential step for developing quieter flying vehicles. At the early stage of development, for instance, when urban authorities have to plan traffic or assess the nuisance, simple and fast prediction tools are needed. At the same time, the main physical features of the sound sources, all related to flow features, must be considered with a minimum realism so that relevant predictions are ensured. Within this context, resorting to analytical models is an attractive approach. However, analytical modeling requires that the dominant sound-generating mechanisms are previously identified, on the one hand, and that simplifications are accepted for mathematical tractability, both on the flow features and the geometry, on the other hand. Furthermore, the models must include design parameters for practical use in optimization algorithms. The theoretical background for such an approach is provided by the acoustic analogy. In parallel, wind tunnel testing is necessary to assess and validate analytical results since experiments provide accurate data, which can help to get an optimum analytical noise prediction tool.

The present work is inscribed in a research framework aimed at improving the understanding and mitigation of noise in DEP configurations through analytical analyses and experimental tests. The generic installed configuration includes a rectangular wing embedded in a mean-flow normal to its edges and a pair of side-by-side propellers in the aft part of the wing. More precisely, the relative wing-propellers' positioning is the main investigated parameter. In addition, the diffraction of propeller noise by the airframe or surrounding surfaces must be explicitly evaluated because it can restructure the sound field strongly. A key aspect to be assessed is that placing the propulsion units over the wing at a quite short distance to its surface is expected to bring the benefit of shielding for observers on the ground [90].

In addition to the steady-loading noise, directly associated with thrust, various interaction mechanisms are expected in the addressed architecture, contributing to the tonal noise. Firstly, the blades interact with the potential field of the pylon, combined with the mean-flow field around the wing. This induces Blade-Loading Harmonics (BLH) on the blades and subsequent tonal noise radiation. For some relative positions, other BLHs are produced as the blade tips cross the boundary layer or the wing wake. The direct field radiated from the blades is scattered by the wing. In particular, the sound is regenerated in the shadow region for masking configurations. Moreover, as the blade tips operate close enough to the wing trailing edge, a possible amplification occurs, as pointed out in previous studies [84, 91, 92]. If the blade tips operate outside the mean-flow gradients of the wing, diffraction of free-field propeller noise is the only remaining effect. The critical question is whether the amplification operates or not, depending on the installation, for moderate wing-propeller distances. Finally, both aerodynamic and acoustic installation effects make a significant sound increase expected as the propeller distance to the plate is reduced. However, which installation effect dominates is probably a matter of combined parameters, which must be clarified.

The main objective of this work is then to understand the flow features and scattering influencing the aerodynamic noise of generic wing-propellers architecture for DEP systems and search for an optimum configuration, both in acoustic signature and aerodynamic efficiency, through a parametric study by changing the relative positioning of the propellers on the wing. To achieve the expected results, some intermediary objectives have been defined:

1. Perform small-scale experiments in an anechoic open-jet facility including a rectangular wing and two side-by-side propellers with adjustable separation, rotational speed, advance ratio, and phasing, positioned at various chord-wise and stream-wise distances from the

wing's trailing edge. This experimental part implies aerodynamic instrumentation and sound measurements using far-field microphones.

2. Develop and implement an analytical model using classical methods for predicting the tonal noise of dipole sources (representing two synchronized propellers) in the presence of the edge of a scattering half-plane (mimicking a wing's trailing edge). This part requires extensions of the scattering model to account for finite-chord effects and comparisons of the predictions with experimental results.

The work described in this thesis is part of the European Union's Horizon 2020 research and innovation program ENODISE (ENabling Optimized DISruptivE airframe-propulsion integration concepts) project [93], which aims to reduce aircraft gas and noise emissions by improving airframe and propulsion system integration. ENODISE is designed as a low-to-mid-TRL (Technology Readiness Levels) enabler project, meant to develop the knowledge, data, tools, and methods necessary to understand, model, and optimize engine-airframe aerodynamic and acoustic installation effects, with a strong focus on innovative architectures bringing a tighter integration of the propulsive system with the wing. Simplified geometrical configurations are investigated to unravel the intricate aeroacoustic mechanisms involved in future aircraft architectures and eventually enable their reliable simulation and optimization while mitigating the adverse effects. Finally, it is important to state that comparisons between small and full-scale DEP systems will be required in the future, as this is not included in project objectives.

1.3 Structure of the Manuscript

This dissertation is divided into seven main chapters. After discussing the context, motivations, and objectives of the research in the present introductory chapter, the rest of this thesis is organized into six additional chapters. In particular, chapter 2 deals with the state-of-the-art of rotor noise and its main underlying mechanisms. The experimental setup is detailed in chapter 3; this chapter describes the propellers-wing model and the wind tunnel facility, as well as the test conditions and acoustic and aerodynamic instrumentation. Then, the key steps of the analytical methodology and mathematical background of the sound-scattering model and noise sources are reported in chapter 4 and chapter 5, respectively. Finally, the main findings of this work and some concluding remarks, along with a summary of future perspectives and recommendations related to the present research are briefly listed in chapter 6. The original contributions of this work depicted in chapter 3, chapter 4 and chapter 5 are based on journal articles and conference papers published by the author throughout as they represent the PhD research activity.

2 State-of-the-art

Summary

The previous chapter introduced a general description of the novel aircraft concept that arose as a solution for the problem of aircraft noise pollution, as well as its unique features that made them acoustically suitable for UAM. This chapter describes the primary noise sources that characterize open rotors/propellers for propulsive systems through a literature review. The chapter is structured as follows. First, the main sources of broadband and tonal noise for open rotors/propellers are described in section 2.1, with emphasis on unsteady loading sources, the ones considered throughout this thesis. Then, section 2.2 briefly addresses some studies regarding propeller noise installation effects resulting from the aerodynamic interaction between the propeller and the airframe. Finally, section 2.3 outlines the propeller noise trends.

Contents

2.1 Propeller Noise Generation Mechanisms

Noise is standard phraseology for undesirable sound, a physical phenomenon detected by the human ear. Then, aircraft noise, defined as the noise perceived by an individual on the ground, is the result mainly of propulsion system noise and airframe noise [94], the latter also known as the "non-propulsive noise of an aircraft in flight" [95]. The contribution of each source to the overall aircraft noise varies in function of the flight phase. Additionally, noise control and

management, which involves low-noise flight procedures and air spatial and ground management, play an essential role in the sound radiated by several sources related to an aircraft [96].

Aerodynamic noise is defined as sound generated directly from relative motion between a solid body or stream of fluid and the surrounding medium. Several industry efforts and investigations have recently addressed the mechanisms by which rotors, *e.g.*, propellers, and fans, produce intense sound [97]. The propeller acoustic signature can be classified into two main categories, namely harmonic noise and broadband and narrow-band random noise. The former occurs from the steady flow over the blades and unsteady periodic interactions, whereas the latter results from time-varying relative disturbances encountered by the blades [98]. The traditionally identified propeller noise generation mechanisms, as well as the additional sources that can be significant, are displayed in Figure 2.1.

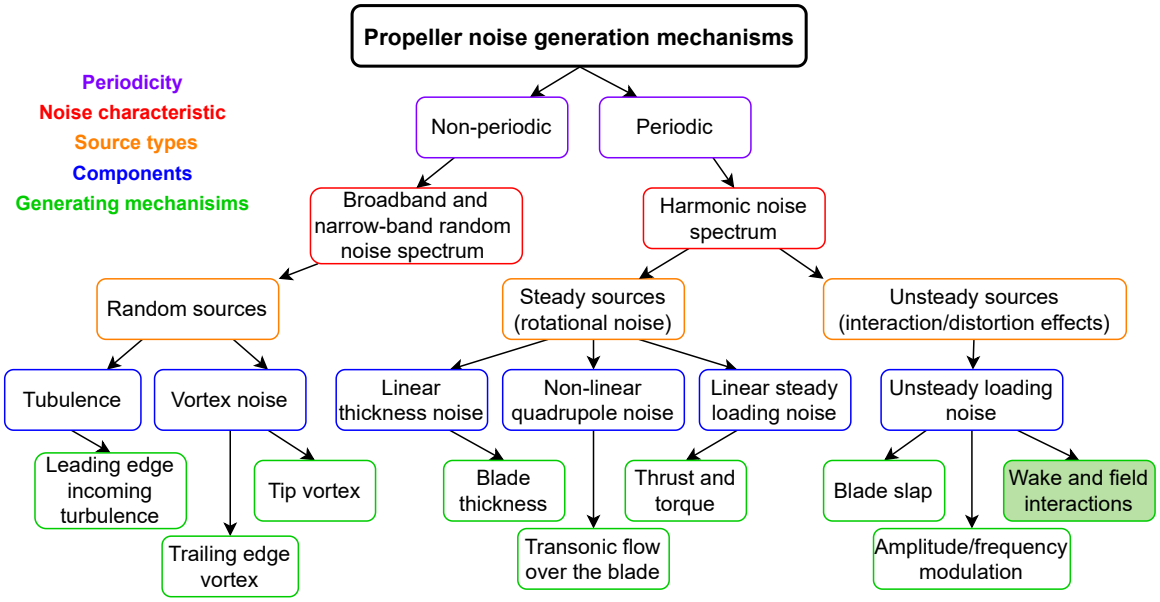

Figure 2.1: Noise generation mechanisms of a typical propeller. Adapted from Hubbard and Kurtz [95, 97]. The green-background noise generation mechanisms are the ones investigated in the present thesis.

Harmonic noise also called tonal noise, is the periodic component represented in the time signature by a pulse that repeats at a constant rate, *i.e.*, strictly at each blade passage. For an observer not rotating with the blades, if a propeller with B blades is operating at constant rotational speed Ω, the resulting noise appears as a signal with the fundamental frequency $f = B\Omega/(2\pi)$ of the tonal noise, also called BPF. The blade-passage period is $T_B = 1/\text{BPF}$. Typically the generated pulse is not purely sinusoidal, so many harmonics exist. These occur at integer multiples of the fundamental frequency, *e.g.* , the first harmonic is the fundamental frequency, the second harmonic occurs at twice this frequency, and so on. Figure 2.2(a) illustrates the characteristics of harmonic noise in both the time and frequency domains.

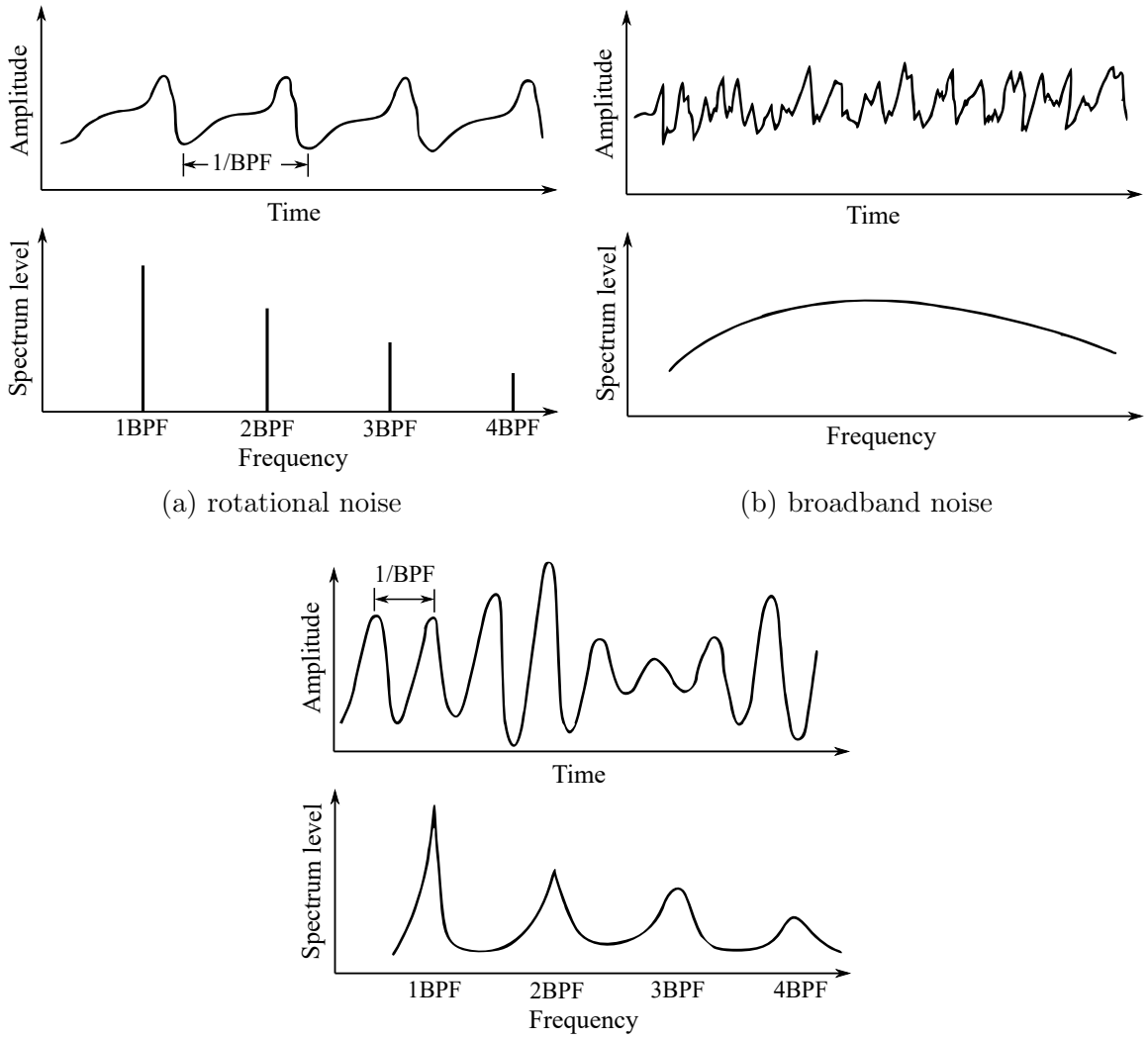

(a) rotational noise

(b) broadband noise

(c) narrow-band random noise

Figure 2.2: Characteristics of propeller noise. Adapted from Hubbard [95].

Contrary, broadband noise has random characteristics and contains components at all frequencies. The frequency spectrum is continuous, with an envelope of arbitrary shape because not all frequencies have the same amplitude. It mostly depends on the quality of the flow ingested by the propeller and on operating conditions. However, the broadband amplitude on the spectrum is most often lower than the tone signal (otherwise, the tones cannot be detected). A typical broadband noise signal is shown in Figure 2.2(b).

Narrow-band random noise is almost periodic. However, the energy is not concentrated at isolated frequencies but rather spreads out as peaks. As shown in Figure 2.2(c), the signal may appear periodic, but specific components do not repeat precisely with time. The frequency spectrum shows finite-width peaks, which possibly spread out increasingly at higher frequencies.

Figure 2.3 illustrates an example of a typical propeller noise spectrum that allows the evaluation of the most important noise source mechanisms. At lower frequencies, the peaks define the tone noise and occur at the blade-passing frequencies whereas in high frequencies the broadband random noise dominates the spectrum. It is worth noting that additional tones are observed

at multiples of the rotational frequency, different from BPF harmonics. This is not included in Figure 2.2 and generally results from blade-to-blade differences, cyclic variations of the rotational speed or dynamic unbalance.

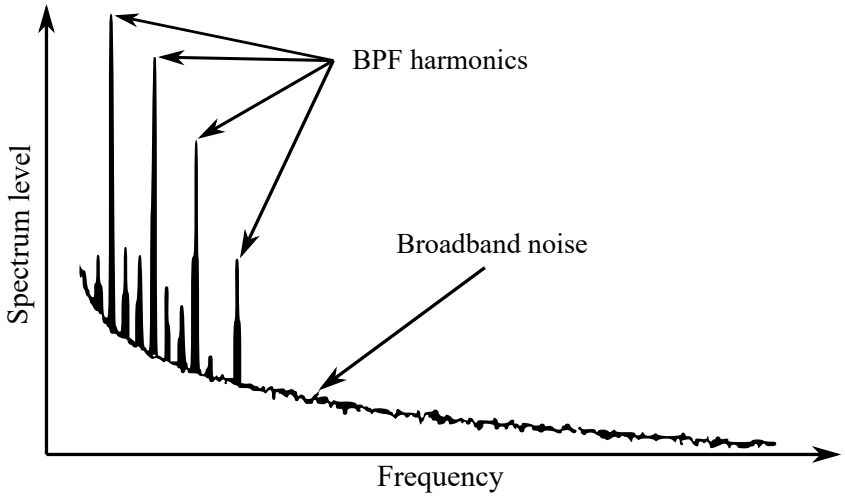

Figure 2.3: Typical spectrum of rotor noise showing harmonics at the blade-passing frequency, broadband noise, and multiple tones at rotational harmonics. Adapted from Glegg and Devenport [99]. Case of a three-bladed propeller.

The mechanisms that lead to the generation of the spectral characteristics discussed above are described in this section. As depicted in Figure 2.1, the noise mechanisms that contribute to the propeller noise spectrum can be classified into three main groups, namely non-periodic random sources and periodic steady and unsteady sources.

2.1.1 Random Sources

Random sources give rise to broadband and narrow-band random noise. The two sources may be important for propellers, depending on the propeller design and operating conditions at which the propeller works. For full-scale propellers in flight, it has been determined that the broadband noise sources are of secondary importance and do not contribute significantly to the total noise [95]. More precisely, broadband noise can become dominant at the higher frequencies for which tonal noise drops.

2.1.1.1 Leading Edge or Turbulence-Impingement Noise

The first broadband noise source is the interaction of inflow turbulence with the blade leading edges, also known as ingestion noise. This turbulence may come from various sources, such as atmospheric turbulence or wake turbulence shed by other rotors or airframe components [19]. Because the inflow is turbulent, the resulting noise is random. Nonetheless, at low frequencies below 1 kHz, this is the dominant broadband source. The importance of this noise source depends on the magnitude of the inflow turbulence, hence it can be quite significant under conditions of high turbulence at low speeds. In principle, leading-edge noise could be reduced by reducing the turbulence integral length scale, if such an action is feasible. As a result, this would also modify the shape of the far-field noise spectrum, with an effective reduction of the noise levels at low frequencies and a general increment of the spectral content at high frequencies [99]. Nevertheless,

this is a significant noise source in several aeronautical applications, such as turbofan engines and rotorcraft configurations undergoing blade-wake interactions.

2.1.1.2 Trailing Edge and Tip Vortex Noise

In the second broadband mechanism, also known as self-noise, noise is generated near the blade trailing edge. A typical propeller develops a turbulent boundary layer over the blade surfaces, resulting in fluctuating blade loading at the trailing edge. The boundary layer properties characterize the noise. A related mechanism occurs at the blade tips, where turbulence in the core of the tip vortex interacts with the trailing edge. At the same time, the vortex can interact with adjacent blades. For a rotor operating in subsonic flow conditions with the homogeneous non-turbulent flow, Brooks *et al.* [100] detailed five airfoil blade self-noise generation mechanisms associated with the interaction between the rotor blade with its self-generated boundary layer and near-wake: turbulent boundary layer trailing edge noise, laminar boundary layer instability noise, boundary layer separation/stall noise, trailing edge bluntness vortex shedding noise and blade tip-vortex noise [101]. The five airfoil blade self-noise generation mechanisms are explained hereafter.

- **Turbulent boundary layer trailing edge (TBL-TE) noise:** trailing edge noise is fundamentally a consequence of the interaction between unsteadiness in the flow and the sharp trailing edge of a blade when the transition from laminar to turbulent states occurs. Turbulence developed in the boundary layers on both sides of the blade is convected past the trailing edge. It is deformed when passing through this region to satisfy Kutta's condition, which accounts for the static pressure continuity at the trailing edge between the upper and lower sides of the blade in such a way that their net sum is equal to zero; hence, the hydrodynamic pressure disturbance convected over the trailing edge is balanced by an additional pressure fluctuation that propagates as sound [100]. Thus, the pressure fluctuations within the turbulent boundary layer are scattered as sound when they pass the trailing edge. Since the boundary layer is now fully developed and characterized by a random and chaotic distribution of vortices of different sizes, the resulting far-field noise spectrum is broadband in nature. Consequently, turbulent boundary layer trailing edge noise is found as the most critical aerodynamic noise source for rotors with larger diameters *e.g.*, wind turbines, and as one of the most relevant broadband noise contributors for propellers and rotors operating in a homogeneous stationary flow [102]. Furthermore, this mechanism is significant at higher frequencies when the inflow turbulence is weaker and increases slowly with the angle of attack.

- **Laminar boundary layer vortex shedding (LBL-VS) noise:** under specific flow and geometric conditions, the boundary layer can remain laminar for a relatively large extension of the blade chord. However, it can also possibly separate, generating a separated shear layer that can reattach as either a laminar or turbulent boundary layer and lead to the formation of a laminar separation bubble [100]. The hydrodynamic instabilities within the laminar boundary layer are amplified coherently in the laminar separation bubble and/or separated shear layer and scattered as sound as they pass the airfoil trailing edge. Then, the resulting acoustic disturbances can travel upstream and trigger the generation of further flow instabilities, reinforcing the sound radiation. Additionally, vortex shedding noise can occur when an LBL exists at least at one side and over most of an airfoil chord. The vortex shedding is coupled to an acoustically excited aerodynamic feedback loop between the airfoil trailing edge and an upstream "source" point on the surface, where Tollmien-Schlichting

instability waves originate. This can significantly increase noise when the laminar separation bubble is sufficiently close to the trailing edge [103]. The resulting noise spectrum comprises quasi-tones related to the shedding rates at the trailing edge with narrowband tones over a broadband hump featuring the corresponding far-field noise spectrum for bi-dimensional airfoils. In particular, the broadband noise is attributed to the scattering of incoherent eddies of different sizes and strengths. In contrast, the tonal noise emissions are related to the scattering of relatively coherent and strong vortical disturbances amplified through the feedback loop. The overall levels of LBL-VS noise could be normalized so that the transition from LBL-VS noise to TBL-TE noise is a unique function of the Reynolds number based on the blade chord [100]. Because it is naturally associated with low Reynolds numbers, this self-noise regime is more likely observed on small rotors or scaled mock-ups for wind-tunnel experiments; when observed, it can be suppressed by appropriate tripping devices.

- **Boundary layer separation/stall (BLS) noise:** stall noise is produced because, at relatively high values of the airfoil incidence, the flow can separate upstream of the trailing edge on the suction side and lead to the formation and shedding of vortices. This phenomenon occurs because the boundary layer is not attached to the airfoil surface when approaching the blade trailing edge. Due to their natural unsteady characteristics, regions of separated flow will produce a large amount of noise. For mildly separated flow, the associated BLS noise signature is quasi-tonal and characterized by a spectral hump at mid-to-high frequencies due to the scattering of relatively small and coherent vortices separating from the airfoil surface, the noise emitted from the trailing edge being dominant. If the angle of attack is increased, the local airfoil section can experience a deep stall condition, with large-scale vortical structures separating from the airfoil surface. As a result, low-frequency stall noise is radiated by the airfoil as a whole [100], being stronger when compared with the TBL-TE noise emitted at low angles of attack [104]. This noise source can be mitigated by operating the blade at conditions away from the stall or through blade pitch control strategies.

- **Trailing edge bluntness vortex shedding noise:** large trailing edge thicknesses produce noise due to the vortex shedding from trailing edge bluntness, similar to the formation of a von Kármán vortex street behind a bluff body. For this, the trailing edge thickness must be large enough compared to the boundary layer displacement thickness. The blunt trailing edge promotes a large-scale vortex shedding within the near wake that is limited to a narrow range of frequencies since the trailing edge thickness determines the dominant turbulent length scale. Consequently, the resulting far-field noise spectrum is quasi-tonal. Due to the large spanwise coherence of the vortices being generated from the blunt trailing edge, the resulting noise can dominate over the turbulent boundary layer trailing edge noise. For rotor blade and wing designs with sharp trailing edges, this noise source is not likely to occur. It can be minimized by designing a trailing edge with a trailing edge thickness to boundary layer thickness ratio below 3.3 under the expected blade operating conditions [100].

- **Blade tip-vortex noise:** tip-vortex noise occurs due to the separated complex three-dimensional flow in this region, associated with the formation of vortices. The randomly oscillating vortical system, characterized by having a thick viscous turbulent core, is generated by the pressure differential between the pressure and suction sides of the blade tip. The associated turbulent structures interact with the trailing edge and the tip, scattering as a strong broadband noise by a mechanism similar to turbulent boundary layer trailing edge noise [100]. However, the tip vortices may be a much more efficient noise source, compared to the trailing edge, since the highest blade velocities are reached at the rotor tip. Tip-vortex noise is more significant at higher angles of attack for wide-chord rotors [101]; nevertheless, it may be reduced by limiting the interaction between the pressure and

suction sides at the blade tip by employing optimal tip shapes or winglets. In addition, tip vortices may interact with neighboring blades in certain flight conditions and generate extra noise.

2.1.2 Steady Sources

Steady sources are those that would appear constant in time to an observer on the rotating blade producing periodic noise because of their rotation. On propellers, steady sources may result from potential or viscous flow phenomena and are usually divided into linear thickness noise, linear steady loading noise, and non-linear quadrupole noise. Thickness and steady loading sources are linear and act on the blade surfaces even at moderate blade section speed, whereas for transonic flow over the blade sections, non-linear effects can become significant. Note that these sources become unsteady when the rotation varies in time.

2.1.2.1 Thickness Noise

Thickness noise is one of the significant propeller noise sources. It originates from the transverse periodic displacement of the air by the volume of a passing blade element, caused by the finite thickness of the blade. The amplitude of this noise component is proportional to the blade volume, with frequency spectrum characteristics dependent on the shape of the blade cross-section, (*i.e.* airfoil shape) and rotational speed. Thickness noise can be represented by a monopole source distribution over the blade surface and becomes important at high speeds. Thin and swept blade sections are used to control thickness noise, which thus becomes generally smaller than loading noise [97].

2.1.2.2 Loading Noise

Steady loading noise results from the pressure field surrounding each blade during its motion, generating thrust and torque (or lift and drag) components. This pressure disturbance moving in the medium propagates as noise. Indeed, despite aerodynamic loading is steady-state for a frame of reference moving with the blades, it has an unsteady behavior when considering a fixed point in the acoustic medium. The loads produced on a rotating blade will be generated from an oscillating rotating pressure field and its waveform will be determined by the pressure distribution on the blades. A dipole source distribution can model steady loading noise for representing the pressure disturbance. These dipole sources will have a strength equal to the net loading produced by the blade at each location [105]. This noise component depends on the Mach number and the blade number [98]. It is an important mechanism at low to moderate speeds for low blade numbers, with harmonic content at multiple BPFs.

2.1.2.3 Non-Linear Quadrupole Noise

Finally, Non-linear quadrupole noise must also be considered to assess the steady noise sources from a propeller thoroughly. These effects can be modeled with a quadrupole source distribution in the volume surrounding the blades for representing the effect related to the Reynolds stresses [106]. The quadrupoles account for the propagation and viscous effects not covered by

the thickness and loading sources. However, the only practical application of this term to propeller acoustics has been its evaluation in the non-viscous flow close to the blade surface. The quadrupole contribution enhances the linear thickness and steady loading sources at transonic and supersonic blade section speeds. It causes a noise increase for unswept, high-tip-speed propellers and helicopter rotors. For low-speed cases, it can be removed from the modeling for simplification purposes [107]. Quadrupoles are not likely to generate significant broadband noise since the induced flow around a blade is mainly laminar, with the wake and boundary layers as the only significant turbulent regions. Thus, there will be only a tiny region of quadrupoles of randomly fluctuating strength, and its noise will be negligible compared to that produced by force fluctuations [106].

2.1.3 Unsteady Sources

2.1.3.1 Unsteady Loading Noise

Unsteady sources are time-dependent in the rotating-blade frame of reference (*i.e.*, for an observer in a non-rotating frame). They include both periodic (*e.g.* pressure bump resulting from the interaction of propeller blades with the wing) and random (*e.g.* self-induced turbulence or turbulence-blade interactions) loading variations on the blades caused by non-homogeneous-flow conditions. In particular, these loading variations generate propeller interaction noise and are usually due to non-axial flight conditions, installation effects, and/or aerodynamic interactions between adjacent or counter-rotating propellers.

Depending on the source of inflow distortion, the loading change will be once per revolution or several times per revolution. All inflow distortions that are invariant with time result in blade-loading changes that repeat exactly for each blade passage during a propeller revolution. The resulting periodic unsteady-loading noise occurs at harmonics of BPF and significantly affects the overall noise signature. Depending on the circumferential location of the loading disturbance relative to the observer, unsteady-loading noise can add or subtract from the steady-loading noise. The non-axisymmetric circumferential directivity exhibits lobe-peaks and -valleys with the number of lobes dependent on the order of the distortion and unrelated to the number of blades. The most relevant interaction noise generation mechanisms are outlined in the following.

- **Blade–vortex interaction (BVI) noise:** the BVI is the most significant noise source associated with aerodynamic interaction for conventional rotorcraft, such as helicopters and tiltrotor aircraft. For these aircraft, BVI noise is generated by the interaction between the rotor and its own wake, which occurs most strongly during descent and maneuvering flight [19]. As the rotor blades pass near the tip vortices formed by preceding blades, they experience a rapid fluctuation of aerodynamic loads, which results in the radiation of highly impulsive noise [108]. In addition, since BVI noise is strongly dependent on the relative positions of the blades and the rotor wake, it is susceptible to changes in the operating condition of the rotor. The intensity and directivity of BVI noise are functions of the angle between the tip vortex and the blade azimuth angle during the interaction, which is determined by the rotation speed of the rotor and the true aircraft's airspeed. Additionally, The BVI noise is a function of the "miss-distance" between the rotor disk and the shed tip vortices. BVI is a significant noise source for conventional rotorcraft but can be effectively reduced by carefully controlling its operation. eVTOL aircraft also experience BVI, both from rotors interacting with their own wake and from rotors interacting with the wakes of

upstream rotors, especially during the transition from horizontal to vertical flight modes [19].

- **Rotor-rotor interaction noise:** for distributed electric propulsion vehicles, strong aerodynamic interactions will likely occur between rotors and propellers, at least during some flight phases. These interactions will result in the generation of unsteady loading on the rotor blades and an associated increase in radiated noise. The nature of these aerodynamic interactions depends on the rotor and aircraft configuration, as well as the aerodynamic operating conditions [19].

  For co-axial counter-rotating propellers, the unsteady loading is an important source, not because counter-rotating propellers contain any additional noise sources but because the aerodynamic interference between the two rotors gives rise to high unsteady-loading noise levels which are particularly significant at low flight speeds, such as during take-off and landing. A complex wake, which convects into the rear rotor, is generated by each front rotor blade. This wake consists of downwash and velocity deficits due to the lift and drag on the blades, respectively, and tip vortices [98, 109]. As a result, a sequence of lift pulses is produced on the rear rotor blades. Additionally, the potential field due to blade loading of the rear rotor creates a disturbance that is felt by the aft part of the front rotor blades. The magnitude of this unsteady loading source depends on the loading level on the rear rotor and the spacing between the two rotors. Since the wakes are periodic, the generated noise is also periodic. Suppose the two rotors have the same number of blades and are operating at the same rotational speed. In that case, the steady and unsteady sources are at the same frequencies, and the noise spectra contain only blade-passage frequency harmonics. However, suppose the number of blades of the front rotor is different from that of the rear rotor, or the two rotors operate at different rotational speeds. In that case, the individual interaction components or modes are distinct in the noise spectra.

  Coleman *et al.* [110] states that as the separation distance between the rotors increases, radiated noise initially decreases rapidly. However, this reduction soon diminishes and the noise reaches a minimum for a separation value of 0.5 rotor radii. At close separation distances, the tonal noise of the rotors is dominant, but as this source diminishes rapidly with increasing separation, the broadband noise component tends to increase. This is likely due to the breakdown of the rotor wakes into weakly correlated vortical structures at long wake ages. Similar trends are observed for varying tip Mach numbers and it is found that the separation distance for minimum noise increases along with the tip Mach number. This happens because tonal noise is relatively more pronounced at higher tip Mach numbers for fixed-pitch rotors. Additionally, the thrust increase causes the wake of the upper rotor to convect towards the lower rotor more quickly at higher tip Mach numbers, resulting in a shorter wake age interaction at a given separation distance [19].

- **Blade-wake interaction (BWI) noise:** BWI noise emerges from rotor blades interacting with the wake turbulence surrounding tip vortices generated by the rotor's preceding blades [111]. BWI is most important for helicopters in mild climb conditions. As the climb angle increases, BWI noise is reduced due to the increased miss distance between the vortex and blade. At higher climb angles, self-noise becomes a more critical noise source. As described previously, BVI is often the most significant source during descent, although BWI still occurs in these conditions [19]. Relatively few BWI noise studies have been conducted, especially in the last two decades. While a basic framework for BWI noise prediction has been developed, it remains limited by incomplete knowledge of the turbulent structures of the rotor wake at long wake ages. However, similar noise mechanisms may be essential for electrical VTOL/STOL aircraft due to the high probability of similar prolonged wake age interactions. While characterizing rotor wakes at long wake ages remains challenging, new

experimental methods and computational tools may provide a path toward understanding and predicting this noise source [19].

- **Rotor-airframe interaction noise:** in addition to previous interaction noise contributions, rotor-airframe interaction noise, also known as aerodynamic installation effects, accounts for the noise produced by interaction with distortions around fixed airframe components, such as wings or struts, and the rotating blades, which can generate strong additional unsteady loads [19]. In practical applications, the additional sound generation can be hard to separate from sound-scattering effects induced by the airframe. As this noise generation mechanism is the most relevant to the studies presented in this thesis, the following section 2.2 will describe it in detail. In addition, the most relevant investigations that address rotor-airframe interaction noise will also be shown.

2.2 Propeller Noise Installation Effects Investigations

2.2.1 Experimental Approaches

The aerodynamic sound generated by the small-sized propellers of drones is also extensively investigated by different authors performing experimental tests. For example, aerodynamic interactions of drone propellers in hover as a function of the distance between the rotors [112, 113] as well as their respective generated aerodynamic sounds in horizontal forward flight with negative pitch [76] have recently been investigated. Firstly, the authors found that the proximity of adjacent rotors adversely affects rotor aerodynamic performance because of the tip blade–vortex interaction. Secondly, installation and forward-flight effects generate much more sound than the steady loading on the blades associated with thrust. Additionally, the near-field sound produced by multirotor drones in hover was also assessed [114, 115, 116]. They produce both non-rotor harmonic noise (*i.e.*, motor noise and noise from the speed controller) and main rotor harmonic noise (*i.e.*, propeller thickness noise and loading noise). In this case, the latter can be reduced by replacing the standard main rotor with custom-designed wide-chord multi-bladed propellers.

Few studies have been conducted with co-axial counter-rotating and co-rotating rotors for assessing the aeroacoustic properties due to the aerodynamic interaction between the two propellers and the installation effects because of the mutual interactions between airframe components and the rotors [117, 118, 119]. Noise reductions relative to the baseline design were achieved by increasing the rotor-rotor spacing and decreasing the rear-rotor diameter to minimize the tip-vortex interaction and reduce wake and upstream influence. Furthermore, the impingement of the pylon wake on the blades has a significant dominant effect on the unsteady blade loadings, whereby analytical [120, 121, 122] and numerical [123] methodologies for prediction of the counter-rotating and co-rotating propellers wake-interaction have been developed to predict the main features of the resulting unsteady blade loadings on the rear-rotor blade surface.

Block [124] conducted a study to compare the differences in radiated noise for a single propeller mounted in a tractor configuration upstream of a pylon and in a pusher configuration downstream of the same pylon. Results showed that the pusher propeller configuration generates additional impulsive noise at the higher harmonics of the blade passing frequency. The author attributes this noise increase to the interaction of the propeller with the wake of the non-lifting strut upstream of the pusher propeller. In the tractor configuration, the (downstream) pylon acts only if the distance to the rotor plane is short enough to affect the potential flow deformation induced by the pylon. Similar conclusions were recently found by Stephenson *et al.* [125] as a

result of the same test conducted in the 40- by 80-foot wind tunnel at NASA Ames to conclude that the presence of an upstream body can significantly influence the acoustic emissions of a propeller system.

In addition to the aerodynamic effect airframe components can have on the rotor, Johnston and Sullivan [126] evidenced that the propellers can also induce significant acoustically unsteady loading on fixed airframe components. The authors conducted an experiment where a wing instrumented with microphones was placed in the propeller slipstream. The measured unsteady surface pressures on the wing were correlated to interactions with the propeller blade tip vortices using smoke flow visualization. Impulsive surface pressure fluctuations were observed on the downstream wing upper and lower surfaces. Depending on the wing angle of attack, the surface pressure fluctuations could convect down the wing chord, and they could be in or out of phase by the time they reached the wing trailing edge. Different blade airfoil shapes may be used to reduce the radiation efficiency of these interactions according to Pagano *et al.* [127]. Zawodny and Boyd [128] performed an experiment with a small UAV hover rotor, either isolated or with a downstream rod at various separation distances from the rotor. High-fidelity predictions were also conducted, with excellent agreement between the measured and predicted acoustic pressure time series and levels. The authors concluded that for low tip Mach numbers, most of the stationary-rod noise is generated because of the rotor unsteady loading noise during this interaction. Experiments and calculations were conducted for the rod above the rotor, which showed even higher levels of unsteady loading noise generation by the rod due to the sharpness of the pressure field on the suction side of the rotor blades.

2.2.2 Numerical Approaches

Numerical aeroacoustic analyses of modern propeller geometries have also been conducted, accounting for a baseline setup of a single propeller mounted on a wing [129]. As a result, compared with the baseline configurations, the off-loaded tip design is quieter because of the lower operating RPM (Revolutions Per Minute) and the inboard load displacement. In contrast, the unequally spaced hub design is shown to be slightly noisier, as well as the staggered hub design but exhibits a greater number of spectral peaks, leading to a spread of the acoustic energy over more frequencies, which leads to a new method to estimate the influence of the number of blades on noise contribution [130]. Firstly, it was found that the aerodynamic efficiency is maximized for a propeller with three blades because of combined blade-wake interactions, blade loading, and Reynolds number effects. Secondly, the tonal noise decreases significantly with the number of blades because the rotation speed decreases for equal thrust, whereas the broadband noise increases due to enhanced blade-wake interactions. Consequently, there is a trade-off between aerodynamic and acoustic performances, because they do not follow similar trends.

More recently, Lim [131] evaluated the aerodynamic interactions between a wing and the tiltrotor rotor of the XV-15 numerically. The wing was found to generate unsteady loading on the rotor through two mechanisms, one related to the circulation of the wing and the other related to the displacement of fluid around the wing. In addition to the unsteady loading on the rotor, Lim's high-fidelity calculations also showed that the rotor generated impulsive unsteady loading on the wing. Although the wing does not generate noise as efficiently as the rotor due to the lack of convective amplification, the high magnitude of unsteady loading combined with the large surface area of the wing could result in significant noise generation. Following this work, Zhang, Brentner, and Smith [132] used mid-fidelity aerodynamic models to show that this unsteady loading noise could dominate overall sound pressure levels upstream and downstream of the rotor.

2.2.3 Analytical Approaches

A relevant strategy suited to the analytical investigation of innovative propulsive architectures is to define generic configurations in which a propeller and an adjacent scattering surface are typically associated. For mathematical tractability, the surface must be easily defined by iso-values of a coordinate system in which the Helmholtz equation is separable. It must also remain compatible with the assumption of a uniform base flow, apart from the superimposed distortion. Various classes of such generic problems can be defined, all based on the fundamental wave equation of the analogy, that can be solved with suited Green's functions. Each mimics a given architecture or part of it.

The very-low frequency test case of a small-scale propeller operating close to a rigid cylinder, recently addressed by Cros *et al.* [133], is a particular example of a strong installation effect that was evidenced. The test was performed with a three-bladed model propeller, the axis of which was parallel to the cylinder axis. The free-field tonal noise of the propeller was found to increase by about 15 dB as the propeller approached a very short distance to the cylinder in such a way that the global area encompassing the propeller and the cylinder cross-section remained acoustically compact. The aerodynamic installation effect, namely the production of BLH due to the formation of mean-flow distortions, could be considered negligible in this case; thus, the measured increase was attributed to the acoustic installation effect. Indeed it was recovered by a proper asymptotic expansion of the cylinder Green's function, assuming the same sources on the blades. The effect is related to what is referred to as the "compact" Green's function by Howe [134].

Smith *et al.* [135] analytically investigated how to reduce the noise of a single open rotor by changing the blade number or tip speed through a parametric study. The authors reported that the noise levels could be significantly reduced generally by increasing the number of blades and reducing the tip speed.

Further analysis of the installation effect for two counter-rotating side-by-side propellers installed on a wing has been presented by Roger [136]. The results indicate that more benefit is expected from masking by the wing than from synchronization of the propellers. Indeed the latter operates optimally for isolated modes and tones and can lead to reinforcement for other modes/tones. However, scattering by the trailing edge can regenerate sound in the geometric shadow region if the natural directivity lobe of a mode impinges on the edge. This situation can be avoided by placing the propeller sufficiently far upstream of the edge because the main lobe is quite close to the propeller plane. Additionally, the installation above the wing also induces periodic interactions with the boundary layer, generating additional unsteady-loading noise.

2.2.4 Research Gap

All previous investigations' results with the three approaches confirm what was explained in Figure 2.2. From all the frequency ranges, tonal propeller noise is most significant around the first harmonics of the BPF. Outside of this region, especially for higher frequencies, broadband noise is the primary contribution since the higher BPF harmonics do not tend to have high sound pressure levels. For counter-rotating propellers, the narrowband sound pressure spectra will have similar behavior but also the following particularity: aside from the rotor-alone tones for each propeller, there will be a noise component related to their interaction. If the number of blades of each rotor is unmatched, new tonal peaks will arise at linear combinations of both rotors' BPFs. The rotor-alone tones are more visible for lower frequencies. In contrast, the interaction tones

display high sound pressure values for an extended frequency range.

Several challenges inherent to DEP systems are being addressed through current research efforts. These challenges include the influence of inlet distortion on fan efficiency and structural robustness, strategies for noise abatement, and the low specific energy of current battery technologies. Nevertheless, it is still necessary to understand, model, and optimize propeller-airframe aerodynamic and acoustic installation effects, with a strong focus on innovative architectures bringing a tighter integration of the DEP propulsive system into the wing. Contrary to the previous airframe-propeller configurations, another one is selected in the present work, in which the distortion is reinforced as the propeller approaches the scattering surface so that the competition between both aerodynamic and acoustic installation effects is less clear *a priori*. The configuration comprises two propellers over the wing close to its trailing edge.

2.3 Propeller Noise Trend

From section 2.1 and section 2.2, it is clear that unsteady loading noise is one of the prominent noise generation mechanisms of propeller noise worth investigation among the various noise sources for electrical VTOL rotors. Greenwood *et al.* [19] computed some rotor noise predictions for analyzing the aerodynamic performance using blade element methods, and then performed aeroacoustic analyses from the blade geometry and predicted air loads. Semi-empirical broadband noise models were also included, in addition to a variety of signal processing functions and noise metrics [137]. Rotor noise levels were predicted for a hovering operating condition with a fixed thrust in ideal steady conditions, *i.e.*, no inflow distortions or additional airframe components, thus no unsteady-loading noise contribution. The tip Mach number was then varied over a wide range, from 0.3 to 0.8. Finally, the contributions of thickness, steady loading, broadband noise, and total Sound Pressure Level (SPL) are plotted against the tip Mach number.

As can be seen in Figure 2.4, at high tip Mach numbers, thickness noise dominates the total noise levels. However, this source falls off quickly as the tip speed is reduced. Steady loading noise falls off less quickly and significantly contributes to moderate tip speeds. The magnitude of both of these steady noise sources is driven by convective amplification. In contrast, broadband noise is relatively insensitive to tip speed reductions because the noise radiation is mainly induced by unsteady surface pressure fluctuations and not convective amplification [19].

Interestingly, the broadband noise levels increase with decreasing tip speeds beginning at a tip Mach number of around 0.5 because of an increase in turbulent boundary layer noise as the angle of attack of the blade sections increases, eventually leading to flow separation. These results imply that there is likely to be an optimal tip speed for a given rotor geometry, below which additional tip speed reductions will be ineffective in reducing noise or even increasing it. At this optimal tip speed, the sources of unsteady loading will dominate. To date, rotors are designed to operate near the optimal point, at tip Mach numbers at or below 0.5. Lower tip speeds are likely achievable with low steady loading noise when the rotors are lightly loaded, such as during the cruise phase. This suggests that mitigating the unsteady loading noise sources will be the primary concern of electrical VTOL developers seeking to develop low-noise aircraft.

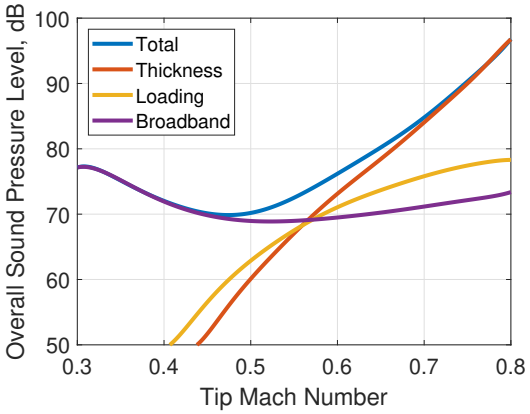

Figure 2.4: Variation in noise by tip Mach number for notional VTOL rotor. No unsteady-loading noise contribution. Adapted from Greenwood *et al.* [19]

Having defined the propeller noise generation mechanisms and previous rotor noise investigations as well as future trends, the chapter 3 of this thesis addresses the description and results of the wind tunnel tests performed as one of the main contributions of the present investigation. The experiments aim to evaluate aerodynamic propeller noise on a DEP architecture setup.

3 Experimental Approach: Wind Tunnel Tests

Summary

The largest part of this thesis consists of wind tunnel tests performed in an anechoic open-jet facility. Thus, this chapter details the methodology adopted to fulfill the objectives of this work. It contains in section 3.1, the description of the models used in the tests, as well as the wind tunnel facility that was used for the experiments in section 3.2. Test conditions are presented in section 3.3. The instrumentation and measurement techniques for each aerodynamic and acoustic analysis are also detailed in section 3.4, including an overview of the theoretical and practical background of the experimental techniques. Finally, the experimental results are presented and discussed in section 3.5.

Contents

3.1 Test Wing and Propeller Models

The wind tunnel experiment is primarily dealing with the scattering of propeller noise by a wing, for an over-the-wing installation and a pair of side-by-side propellers. The configuration is a reduced arrangement mimicking DEP systems possibly used in future flying architectures. The experiment is aimed at demonstrating the feasibility of determining an optimum configuration in terms of sound masking by the wing, with regards to observers located below the wing, preserving acceptable aerodynamic performances. Therefore, both the aerodynamic noise and the performances in terms of combined wing lift and propeller thrust must be considered as parameters for the optimization. The space of parameters will be inspected empirically in the study, except for relying on accompanying analytical modeling to identify either promising or detrimental configurations.

Realistic enough features must be included in the experiment so that the search for an optimum makes sense. For this, the two propellers are synchronized, with adjustable phasing in terms of the relative angular positions of the blades. They can be either co-rotating (COR) or counter-rotating (CTR). The two six-bladed subsonic propellers of 0.2 m diameter placed in pulling configuration are from TUD (Delft University of Technology) and known as the "XPROP-S" [138, 139]. They have a blade stagger angle $\gamma_j = 30°$, as defined at 70% of the tip radius, and are installed at different positions near the trailing edge with adjustable separation. The chord and pitch angle changes along the span of a blade are shown in Figure 3.1. The propellers are powered by two Scorpion SII 4035 250 KV motors up to a speed regime of 7000 rpm, corresponding to a blade-tip Mach number of about 0.24. Two AMT23 encoders with 0.2° accuracy are used for the propeller synchronization and a cooling system keeps the propulsion system within the optimum temperature range. Furthermore, the wing-body is a rectangular airfoil, extruded from the cross-section of a true lifting wing of aircraft in cruise flight configuration, namely the F15 shape, with courtesy of DLR (German Aerospace Center). This vertically mounted scattering unswept "DLR-F15" wing [140] has 0.3 m chord, and 1.4 m total span, for a wetted span of 0.9 m. The wing is set to a non-zero lift angle of attack that will be kept unchanged in the experiment. The primary and relevant parameters of the model are summarized in Table 3.1.

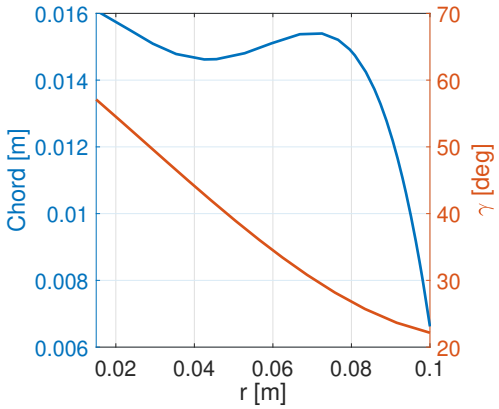

Figure 3.1: Blade chord and pitch distributions of an XPROP-S propeller. Adapted from Reynard *et al.* [139].

Most of the tests were carried out with the original metal blades but some additional tests with 3D-printed ceramic propellers were also performed. The Masked Stereolithography (MSLA) 3D printed technique [141] was employed by using Ultracur3D RG 3280 ceramic-filled resin [142]. Stereolithography (SLA) works by exposing a layer of photosensitive liquid resin to a UV-laser

beam; the resin solidifies in the desired pattern, and the item is created layer by layer until it is finished. The MSLA is still a kind of SLA, but while SLA technology uses a laser to trace layers and is often reserved for industrial applications due to its high cost, MSLA polymerizes an entire layer simultaneously using a matrix of ultraviolet (UV) LEDs and a Liquid Crystal Display (LCD) screen. Initially limited by the low brightness and poor resolution of LCDs, it is now replacing the SLA technology due to the huge improvement in LCDs and up to 20 times faster production speeds for comparable quality results.

Table 3.1: Propellers-wing geometrical and operational parameters.

Parameter	Value
Maximum flow velocity	22 m/s
Wing chord	0.3 m
Total wing span	1.4 m
Propellers diameter	0.2 m
Propellers sweep angle	30°
Number of blades	6
Propellers tip Mach number	0.24
Propellers rotational velocity	7000 rpm
Propellers Reynolds number	5×10^4
BPF	700 Hz

As previously pointed out, the propeller unit is made of an aligned electric motor with an encoder, and additionally, a load cell is placed behind the encoder. The rotating part of the motor is the external black part in Figure 3.2(a), on which an extension is fixed to receive the propeller. The elements are held by mechanical parts fixed to a double hollow beam, in which all cables are gathered. A copper coil inserted in an aluminum part is embedding the encoder. The ends of the coil, seen in the figure, can be connected to long plastic tubes connected to a pump. Continuous circulation of water ensures the cooling of the assembly. The shroud embedding the complete core assembly is 3D-printed. It includes a beam shroud based on a NACA-type design, as well as an axisymmetric center body ending with a profiled back-end (Figure 3.2(b)). The hollow shroud also allows to include an accelerometer and a thermocouple, for vibration and temperature control.

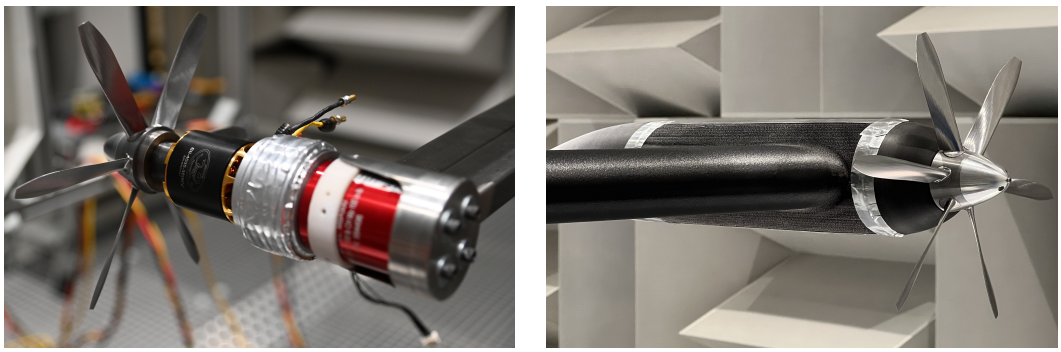

(a) Core assembly of a propulsive unit (b) Installed-in-shroud propeller

Figure 3.2: Propulsion system parts. The encoder is hidden by the coil of the cooling system.

An electronic interface card with an Odrive controller is used to control both motors at the same time by using the schematic diagram shown in Figure 3.3. The whole electronic system is integrated into an external box. The design and implementation of the computer-assisted integrated system have been achieved by the Piwio Company. The electronic power supply is up

to 52 V, therefore, the motors can be powered at their maximum voltage (48 V).

Finally, Figure 3.4 displays the complete setup including not only the previously described propellers-wing architecture but also the facility and instrumentation that will be described in the following sections. It is important to notice that the support of the propellers is separated from the wing to avoid the transmission of vibrations and subsequent additional noise sources.

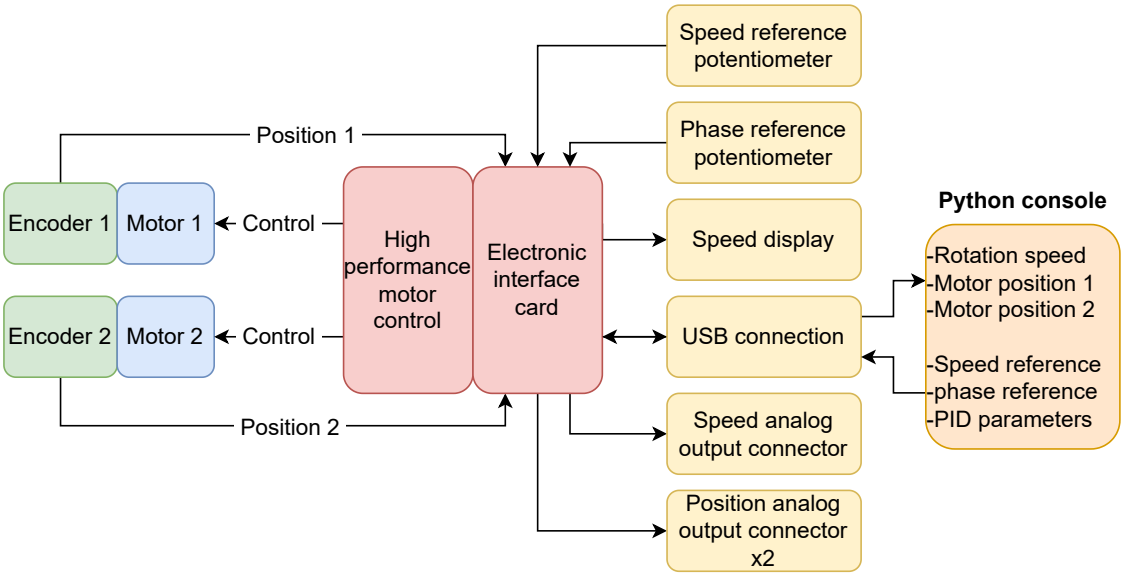

Figure 3.3: Schematic diagram of the power system loop.

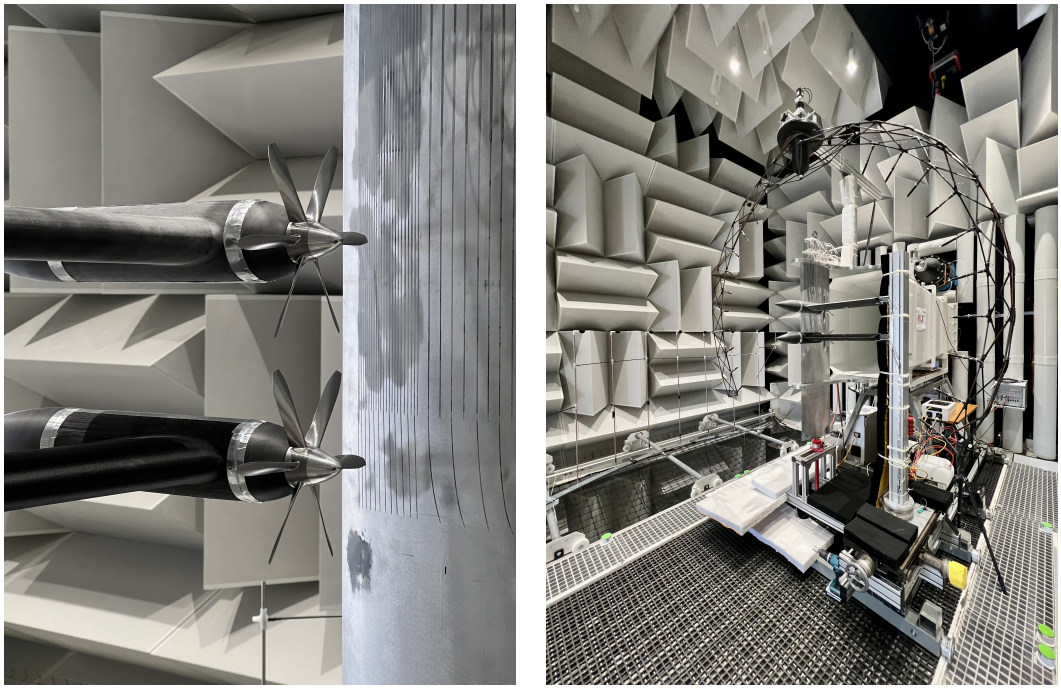

(a) Close-up of the pair of propellers (b) Complete setup view

Figure 3.4: Experimental setup.

3.1.1 Dimensional Considerations

A basic dimensional analysis allows us to identify the most determinant aerodynamic and geometrical parameters to be investigated. The main flow parameters are the mean velocity of the flow delivered by the nozzle, U_0, characterizing the equivalent flight speed of the wing-propeller system, and the rotational speed Ω of the propellers assumed the same for both. U_0 and Ω define the advance ratio $J = \pi U_0/(\Omega r)$, if r is the propeller radius. Once the geometrical description of the propellers is specified, the application of standard Blade-Element Momentum Theory (BEMT) provides values of the induced speed v_i and other details, such as the angle of attack on the blades, for any selected annulus of the propeller disc. The theoretical thrust and torque can also be obtained, for the specified value of J. Because the tonal noise, considered of major interest, is interferential in essence, directions of maximum and minimum noise are expected. The sound field must be explored in a three-dimensional way along two observation angles θ_{obs} and ϕ_{obs}, for instance in a spherical coordinate system with respect to an origin taken close to the sources. More precisely, θ_{obs} corresponds to an angle in the plane of the propeller discs, with origin in the mid-span of the wing. Additionally, ϕ_{obs} stands for an observation angle in a perpendicular plane, with origin on the trailing edge of the wing, for measurements above and below the system. Both angles are shown later on in Figure 3.14. The dual propeller system is defined by the axis-to-axis distance d. Its positioning relative to the wing is defined from the wing trailing edge point at mid-wetted span, by the streamwise distance to the edge D and the normal-to-wing distance h. Because the blades are unswept and radially aligned, the mid-chord plane of the propellers and the plane containing the propeller axes are taken as references for the definition of these distances. The blade chord length c is another involved parameter, whereas the full span can be assimilated to the tip radius for dimensional considerations, in view of the large aspect ratio. The selected propeller-wing configuration representative of DEP architectures for aircraft is depicted in Figure 3.5.

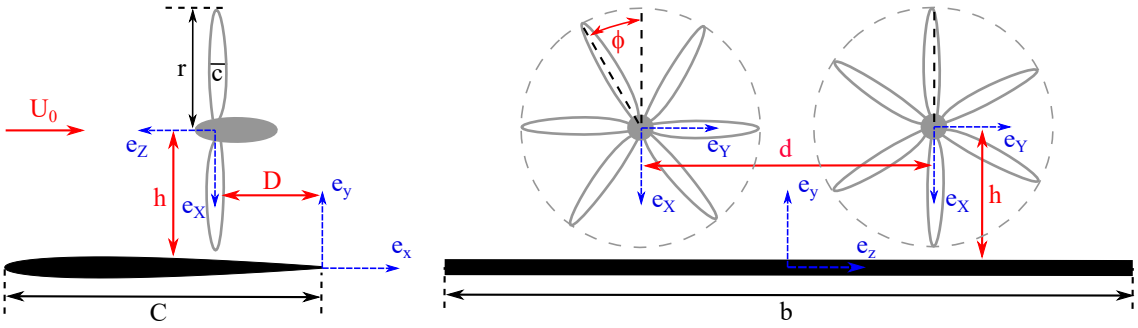

(a) Side view (b) Front view

Figure 3.5: Propellers-wing configuration, reference frames, and main notations.

At any observation point, the Root-Mean-Square (RMS) sound pressure can be *a priori* expressed in a dimensionless form as a function of a series of parameters:

$$\frac{p_{rms}}{\rho c_0^2/2} = \mathcal{F}\left(\mathcal{R}e, M_t, J, k_B, \theta_{obs}, \phi_{obs}, k_B r, k_B h, k_B D, k_B d, \phi, m\right) ,$$

where r is the propeller radius, ρ_0 is the mean fluid density, c_0 the sound speed and $M_t = \Omega r/c_0$ the blade-tip Mach number. $\mathcal{R}e = U_{rel}c/\nu$ is the Reynolds number built on the blade chord c and the relative speed U_{rel} (a function of Ω and U_0), at some reference radial position, usually chosen as a percentage of r. It is representative of the flow regime around the blades, and is usually low for the present application, entering the transitional range. M_t and J determine the

axial-flow Mach number $M_0 = U_0/c_0$. $k_B = B\Omega/c_0$ is the acoustic wavenumber at the BPF, B the number of blades, ϕ the propellers offset angle, and m the BPF harmonic order.

The functional form $\mathcal{F}$ is *a priori* unknown, the experiment is a way to partially determine it. The number of its dimensionless arguments can be defined rigorously by the Vaschy-Buckingham theorem, provided that a reasonably reduced exploration space of variables is previously identified. But the definition of the parameters is arbitrary; they could be replaced by some combinations of them, at a constant total number of parameters (for instance, M_0 could be selected in place of M_t). The dependence on $k_B R$ can be suppressed for an observer in the acoustic far-field, by virtue of the decrease with inverse distance $1/R$ ensuring similarity. Furthermore, the Reynolds and Mach numbers, as well as the advance ratio, are varied in a limited range. The maximum tangential Mach number is about 0.2 at 7000 *rpm*. The instrumentation is designed in such a way that acoustic measurements are performed globally on a portion of the sphere, for fixed values of the flow and propeller positioning parameters. All values of m are accessed, as well as, implicitly, the broadband noise.

The present experimental setup allows to explore effects of Ω, J, ϕ, h, D and d, for the 6-bladed propellers, on the acoustic signature. A similar analysis can be roughly outlined for the aerodynamic performances. This means that the combined lift of the wing and thrust of the propellers, on the one side, and wing drag and propeller torque, on the other side, must be considered together as they are functions of the same set of parameters. In view of its size, the addressed 6-dimensional space must be bounded. Limits are imposed by the installation itself, and by an *a priori* estimation of what is acceptable in terms of aircraft design.

One of the key points to be addressed about sound scattering by the trailing edge is the possible amplification of dipole radiation for compact distances of the sources to the edge. According to Roger *et al.* [143], amplification is expected as the Helmholtz number kr_0 is below 0.1, r_0 being the distance of a point dipole to the edge. This could occur in the present case at the BPF for a blade-tip force if $k_B\sqrt{D^2+(h-r)^2} < 0.1$, thus for a tip-to-edge distance of about 1 *cm* at 7000 *rpm*. Such a positioning is not likely to be encountered in practical applications; indeed it corresponds to a distance to the edge of 3.3% of the wing chord and 5% of the propeller diameter. Yet the question of the effect of short distances approaching the amplification regime is still open. Moreover, substantially lower frequencies would be produced by propellers of the same size but with lower blade numbers, making the issue more critical. For these reasons, a short distance of the order of the centimeter must be tested in the experiment.

Two regimes of interaction can be addressed with the present experimental setup (see Figure 3.6), namely the true over-the-wing configuration, and an asymmetric behind-the-wing configuration. In the first case, $(h > r, D > 0)$, significant masking by the wing is expected for observers located below the wing. In the second case, $(D < 0)$, additional sound generation is expected from the operation of part of the blade span through the wing wake when $h < r$ [84].

Even though almost 100 configurations were experimentally assessed and analyzed, as described in Table 3.2, only the most critical cases *i.e.*, configurations with maximum (Max) and minimum (Min) D, h, and d parameters are discussed for both offset phase angles ϕ, flow velocities U_0, and directions of rotation, as shown in Figure 3.7.

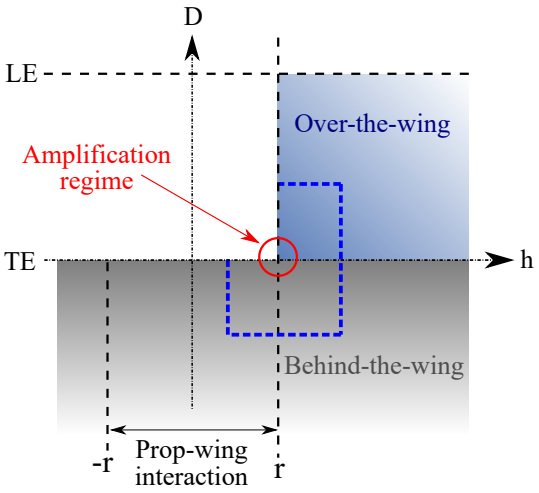

Figure 3.6: Domain of parameters h and D for the assessment of wing scattering. Indicative bounds of the searching domain are indicated with the blue dotted line.

Table 3.2: Parametric variations of the wing-propellers configurations.

	1	**2**	**3**
D	$0.1r$ $(0.01\ m)$	$0.5r$ $(0.05\ m)$	r $(0.1\ m)$
h	$r + 0.1r$ $(0.11\ m)$	$r + 0.5r$ $(0.15\ m)$	-
d	$2r + 0.1r$ $(0.21\ m)$	$2r + 0.5r$ $(0.25\ m)$	-
ϕ	$0°$	$30°$	-
$\mathbf{U_0}$	$0\ m/s$	$22\ m/s$	-
Rotation	COR	CTR	-

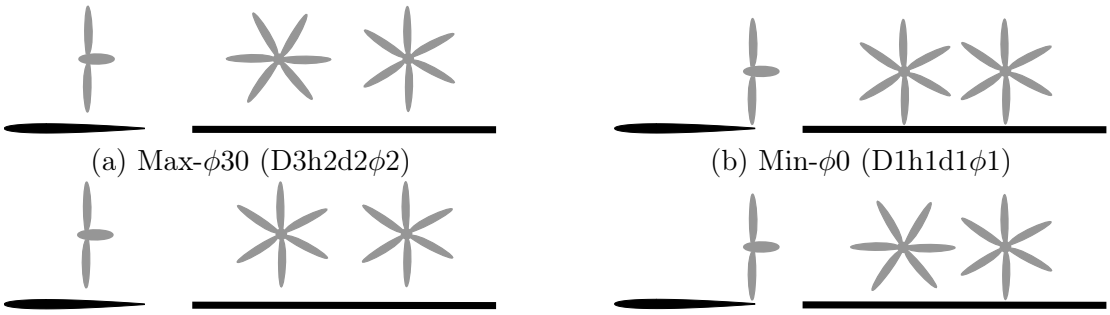

(a) Max-ϕ30 (D3h2d2ϕ2)

(b) Min-ϕ0 (D1h1d1ϕ1)

(c) Max-ϕ0 (D3h2d2ϕ1)

(d) Min-ϕ30 (D1h1d1ϕ2)

Figure 3.7: Critical tested configurations.

3.2 Wind Tunnel Facility

Experiments are performed in the high-speed open-jet anechoic wind tunnel in the Fluid Mechanics and Acoustics Laboratory (LMFA) of *École Centrale de Lyon* (ECL) [144, 145]. The wind tunnel has an open test section of 0.9 m height and 0.7 m width with chamfered corners. The nozzle emerges inside an anechoic chamber, as shown in Figure 3.8, with average length, height, and width of 10 m, 9 m, and 8 m, respectively. The chamber has slightly diverging walls made of glass wool wedges coated by perforated metallic panels for acoustic absorption. An 800 kW electric motor drives the fan, which delivers the flow from an external environmental inlet to the

outlet in the anechoic chamber. An acoustically treated duct absorbs fan noise with honeycomb and liners embedded in the streamwise direction and upstream of the outlet nozzle. Additionally, several grid screens are located close to the final contraction, generating residual turbulent intensity of the flow in the room lower than 0.5%. The maximum design free-flow speed is continuously adjustable depending on the cross-section, starting from 60 m/s for the original rectangular one of 0.56 m height and 0.56 m width. However, the maximum achievable flow speed in the present study will be 30 m/s, due to the enlarged open test section.

Figure 3.8: View of the wind tunnel and the anechoic chamber.

3.3 Tests Conditions

3.3.1 Numerical Simulations

Although the primary approach of this investigation is not numerical, some Reynolds-Averaged-Navier-Stokes (RANS) simulations were performed to validate the new wind tunnel diverging duct (diffuser) design and verify the best wing angle of attack for the experimental tests. The numerical simulations were evaluated using the commercial software ANSYS-FLUENT 2021, a widely accepted computational tool that works with the finite volume method. Incompressible flow and steady-state were assumed. Two different cases were simulated. The first one was aimed at defining a relevant diffuser geometry. The second one involved the diffuser and the wing model placed farther downstream outside of the wind tunnel. In addition, the computational domain dimensions and boundary conditions were adjusted to the characteristics and location of the wind tunnel used for the experiments.

In the design of a wind-tunnel diffuser with hydraulic diameters D_{h1} and D_{h2} at the entrance and exit, respectively, and total length L_d, the primary parameter to be set is the equivalent conical expansion angle θ_e [146]. For rectangular cross-sections, this angle is recommended to be lower than 5° [147]. The hydraulic diameter for a rectangular cross-section area A and the equivalent diffuser length L_d are calculated as follows:

$$D_h = 2\sqrt{A/\pi} \quad \text{and} \quad L_d = \frac{(D_{h2}/2) - (D_{h1}/2)}{\tan\theta_e}$$

The selected conical expansion angle of 4° results in rectangular duct expansions of 1.6 m length with angles of 5° and 3° in the vertical and horizontal directions, respectively. The diffuser cross-section corner cuts are aimed at avoiding detrimental flow separation. However, expansions do not deliver a uniform velocity distribution in the test section. Therefore, a constant-area section of 0.4 m length is added after the final expansion area, for a 2 m total length. As shown in Figure 3.9, the new diffuser allows an expansion from a frontal area of 0.56 $m \times 0.56$ m to 0.90 $m \times 0.70$ m height and width, respectively.

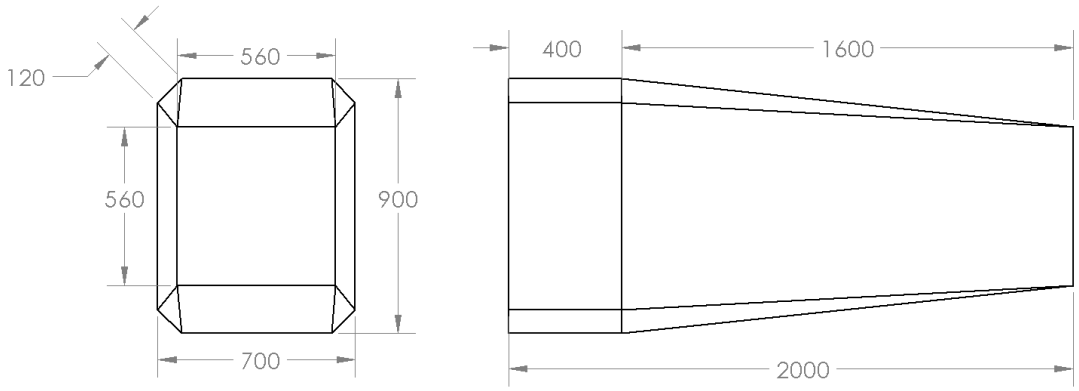

Figure 3.9: Diffuser main dimensions in mm.

For simulating the diffuser performance, the computational domain in Figure 3.10(a) was selected. Once the diffuser was validated, the second case (diffuser + wing) was simulated as well by using a new domain shown in Figure 3.10(b). A wide range of angles of attack was examined, from $\alpha = 0°$ to $= 12°$, selecting $\alpha = 10°$ for having a realistic lift coefficient value of an urban air vehicle.

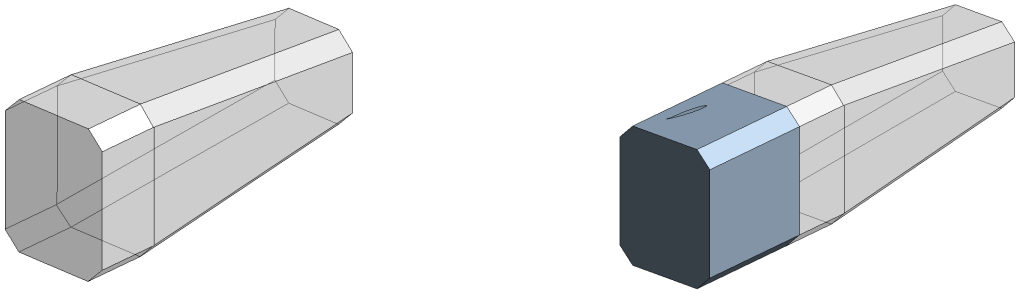

(a) Case 1 (b) Case 2

Figure 3.10: Computational domains. Wing cross-section shown on the upper side of the colored extension in subplot (b).

Two appropriate meshes were created by discretizing the computational domain in an adequate number of elements. A grid independence study was carried out to ensure that the grid refinement does not affect the solution. This study gave the size of the grid elements with the lowest computational cost by maintaining a fine near-wall mesh. For the first case, a structured mesh with 10 M elements was implemented, whereas, for the second, an unstructured mesh with tetrahedral elements was created for the whole domain; however, a structured coarser mesh was used near the walls, and the wing to capture the boundary layer effects, which resulted in a 22 M elements mesh. In both cases, the meshes had a 2×10^{-3} m maximum element size, whereas the first element thickness away from the walls was $Y_t = 1 \times 10^{-5}$ m, resulting in a maximum viscous sub-layer of $Y^+ = 1$. A wall inflation condition of 26 cells and 1.1 growth rate was imposed in

both the diffuser and wing model walls. Figure 3.11 displays general and closer views of the mesh implemented in the diffuser.

A velocity inlet condition of 45 m/s and a gauge pressure outlet condition of 0 Pa were defined for boundary conditions. In addition, for the diffuser walls, a no-slip shear condition was implemented, where the roughness height is 0 m, and the roughness constant is 0 which indicates a uniform wall roughness. Additionally, the inlet and outlet have a turbulent intensity of 0.5%, as expected in the experiments.

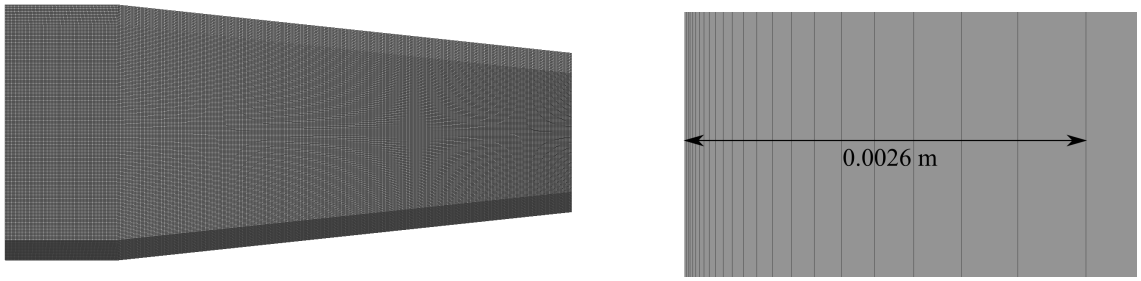

(a) Structured mesh (b) Wall inflation dimensions

Figure 3.11: Diffuser mesh.

In this problem, the fluid flow is assumed to be steady, incompressible, and fully turbulent. For this case, the Navier-Stokes (NS) equation is solved where the unknowns are the velocity and the pressure. The continuity equation forces the incompressible condition. Since the NS equation alone cannot predict fluid flows at high Reynolds numbers, it was necessary to include a turbulence model in the equations system. The Shear Stress Transport (SST) turbulence model, which accurately models typical high-lift aerodynamic problems, was used to maintain simplicity alongside the turbulence model transport equations of turbulent kinetic energy κ_t and turbulent dissipation ω_t. The SST κ_t-ω_t have shown better results than other turbulence models for all flows in aerodynamic applications involving boundary layers under adverse pressure gradients, recirculation, and flow separation, ensuring that the transition effects at high turbulence levels are correctly modeled by calibrating the coefficients for the appropriate flow phenomena [148, 149]. As the fluid flow is incompressible, a pressure-based solver was used with the SIMPLE segregated algorithm [150], where the pressure is corrected by enforcing mass continuity over each cell. For the spatial discretization, the convective terms were set by a second-order upwind and the pressure with a second-order central-difference scheme. Finally, the turbulent variables were solved with a first-order upwind scheme.

Some numerical results are shown below. The total velocity contour in Figure 3.12 shows that there is no flow separation around the airfoil at the selected angle of attack. Figure 3.13 displays the velocity along the diffuser center line and axial-velocity profiles at several length stations. These results verify the correct design of the diffuser as the minimum needed velocity at its exit was achieved. Additionally, the velocity profile at the end of the diffuser confirms that a sufficient area of nearly-uniform flow is formed, so that the complete setup including wing and propellers will be free of interaction with the lateral velocity gradient of the shear layers.

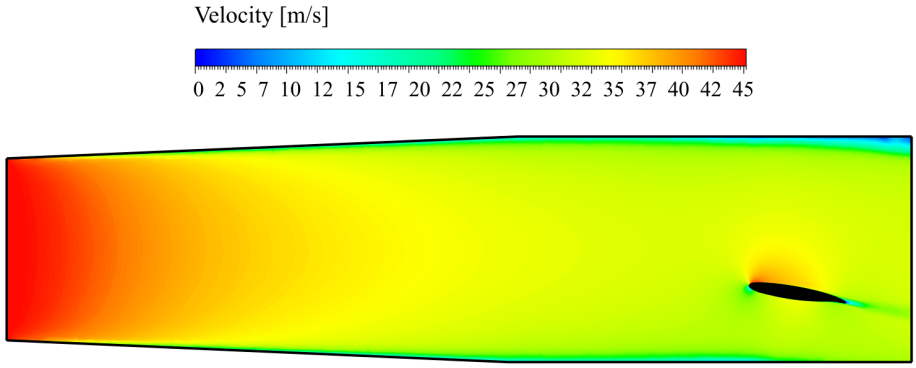

Figure 3.12: Diffuser velocity contour with wing model at $\alpha = 10°$.

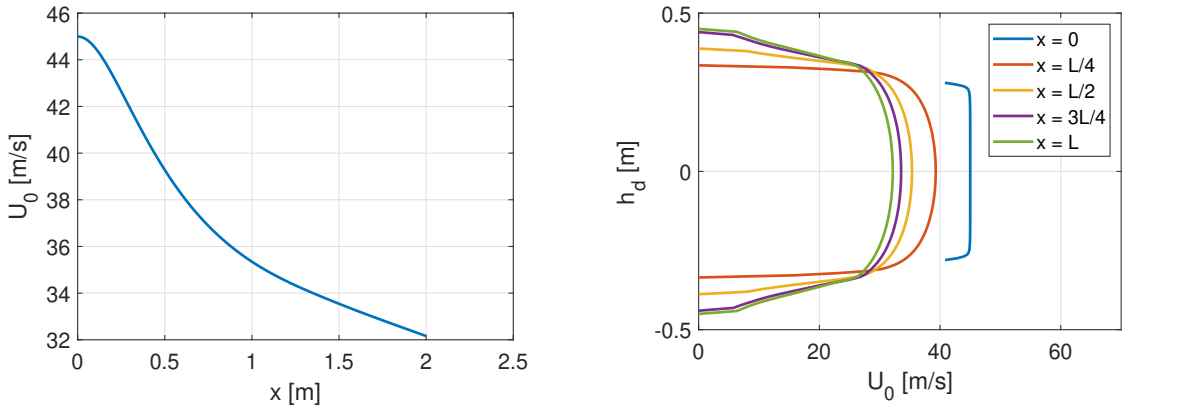

(a) Velocity along diffuser center line (b) Velocity profiles along the diffuser's length

Figure 3.13: Diffuser axial-velocity variation. h_d stands for the diffuser height.

3.3.2 Selected Reference Configuration

The maximum selected wind tunnel speed for the experimental campaigns was 22 m/s, corresponding to 4.5×10^5 Reynolds number based on the chord length of the model wing. Tests were performed for different model configurations, varying the position of the propellers and RPM settings but maintaining their orientation. The propeller axis was always aligned with the direction of the upstream flow, along the nozzle axis. Before these tests, a reference configuration has been defined, as a clean configuration with no propellers. For this, the wing was tested for a single deflection angle $\alpha = 10°$.

3.4 Instrumentation and Measuring Techniques

3.4.1 Acoustic Far-field

Acoustic measurements were taken with an array of 20 Bruel & Kjaer type 4958 1/4" free-field microphones distributed around the model on a 2 m diameter rotating arc antenna, at angles θ_{obs} every 10° as shown in Figure 3.14(a), the microphones 4 and 17 being at ±90°. The antenna reached 11 positions (ϕ_{obs} from 45° to 135° on the left-bank side facing the suction side of

the wing, plus diametrically opposite positions) by rotating around the vertical axis to cover a portion of a sphere and obtain three-dimensional sound directivity. For practical reasons, the arc antenna of far-field microphones can be rotated around its axis by a maximum amount of ±45° concerning a reference position perpendicular to the direction of the wind-tunnel stream. Larger angular displacements would make the measurements suffer from sound scattering by the lips of the nozzle and/or from contamination by the pseudo-sound pressure of the jet shear layers.

The pre-polarized microphones can measure sound pressure levels up to 140 dB for a maximum frequency of 20 kHz. The Transducer Electronic Data Sheet (TEDS) contains information about the complex transfer function, hence enabling applications to calculate corrections for the individual transducer, resulting in more precise measurements [151]. The raw signals are converted through the microphone calibration performed with a Bruel & Kjaer type 4231 sound calibrator [152] and a software code after the acquisition. The microphone preamplifier is of the industry standard Constant Current Line Drive (CCLD) type for use with a cheap coaxial cable for signal, a power supply, and TEDS. A rugged protection grid provides an integrated heat shield. The microphone is front-vented for pressure equalization. The main specifications of the microphones and sound calibrator are detailed in Table 3.3 and Table 3.4, respectively.

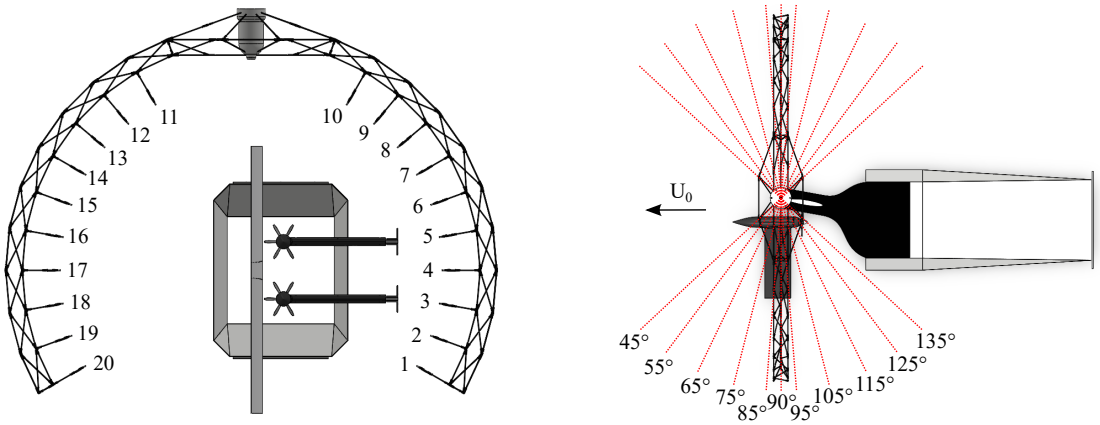

(a) Microphone numbering (frontal view) (b) Antenna positions (top view)

Figure 3.14: Antenna location regarding the setup and wind tunnel. The antenna axis coincides with the wing trailing edge.

Table 3.3: Bruel & kjaer type 4958 microphone specifications.

Parameter	Value
Dynamic range	28 – 140 dB
Frequency range	10 – 20000 Hz
Sensitivity	11.2 mV/Pa
Temperature range	-10 to 55 $°C$

Table 3.4: Bruel & kjaer type 4231 sound calibrator specifications.

Parameter	Value
Calibration pressure	94 – 114 dB
Calibration frequencies	1000 Hz
Calibration accuracy	±0.2 dB

The microphone data acquisition is performed through 4 synchronized AC/DC (Alternating Current/Direct Current) coupling NI (National Instruments) PXI-4472 boards of 8 analog

inputs each and mounted in a NI PXI-1042Q chassis [153, 154]. The boards are dynamic signal acquisition modules for acoustic and vibration measurements. The input channels incorporate Integrated Electronic Piezoelectric (IEPE) signal conditioning for accelerometers and microphones and anti-aliasing filters that automatically adjust to the sampling rate. All eight input channels of the PXI-4472 simultaneously digitize input signals. The acquisition is controlled by a NI PXI-8331 interface module that gives PCs direct control of the PXIs-4472. A LabView environment developed at the laboratory was also employed for the data acquisition at a 51.2 kHz sampling frequency. The data were acquired simultaneously with the acquisition parameters described in Table 3.5.

Table 3.5: Sound acquisition parameters.

Parameter	Value
Acquisition time	30 s
Sample rate	51.2 kS/s
Cutoff frequency filter	3.4 Hz
AC precision	24 $bits$

3.4.2 Free Stream Conditions

Flow velocity measurements were performed by a KIMO L-shaped pitot tube. The curved neck design of the L-shaped probe enables less downstream airflow blockage since the shaft is perpendicular to the tip of the probe without interaction with the air stream. The stainless steel body and ellipsoidal head pitot tube has one main intake hole for measuring the total pressure and 6 additional holes for static pressure [155]. The transducer was mounted in an automatic traverse system that mapped the flow velocity at the exit of the diffuser. The main specifications of the pitot tube are detailed in Table 3.6.

Table 3.6: KIMO L-shape pitot tube specifications.

Parameter	Value
Maximum static pressure	2 bar
Acceptance angles	$\pm 10°$
Accuracy	1%
Air velocity range	0 to 100 m/s
Temperature range	0 to 600 $°C$

Data were acquired by a digital multi-function Furness Controls FCO560 pressure transducer combined with LabVIEW. The FCO560 is a low-differential pressure instrument with two modes of operation. The calibration mode fulfills the calibration requirements for low differential pressure flow devices. The measurement mode provides a versatile precision micro-manometer that is combined with pitot tubes for measurement of velocity, volumetric flow, and mass flow [156]. The high-accuracy probe calibrations define the relationship between the probe pressures measured and the actual velocity sensed by the probe and the pressure transducers. A pneumatic tubing was connected from the ports of the multi-hole probe to the pressure measurement system for correct data acquisition with the parameters described in Table 3.7.

Table 3.7: Flow velocity acquisition parameters.

Parameter	Value
Acquisition time	20 s
Sample rate	275 $S/s/Channel$
Cutoff frequency filter	3.4 Hz
Resolution	24 $bits$

3.4.3 Flow-Field Characteristics

During the first campaign, the mean velocity and turbulent intensity were measured in the wake of the wing with a single hot-wire Dantec Dynamics 55P01 probe. This probe consists of a 5 μm diameter and 0.00125 m long platinum-plated tungsten active sensor, the ends of which are copper- and gold-plated to a thickness of 15 to 20 μm diameter. The end-to-end length is 0.003 m and it is attached to a pair of 0.008 m long prongs that are hold by a 0.0019 m diameter, 0.03 m long ceramic cylinder [157]. The main physical specifications of the hot-wire sensor are detailed in Table 3.8.

Table 3.8: Dantec 55P01 sensor specifications.

Parameter	Value
Temperature coefficient of resistance	0.36% $°C$
Max. sensor temperature	300 $°C$
Max. ambient temperature	150 $°C$
Velocity range	0.05 to 500 m/s

The hot-wire is of the Constant Temperature Anemometer (CTA) type. The CTA technique is based on feeding current through the wire, which raises its temperature and subsequently modifies its resistance. The CTA approach consists of adapting the voltage to keep the wire temperature constant regardless of the flow velocity. For a given flow velocity, the heat exchange due to convection can be measured as a voltage across the bridge, and related to this velocity through calibration charts. The data acquisition for the flow-field measurements was performed using a SteamLine Pro Dantec Dynamics analog anemometer system equipped with CTA modules [158]. The system is operated by the StreamWare Pro software, which performs hardware set-up, automatic probe calibration, data acquisition, conversion, and reduction, allowing velocity measurements with high spatial and temporal resolution, high dynamic range, and excellent accuracy. The data acquisition was performed with a 1 kHz sampling rate, and 1024 samples were taken for each measurement. An automatic 2-axis traverse system controls the probe during the measurements. Thus, the measurement acquisition points are defined through a grid before the experiment starts. The first hot-wire wake measurements were conducted for one spanwise station by steps of 0.5 mm close to the trailing edge up to 5 mm further in the horizontal direction for a total of 115 points. Wing-wake measurements are not directly used in the present work; they are performed for future use, such as comparison with possible numerical simulations. The acquisition parameters are described in Table 3.9.

Table 3.9: Hot-wire acquisition parameters.

Parameter	Value
Acquisition time	20 s
Sampling rate	1 kHz
Samples	1024
Resolution	24 bits

3.4.4 Surface Pressure

The wing model instrumentation includes two chordwise sets of 32 steady-state pressure taps distributed on both pressure and suction sides, with refined distributions close to the leading edge and in the aft part on the suction side, where the propellers are positioned. In the reference state, the two rows of pressure taps are located in the center part of the vertical flow extent, at 0.05 m on each side from the mid-wetted-span. Arbitrary spanwise measuring positions can be reached by shifting the wing vertically with respect to the other parts of the setup. Indeed, distributed pressure-coefficient measurements are needed to characterize the aerodynamic performances of the wing in the presence of the propellers, with some expected spanwise non-uniformity. Figure 3.15(a) shows the positions of the pressure taps in the two instrumented cross-sections.

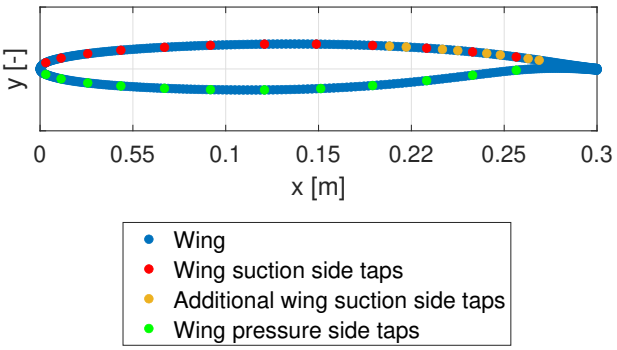

(a) Pressure taps distribution

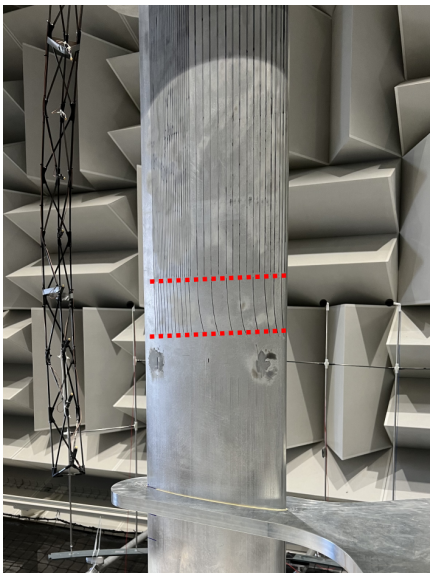

(b) Pressure taps rows

Figure 3.15: Pressure taps locations.

Figure 3.15(b) shows the instrumented part of the wing, with two lines of pressure taps, made of pinholes ending tubes that are spanwise-inserted in the body of the wing, and connected to an external multi-channel manometric system. The two lines are slightly oblique with respect to the chord direction to avoid wake effects between adjacent pinholes. Making the wing slide through its supports allows to scan the wall pressure and reconstruct a complete pressure-coefficient map.

The pressure taps are connected to pressure tubes guided out of the wing and connected to a KMPS-1-64 Kulite pressure scanner of 0.1% accuracy, which works in a 1 - 2 *psi* range. The KMPS-1-64 is a highly compact electronic pressure scanner module designed for wind tunnels. It accepts up to 64 pneumatic inputs and converts them into high-accuracy outputs for both analog and digital systems. The sensors are arranged into 4 groups of 16 and the 64 pressure inputs

can be measured at the same time with a trigger input for low latency triggered acquisition. The module also incorporates a calibration valve that enables sensors to be automatically calibrated online and purges the input lines of contaminants or condensation. Additionally, it is vibration and moisture-resistant, leading to extreme reliability. Due to the wide temperature capability, it does not require heating or cooling in the wind tunnel [159]. The main specifications of the scanner sensor are detailed in Table 3.10.

Table 3.10: KMPS-1-64 Kulite pressure scanner specifications.

Parameter	Value
Pressure range	$1 - 2\ psi$
Electrical excitation	8 to 32 VDC
Accuracy	$\pm 0.1\%$
Temperature range	-15 to $125\ ^{\circ}C$

Data are acquired simultaneously for all pressure inputs via ethernet digital output allowing integration into standard networks for connecting the Kulite pressure scanner with a local computer. The acquisition parameters are described in Table 3.11.

Table 3.11: Pressure acquisition parameters.

Parameter	Value
Acquisition time	$20\ s$
Sample rate	$275\ S/s/channel$
Resolution	$24\ bits$

3.4.5 Aerodynamic Forces

The propeller torque moments as well as tension and compression loads, were measured with a Futek MBA500 (100/100) bi-axial load cell. This torque/thrust sensor is temperature-compensated and able to achieve 0.2% nonlinearity and yet provide 125-150% over-capacity. Additionally, high precision is achieved through two separate outputs for applied torque and thrust forces. Furthermore, the voltage measurements from the strain gauge of the load cell are amplified through the Futek IAA100 amplifier, which allows for gains and filtering regulations [160, 161]. The main specifications of the load cells are detailed in Table 3.12.

Table 3.12: Futek MBA500 (100/100) bi-axial load cell specifications.

Parameter	Value
Load capacity	$\pm 444\ N$
Torque capacity	$\pm 11.3\ Nm$
Sensitivity	$2\ mV/V$
Temperature range	-42 to $93^{\circ}C$

The data were acquired simultaneously with the acquisition parameters described in Table 3.13. Since the signal provided by the amplifier has an electric nature, it was converted to force units through calibration constants calculated from Figure 3.16 and embedded in the acquisition software, so the output was already in force units.

After calibrating the load cells, the trace points shown in Figure 3.17 were measured by varying the propellers' velocity, from zero to the nominal speed of 7000 rpm. Indices 1 and 2

refer to the two propellers. Then the conversion of the obtained values in Volts was made using the constants in Figure 3.16 and the corresponding load and torque for both load cells can be seen in Figure 3.18. The discrepancies between both propellers are negligible, especially for thrust and at extreme rotational speeds, which are investigated in the experiment.

Table 3.13: Forces acquisition parameters.

Parameter	Value
Acquisition time	30 s
Sample rate	51.2 kS/s
Cutoff frequency filter	3.4 Hz
DC precision	24 bits

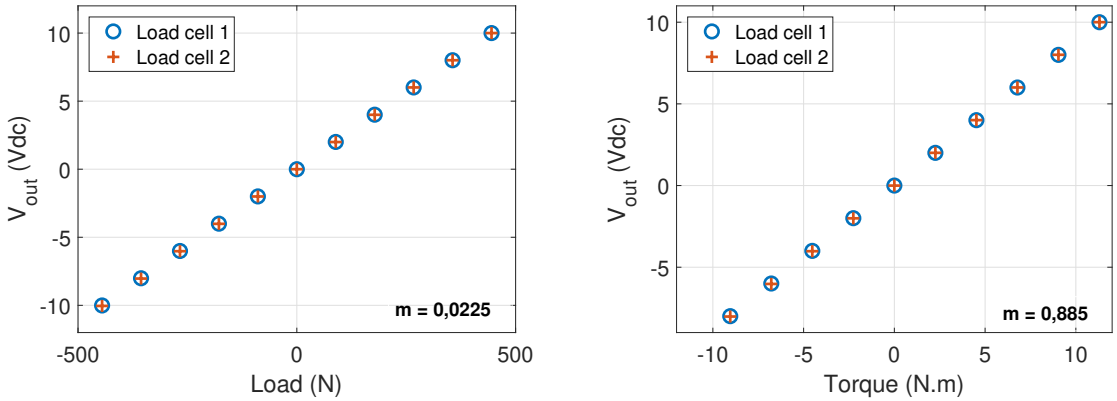

(a) Load (b) Torque

Figure 3.16: Load cell calibration lines.

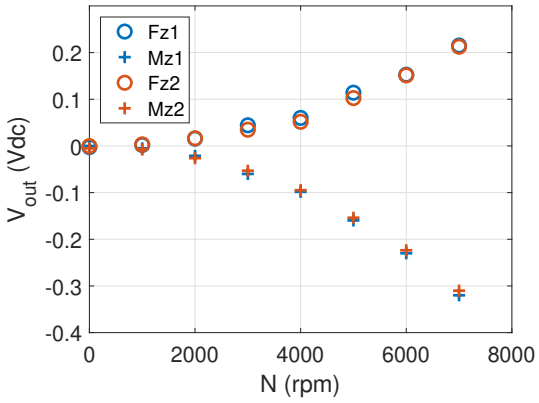

Figure 3.17: Trace points.

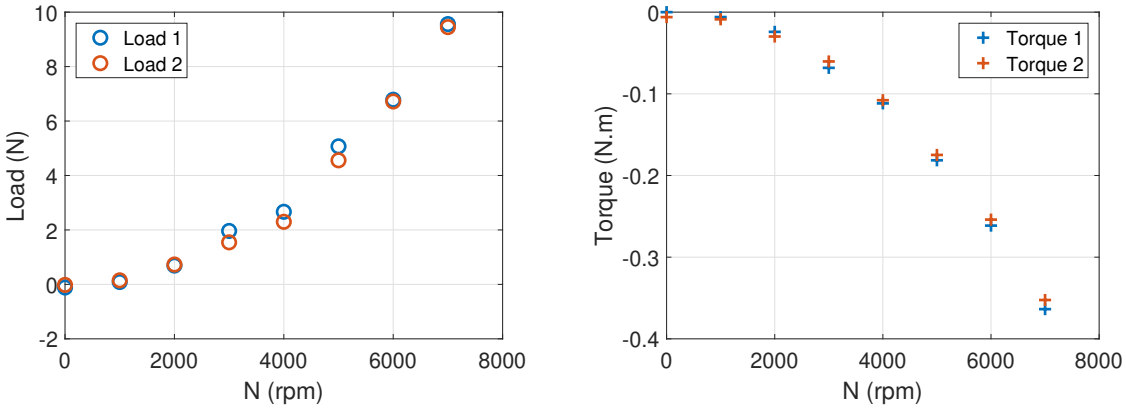

(a) Load (b) Torque

Figure 3.18: Load cell calibration lines

3.5 Results and Discussions

3.5.1 Aerodynamic Performances

The experimental analyses started with the verification of the flow parameters upstream and downstream of the propellers-wing model to corroborate the numerical results previously explained in section 3.3. Figure 3.19 shows the measured upstream mean velocity profile with an expected constant and low turbulence velocity in the center of the diffuser where the propellers will be placed. Additionally, the profile displays a velocity deficit close to the continuation of the diffuser walls produced by the shear layer as in Figure 3.12. A complete measured velocity map at the exit of the diffuser is shown in Figure 3.20(a). The map evidences a velocity re-distribution due to the presence of the wing (around $y = 400\ mm$), suggested by the asymmetry. Local drops are noticed near the middle of each edge. In contrast, The numerically predicted map plotted in Figure 3.20(b) is found nearly symmetrical. Additionally, it features areas of lower velocity close to the corners of the diffuser, much larger than in the measurements. The finally observed area of nearly homogeneous flow, especially in the spanwise direction, larger than expected, is an advantage for the installation of the propellers.

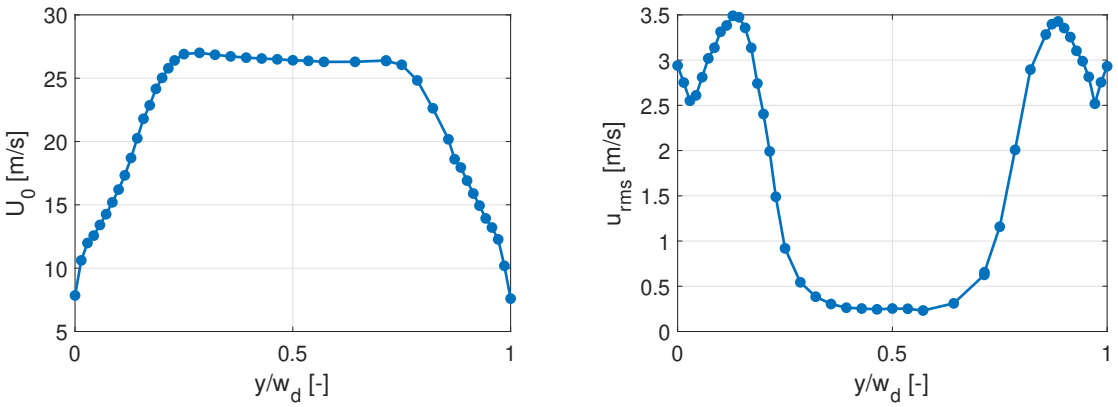

(a) Mean velocity (b) Turbulent velocity

Figure 3.19: Upstream velocity profiles at mid-span.

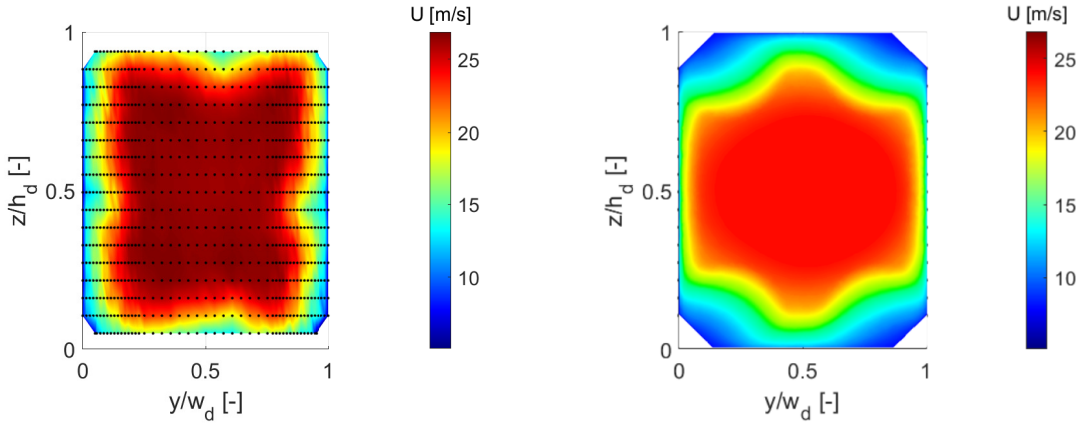

(a) Experimental (b) Numerical

Figure 3.20: Axial-velocity colormap at diffuser exit, with wing model installed at $\alpha = 10°$. The measured points with traversing Pitot tube are featured by the black dots.

The results of downstream near-wake HWA (Hot Wire Anemometry) measurements are shown in Figure 3.21. The closer the wake measurements are performed to the trailing edge, the deeper the velocity deficit is. Few differences are found between scans at 2 mm and 5 mm. In contrast, the wake is thicker and weaker as the probe is moved farther downstream at 50 mm and 100 mm. It is worth mentioning that the lower velocity peak is shifted to the right because of the angle of attack of the wing, and the scanning perpendicular to the nozzle axis. The results confirm that the flow remains attached to the wing. Furthermore, the asymmetry between values on the pressure and suction sides of the wing is associated with the non-zero lift.

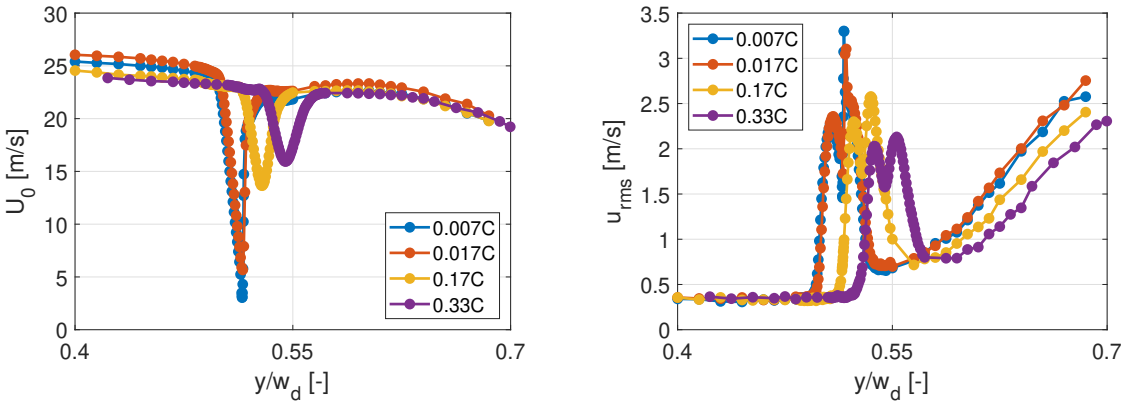

(a) Mean velocity (b) Turbulent velocity

Figure 3.21: Downstream axial-velocity profiles at mid-span. Traverses normal to the nozzle axis.

Figure 3.22 presents a summary of the lift-coefficient C_L results computed by integration of the pressure coefficient C_P of each tested COR configuration. What stands out in this figure, is the higher influence of the h parameter (the distance from the tip of the blades to the wing) on C_L. Among all configurations, this is a key parameter. The lift also increases when the rotation of the propellers is synchronized with zero angular offset ($\phi = 0$), while the distance between them (d parameter) has a slight effect. In fact, for all the configurations, the C_L is less than 3% lower for the cases of $d2$. Finally, the D parameter (chordwise distance between the propellers and the trailing edge) also has an important role. The closer the blades approach the trailing edge, the higher the lift increases, with a steeper slope for the $h1$ configurations. The wing C_L

measured with no propellers is also plotted for comparison purposes. As can be seen in both $d1$ and $d2$ cases, the propellers increase the lift coefficient, even for their farther position from the trailing edge of the wing.

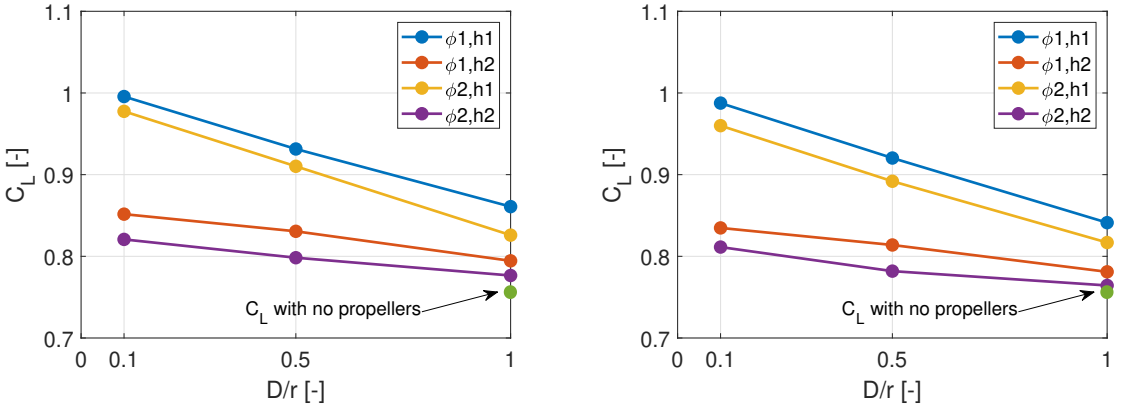

(a) d1 (b) d2

Figure 3.22: Effect of several parameters on the C_L for COR propellers.

As explained before, pressure measurements have been made with the two instrumented pressure taps rows, at the flow speed of 22 m/s selected for the study, leading to the following pressure-coefficient plots. First, Figure 3.23 shows the reference C_P case without any propeller over the wing. This case shows a clear homogeneity in the spanwise direction in both the pressure and suction sides and the maximum C_P peak. In particular, no significant variation due to the shear-layers of the wind-tunnel jet is seen in the explored area.

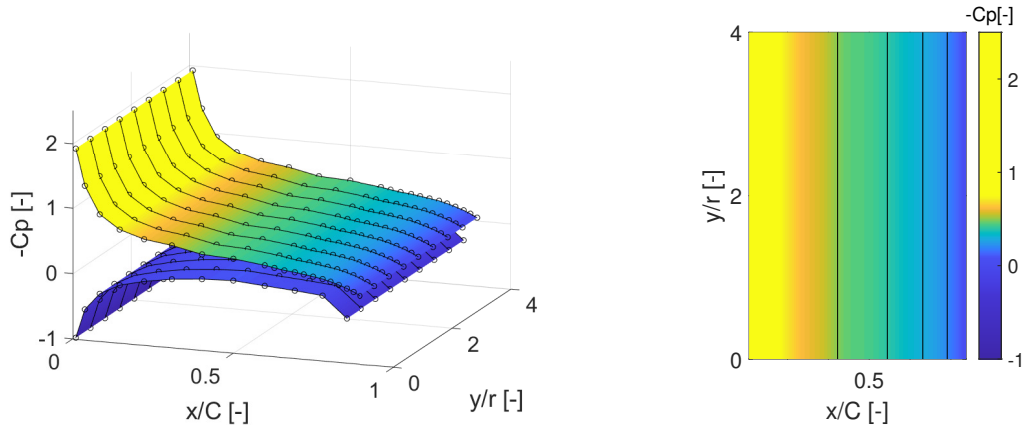

(a) 3D C_P (b) Suction side C_P

Figure 3.23: 3D and suction side C_P without propellers.

From now on, the lower (Max-ϕ30) and higher (Min-ϕ0) C_P cases for COR propellers are compared (see Table 3.2). As can be seen in Figure 3.24(a) and Figure 3.25(a), conditions close to homogeneity in the spanwise direction are achieved with the Max-ϕ30 configuration, in both the pressure and suction sides, except for a moderate bump in the area between propellers, extending up to the leading edge. In contrast, Figure 3.24(b) and Figure 3.25(b) exhibit a more pronounced spanwise heterogeneity along the measured wing suction side with the Min-ϕ0 configuration. An increase in the C_P close to the trailing edge and upstream of the plane of the propellers is easily identified, in the form of a hump. This effect is generated by the induced velocity of the propellers, which causes a decrease in the pressure over the wing surface. The hump suddenly decreases close

to the tip of one of the propellers, where the induced flow interacts with the surface of the wing (this depends on the direction of rotation). This effect does not happen in the zone close to the gap between both propellers, where their tip flows interact due to their opposite motions, while one is going down, the other one is moving up and the flow interaction with the wing is lower. Additionally, it is clear that propellers have a strong effect up to the leading edge of the wing. For both cases, the peak of maximum C_P at the leading edge decreases more in front of the tip of the propellers (for instance, close to $y = 0.4\ m$) than in front of the gap between both tips (around $y = 0.15\ m$). But taking a closer look at the peak in front of the gap for both cases, the decrease is higher for the Max-ϕ30 configuration than for the Min-ϕ0 one, because of the larger propeller separation.

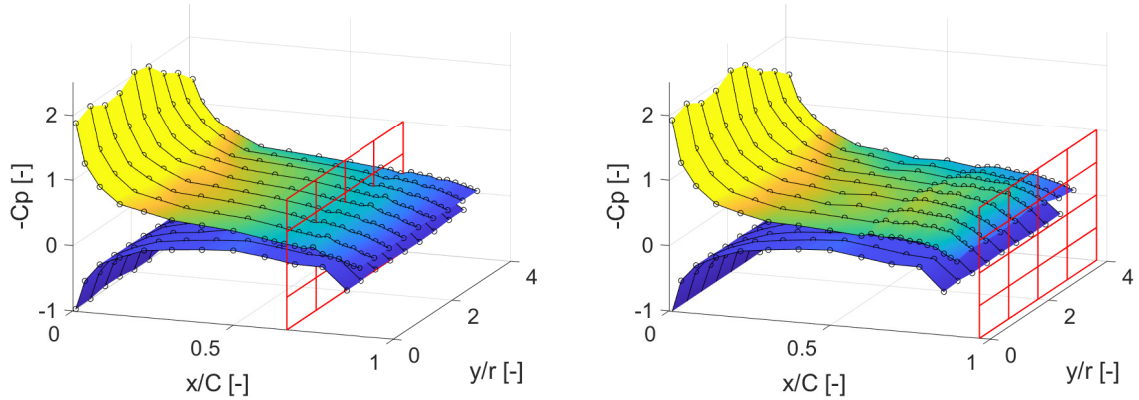

(a) Max-ϕ30 (b) Min-ϕ0

Figure 3.24: 3D C_P for COR propellers. In red is shown the plane of the propellers.

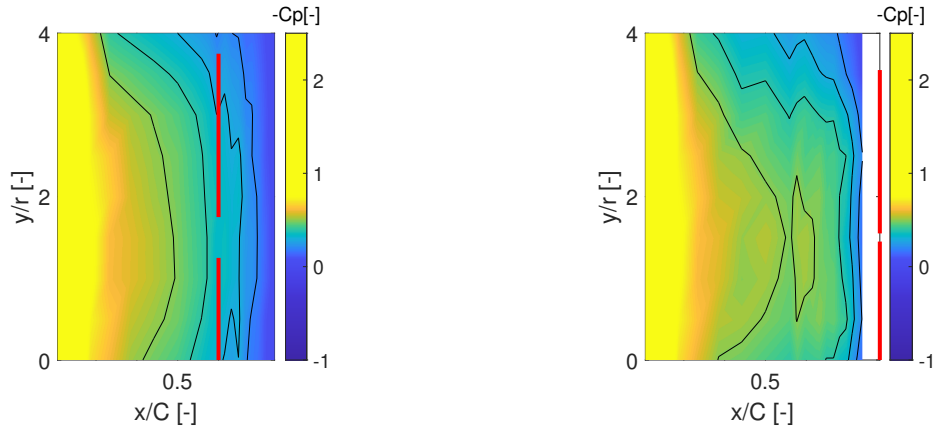

(a) Max-ϕ30 (b) Min-ϕ0

Figure 3.25: Suction side C_P for COR propellers. In red is shown the position of both propellers.

The previous analysis can also be corroborated, more quantitatively, by Figure 3.26. As expected, the propellers over the wing only affect the suction side of the wing and not at all the pressure side. Furthermore, the theoretical values of C_P extracted from the numerical simulation of the setup, in the reference configuration without propellers, superimposed in the figure, are found to be in very good agreement with the measurements.

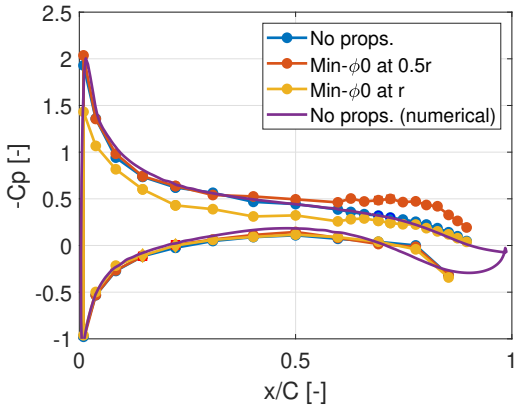

Figure 3.26: Experimental and numerical C_P comparison with COR propellers.

For completing the aerodynamic investigation of the COR propellers, Figure 3.27 shows the variation of the measured forces with the load cell on each propeller for all the tested configurations. Trends and slopes are nearly the same with and without flow, even though the forces are much higher without flow because of the lower advanced ratio J. In both cases, the force produced by the top propeller is higher than that of the bottom propeller, but for the $d2$ cases (large distance between propellers), the difference is less than for the cases of closer propellers. Nevertheless, this is the parameter with more impact in the obtained force for the configurations with $d1$. The phasing ϕ appears as the second more important parameter. Configurations with $\phi = 0$ are more efficient for the $d1$ cases for both propellers. The distance to the wing surface h is less significant than in the previous C_P analysis. However, when the propellers are more separated from the wing, the force differences are less than 3% lower for the $h2$ cases. Finally, the D parameter behaves the same as for the C_P: the closer the system is to the trailing edge, the higher the thrust. Regarding the data of the aerodynamic force measurements, the Min-ϕ0 with and without flow is the best configuration for the flow and no-flow cases, respectively, whereas the configuration of minimum thrust is the Max-ϕ30. In both flow and no-flow cases, the measured thrust with no wing is also plotted; the presence of the wing is found to slightly reduce the thrust, in the conditions of the experiment.

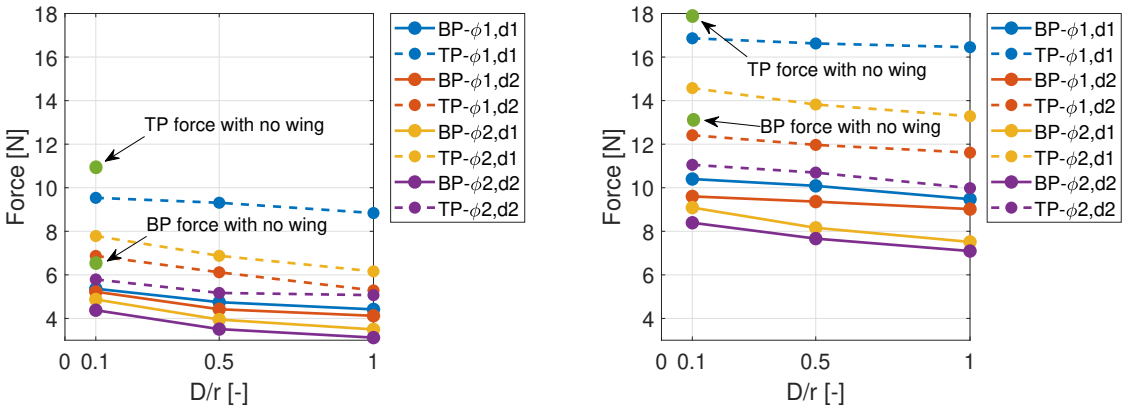

(a) Flow case ($J = 0.95$) (b) No-flow case ($J = 0$)

Figure 3.27: Effect of several parameters on COR propellers thrust with $h1$. BP: bottom prop. and TP: top prop.

Now, the aerodynamic effect of having CTR propellers instead of COR ones is shown in

Figure 3.28, with the C_L results computed from the C_P for each CTR configuration. Only a reduced number of cases were tested with CTR propellers, based on previous observations with COR propellers. As before, in these cases, the D and h parameters remain the most important, whereas the offset angle ϕ and d distance are of secondary importance. However, the trends are similar to the ones in Figure 3.22 for all the cases with $D1$, the C_L increases, and the Min-ϕ0 configuration is still the best regarding the wing C_P. From Figure 3.29, two main changes can be evidenced by looking at the plots and comparing them with Figure 3.24 and Figure 3.25. Firstly, with CTR propellers the hump over the wing is bigger with no significant differences around. Secondly, the peak decrease is lower than before. This means that, in general, the wing C_L is increased by around 7% by using the CTR propellers. Furthermore, the pressure-coefficient map is clearly symmetric with respect to the inter-propeller line.

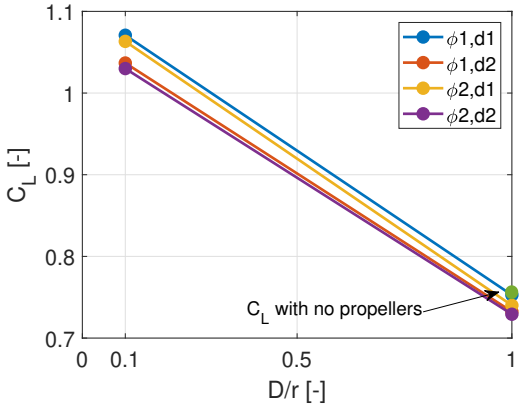

Figure 3.28: Effect of several parameters on the C_L for CTR propellers.

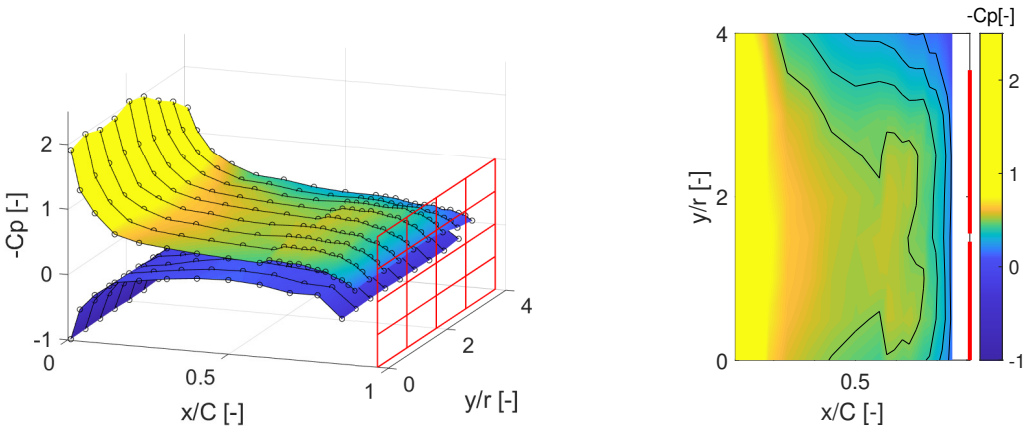

(a) 3D C_P (b) Suction side C_P

Figure 3.29: C_P for Min-ϕ0 configuration with CTR propellers. In red is shown the plane of the propellers.

Additionally, not only the aerodynamic behavior of the wing is better with CTR propellers, but the total force produced by the propellers also increased by an average of 6%, as both propellers produce the same amount of thrust. In general, this aerodynamic improvement can be attributed to the fact that in this case, the blades are not interacting oppositely with each other during their rotation in the zone between the propellers, as both are moving up or down depending on the sense of rotation, meaning that the turbulence created is smaller than with the COR propellers. Figure 3.30 indicates similar trends to the ones with COR propellers but with a force increase. For the CTR cases, the difference between propellers was found around 5%.

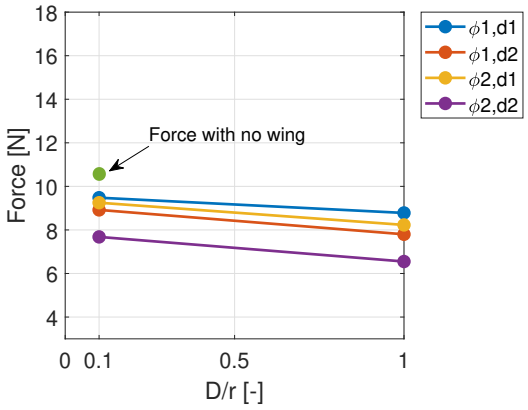

Figure 3.30: Effect of several parameters on CTR propellers thrust with flow (J = 0.95).

Finally, additional tests were performed with 3D-printed ceramic propellers, in order to evaluate the potential of this emerging technology for rotating blade studies. Indeed, relatively easy manufacturing of multiple versions of blades becomes accessible with 3D printing, at much lower cost, which could make it attractive for future experimental parametric studies. Despite the same propeller design, the tests with the ceramic propellers led to different results with respect to the metal ones. For all the tested cases, the ceramic propellers produced around 10% less wing C_p for both the Max-ϕ30 and Min-ϕ0 CTR cases. On top of that, they generated up to 30% less force for the same configurations. This degradation of performances is attributed to the fact that, at the tested rotational velocity, the blades began to deform and curve. Yet the mock-ups are mechanically resistant enough to validate the 3D-printing technology as relevant. This last test, not further detailed here, indicates that it could be used more extensively, provided that stiffer materials are available.

3.5.2 Far-Field Sound Inspection

The effect of the five selected parameters on the OverAll Sound Pressure Level (OASPL) of the COR configurations is depicted in Figure 3.31(a,b) for microphones 4 and 17 and for the 90° antenna position (which would correspond to observers above and below the wing, respectively, case of Figure 3.14). Frequencies below 100 Hz are ignored in the calculation of the OASPL, as attributed to the background noise. As expected, the noise levels are $3-5$ dB higher for Mic 4 than for Mic 17 in all configurations, due to reflection and scattering by the wing, even for configurations where propellers are close to the trailing edge. Even though the results are not far from each other when comparing on one specific microphone, differences and trends can still be identified, especially for the D parameter that makes configurations noisier as propellers approach the trailing edge. The parameter ϕ appears to have a critical effect on the measured OASPL. For all the configurations, the noise is obviously higher when propellers are synchronized with a phase of 30°. The plots show that the d parameter is sensible as well, the less the gap between the blades, the higher the noise. Finally, the distance h between the wing and the blades is not as important as the previous parameters. Nevertheless, the system is around $2-3$ dB less noisy when that distance is large. Clearly, bigger differences can be found depending on the microphone and antenna position selected, as will be shown later in the 3D results.

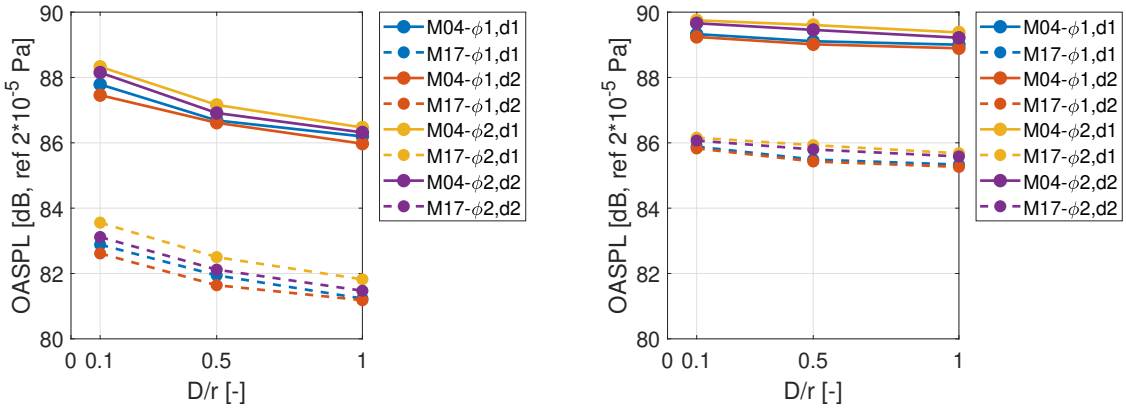

(a) Flow case ($J = 0.95$) (b) No-flow case ($J = 0$)

Figure 3.31: Effect of several parameters on the OASPL ($0.1 - 24\ kHz$) for COR propellers with $h1$. M04 = mic. 4, M17 = mic. 17.

Power Spectral Densities (PSD) of the measured acoustic pressure are compared in Figure 3.32 for the loudest and quietest configurations, Min-ϕ30 and Max-ϕ0, respectively, in the case of advance ratio $J = 0.95$. The comparison is made for microphones 4 and 17. Background-noise and wing-alone noise spectra are added, for a better breakdown of contributing sources. The former is defined as the noise measured with the flow speed of 22 m/s when the wing and the propellers are removed. It includes mixing noise from the shear layers of the wind-tunnel jet, and more dominantly trailing-edge noise from the edges of the nozzle. As mentioned before, the measured noise is higher on the microphone 4, because the wing acts as a shield and reflects most of it. Frequencies below 100 Hz must be ignored as dominated by the background noise. The wing-alone configuration involves background noise and wing noise, the latter including trailing-edge noise and interaction noise with the turbulence in the jet shear-layers, at the junctions with the span-end supports. Wing noise so defined contributes, roughly in the range from 100 Hz to 2 kHz. Propeller-associated broadband noise exceeds wing-and-background noise, typically beyond 400 Hz, with strongly emerging tones at both multiples of the BPF and multiples of the rotational frequency. The masking effect produced by the wing is highlighted in Figure 3.33, for both configurations, in the high-frequency range, where the sound level for the mic. 17 (below the wing) is less noisy by at least $5 - 10\ dB$.

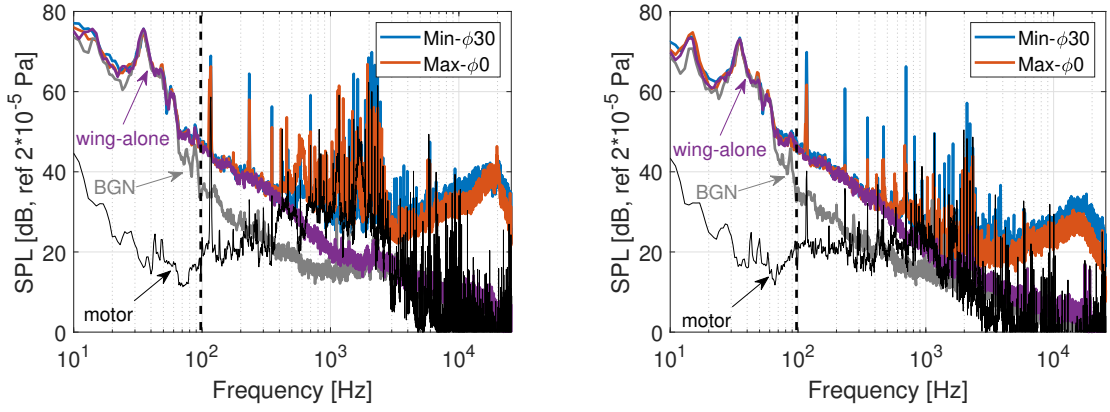

(a) Mic. 4 (b) Mic. 17

Figure 3.32: Sound spectra in louder and quieter configurations for COR propellers.

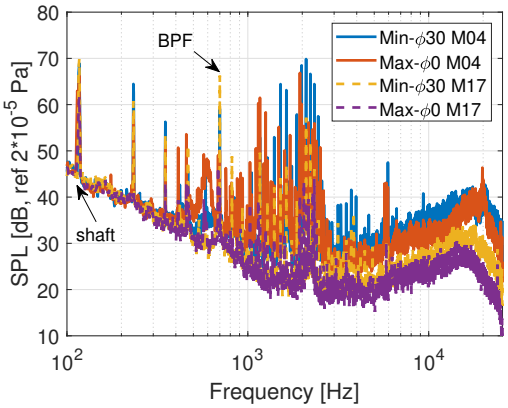

Figure 3.33: Masking effect in louder and quieter configurations with COR propellers.

Broadband propeller noise is more likely to be blade trailing-edge noise. It can be extracted by removing the tones from the propeller-noise spectra after the elimination of wing-and-background noise. An automatic procedure has been applied to suppress all tones related to rotational noise, not only multiples of the BPF but also multiples of the rotational frequency. The result is plotted in Figure 3.34, where a series of residual tones still contaminates the spectrum. This acoustic signature is attributed to motor noise, as confirmed by the raw spectra in Figure 3.32. Finally, the experiment provides reliable propeller broadband-noise data beyond 3 kHz. The complementary processing consists of extracting the tones associated with rotational noise. This is achieved in Figure 3.35, where the BPF harmonics are featured by the thick peaks. The perfect aeroacoustic operation would only generate these tones, therefore other multiples of the shaft frequency are discarded from the analysis. Relative variations of the tonal noise levels are clearly observable at the first five BPF harmonics, numbered on the plots. In any case, even though the BPFs differences are not the same for both sides of the wing in Figure 3.35, and especially for the first three, the Max-ϕ0 configuration BPFs tones are around $10-20$ dB quieter than the Min-ϕ30 ones.

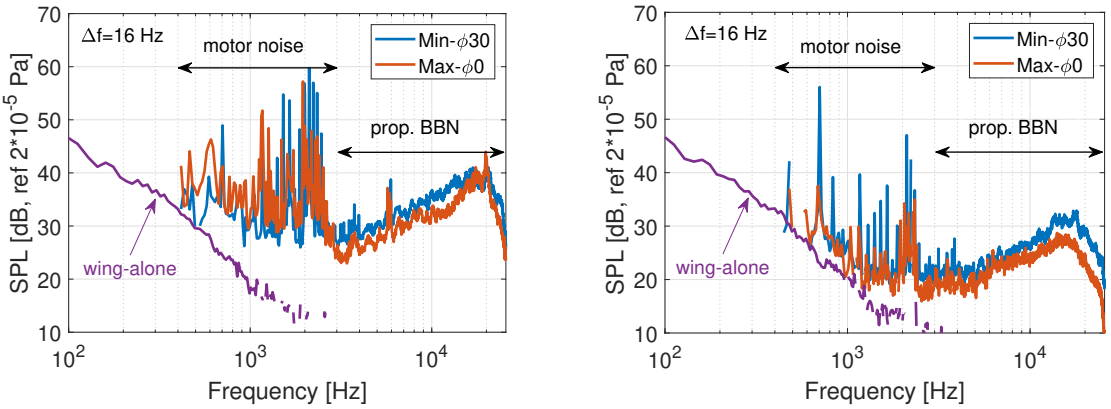

(a) Mic. 4 (b) Mic. 17

Figure 3.34: Broadband noise in louder and quieter configurations with COR propellers.

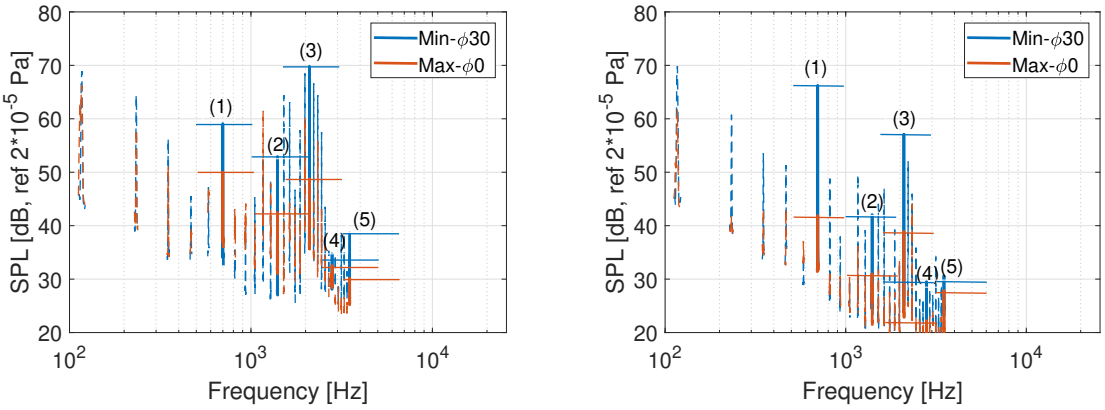

(a) Mic 4 (b) Mic 17

Figure 3.35: Tone levels in louder and quieter configurations with COR propellers.

Apart from the differences in the tones, the directivity (see Figure 3.36) plots in Figure 3.37 evidence that the level at the BPF can increase up to 25 dB above and below the wing for some antenna and microphone positions, in the noisiest configuration. However, the pressure side exhibits the larger differences between the noisiest and quietest configurations. This will be addressed later in this chapter by analyzing three-dimensional sound maps.

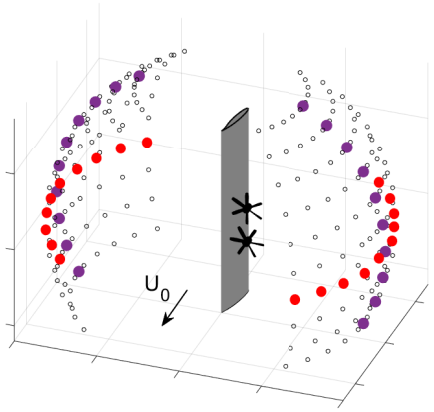

Figure 3.36: Selected microphones for directivity analyses. In red: microphones 4-17 and all antenna positions. In purple: 90° antenna position and all microphones

Sound spectra in the same configuration (Min-ϕ0) with and without flow are compared in Figure 3.38. In those cases, for both microphones, the sound is louder at zero advance ratio than for $J = 0.95$, for the mid and high-frequency range, for both broadband (see Figure 3.39) and tonal (see Figure 3.40) contents. This is related to the much higher thrust produced by the propellers, and the stronger loading conditions on the blades. Low-frequency noise is higher in Min-ϕ0 with flow because the wing is aerodynamically loaded and consequently generates noise. This frequency range has been identified as the wing contribution in Figure 3.32, which is not involved in the no-flow case. For mid frequencies at mic 4, there is still a very significant effect of the additional tonal noise due to the motor. Additionally, the directivity maps in Figure 3.41 will confirm that the total sound increases in the no-flow case in both the suction and pressure sides of the wing for several antenna and microphone positions. It is worth noticing that for the no-flow case, the directivity patterns are almost a mirror of each other in the pressure and suction side for both plots, but this is not the same for the flow case, suggesting that free-stream

velocity also plays a role in directivity patterns.

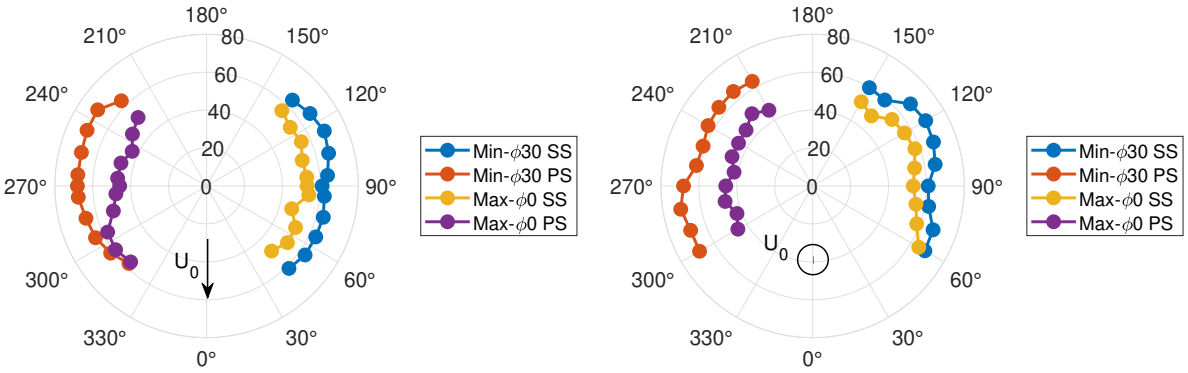

(a) Plane parallel to the wing airfoil (b) Plane parallel to the propeller discs

Figure 3.37: 2D directivity patterns of the 1st BPF (700 Hz) in louder and quieter configurations with COR propellers. SS: suction side and PS: pressure side.

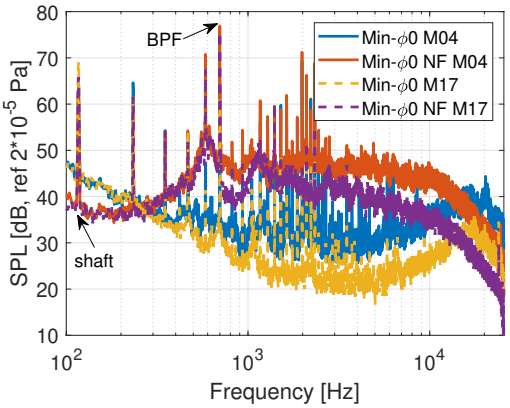

Figure 3.38: Masking effect in flow and no-flow (NF) configurations with COR propellers.

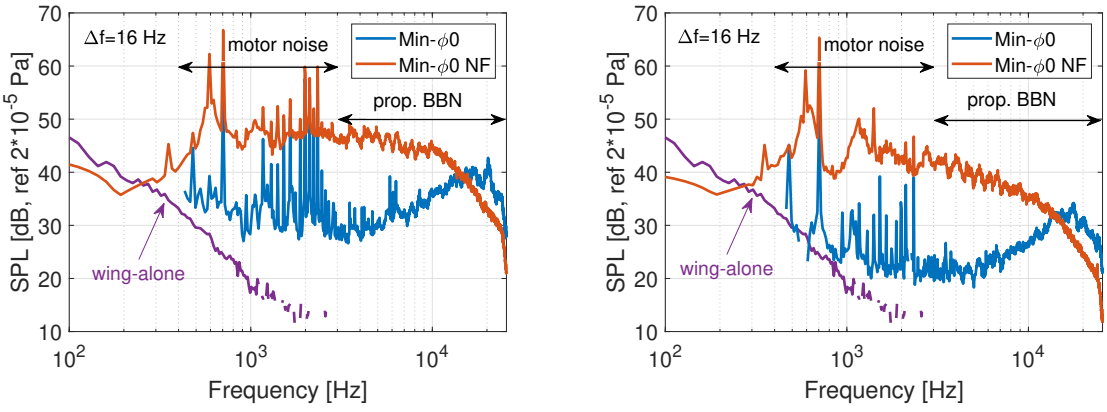

(a) Mic 4 (b) Mic 17

Figure 3.39: Broadband noise spectra in Min-ϕ0 flow and no-flow (NF) configurations with COR propellers.

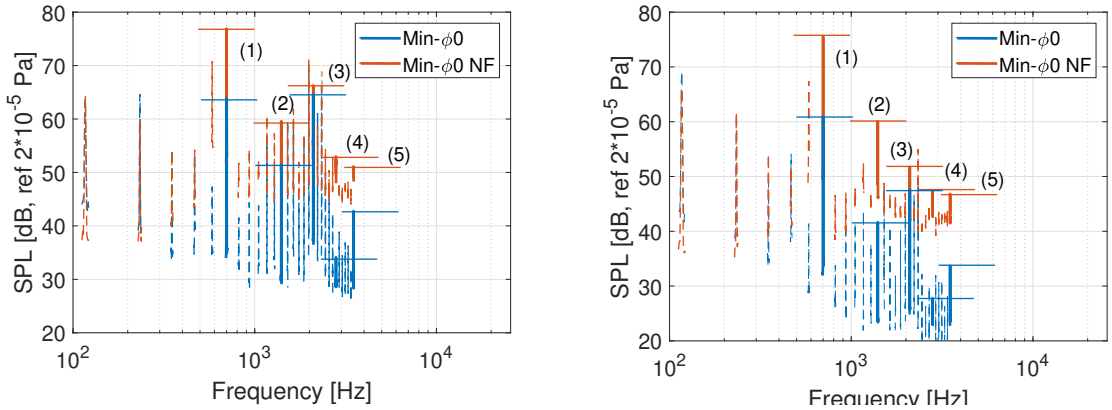

(a) Mic 4 (b) Mic 17

Figure 3.40: Tone levels in Min-ϕ0 flow and no-flow (NF) configurations with COR propellers.

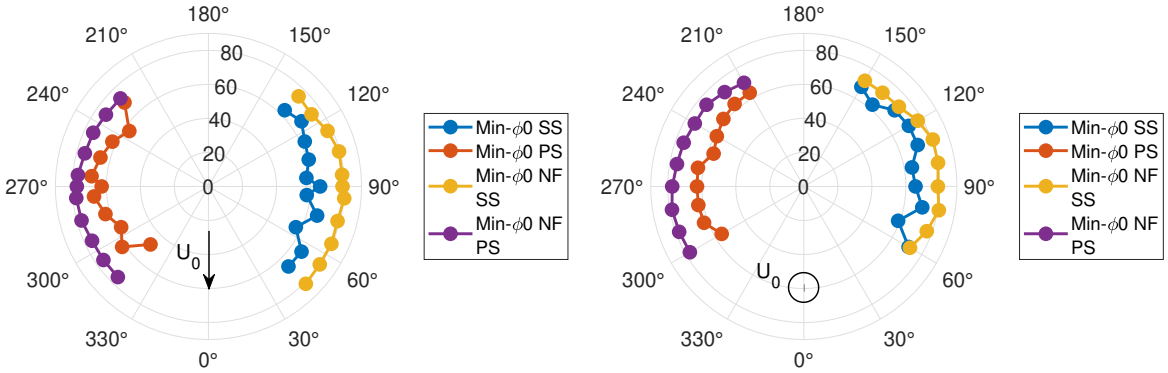

(a) Plane parallel to the wing airfoil (b) Plane parallel to the propeller discs

Figure 3.41: 2D directivity patterns of the 1st BPF (700 Hz) in flow and no-flow configurations with COR propellers. Maximum-noise configuration. SS: suction side, PS: pressure side, and NF: no flow.

The arc antenna of microphones allows the investigation of the three-dimensional directivity of noise components, which is of primary interest for the assessment of installation effects. Indeed, in real operating conditions, annoyance related to community noise of air vehicles is a matter of relative source-observer positioning. The directivity is illustrated in the following Figure 3.42 and Figure 3.43 by means of sound-level maps on the portion of the sphere accessible to the microphones of the antenna. The selected results are for the most representative configurations, regarding the aerodynamic and acoustic analyses for the 1st BPF tone and the broadband noise, respectively. They correspond to 20 microphone angles on the arc antenna and 11 antenna positions, leading to the measuring points featured by symbols $\circ$ in the figures. Drawings of the wing and propellers in their real arrangements are added to the plots for clarity.

Comparing results in Min-ϕ30 configuration with and without the wing in Figure 3.42(a,b), shows that for both portions of the sphere, sound at the BPF significantly increases in the presence of the wing, because of sound reflection and regeneration for the microphones located over and under the wing, respectively. In both cases, the sound is also higher for microphones 5 to 9 which are shifted in the direction of rotation of the propellers, as well as for a symmetrical area on the opposite side. This tends to feature a dipole-like pattern with an axis tilted in the direction of rotation. The configuration Min-ϕ30 is typical of a significant amplification by installation effect, because of the close vicinity of the blade tips to the trailing edge of the wing.

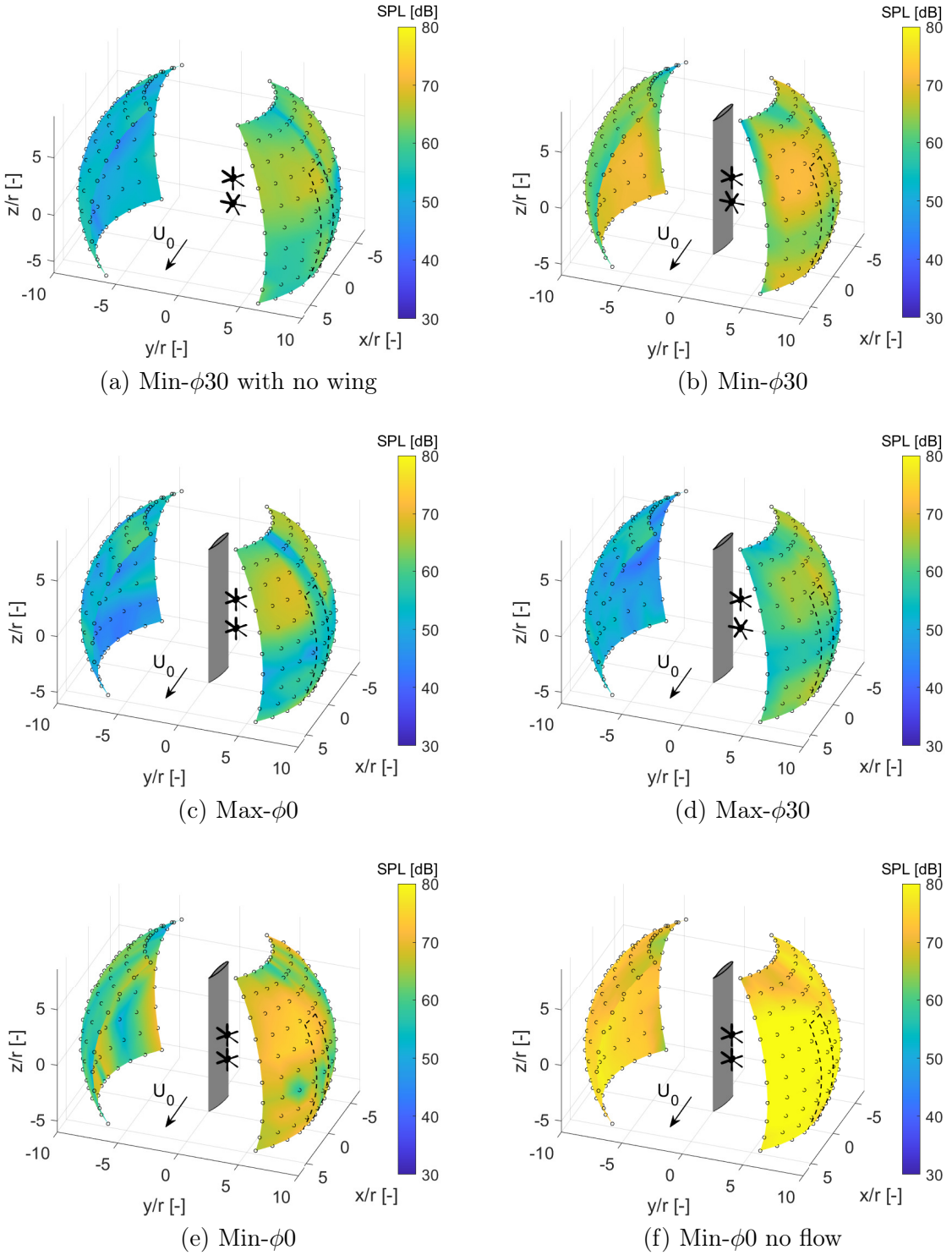

(a) Min-ϕ30 with no wing

(b) Min-ϕ30

(c) Max-ϕ0

(d) Max-ϕ30

(e) Min-ϕ0

(f) Min-ϕ0 no flow

Figure 3.42: 3D directivity patterns of the 1st BPF (700 Hz) in configurations with COR propellers.

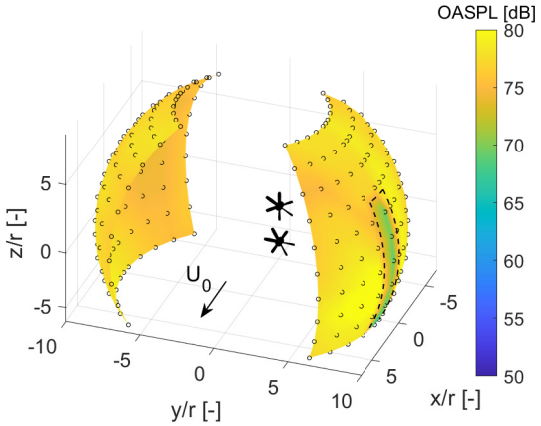

(a) Min-ϕ30 with no wing

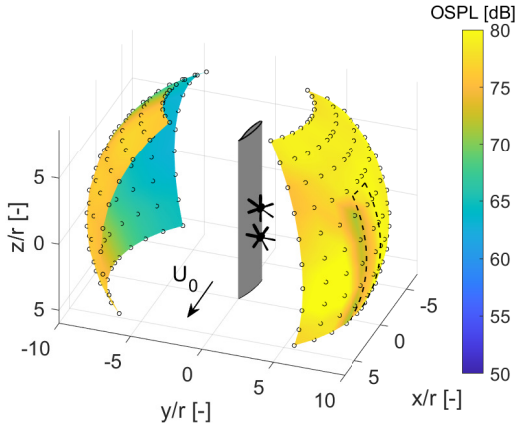

(b) Min-ϕ30

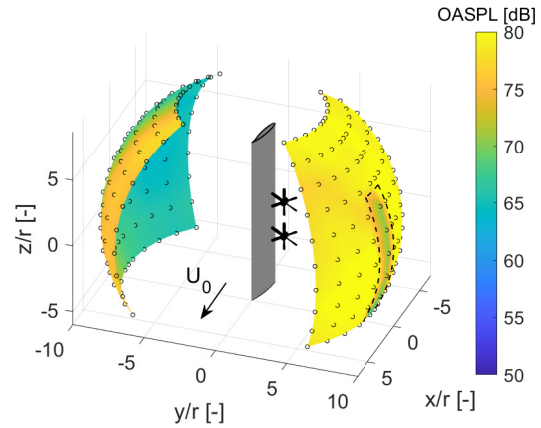

(c) Max-ϕ0

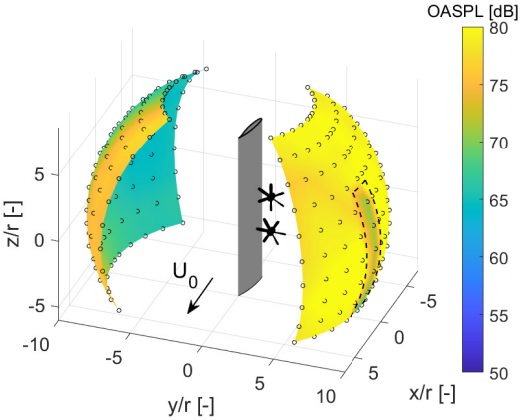

(d) Max-ϕ30

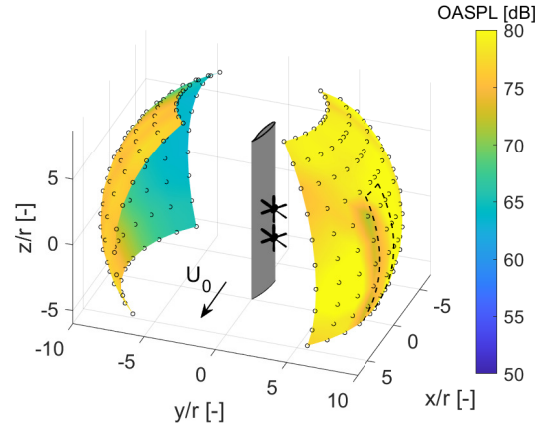

(e) Min-ϕ0

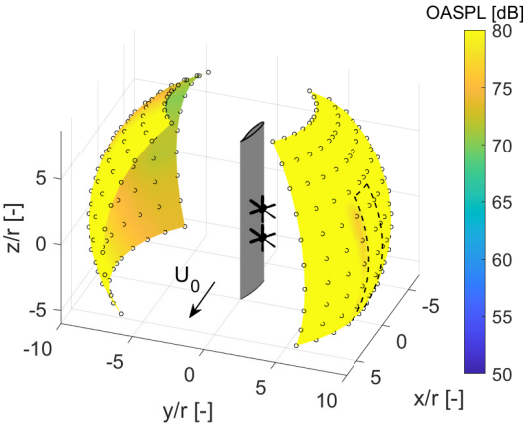

(f) Min-ϕ0 no flow

Figure 3.43: 3D directivity patterns of broadband-noise OASPL ($4 - 24\ kHz$) of configurations with COR propellers.

The same tilting effect of the dominant directivity lobe seems to be also evidenced in all configurations. Large differences are also found between Min-ϕ30 and Max-ϕ0, the loudest and quietest configurations with flow, respectively. Figure 3.42(c) illustrates a general fact: the larger the distance between the propellers and the wing (from the surface and from the trailing edge), specifically for $\phi = 0$, the lower the tonal noise, for both sides above and below the wing. Changing the ϕ parameter between Max-ϕ0 and Max-ϕ30 produces significant changes (Figure 3.42(d)). The main tilted directivity lobe (dominant yellow area) is reduced in Max-ϕ30, making it better globally. But the sound is globally lower below the wing in Max-ϕ0, making $\phi = 0$ the best option for reducing the tonal noise. Finally, Figure 3.42(e,f) illustrate the effect of the flow. The tonal noise is globally increased by a large amount, on both sides of the wing and in all directions, when $J = 0$. This confirms the expectation that static operation is substantially louder than in-flight.

A separate analysis dedicated to the broadband noise makes sense, in particular, because wing-trailing-edge scattering is totally different for uncorrelated sources and for the modal sources typical of propeller tonal noise [91]. The same three-dimensional directivity inspection as for the tonal noise at the BPF is presented in Figure 3.43, for an OASPL calculated in the 4-24 kHz frequency range, representative of propeller broadband noise. These plots stress the strong effect of the wing for masking the noise when the propellers are placed above, even for cases of the highest tonal content. Apart from the Min-ϕ30 case without the wing in Figure 3.43(a), for which there is no masking effect, other configurations exhibit a very significant noise masking below the wing (keeping in mind that this also corresponds to a significant sound reflection above the wing). In the zero advance ratio case, illustrated in Figure 3.42(f), the broadband noise is also found much higher than for the ratio 0.95, as for the tonal noise. It is worth noting that the narrow area of lower sound level, limited by the dotted lines on the right side of all plots in Figure 3.42 and Figure 3.43, corresponds to some masking by the mast supporting the propulsive system, previously shown in Figure 3.4. This area must be ignored in the analysis.

Apart from the far-field sound inspection with COR propellers, an additional analysis with CTR propellers follows. Firstly, from Figure 3.44 can be concluded that noise levels are higher for both CTR configurations with flow regarding the results presented in Figure 3.31. Additionally, even though the trends with ϕ angle and d distance are the same as before, the CTR cases do not present significant differences when changing the D parameter for Mic 4 and Mic 17. Figure 3.45 shows that, except for the motor noise, the broadband noise with CTR propellers decreases for both microphones. This effect could be attributed to the fact that now the blade tips of both propellers move in the same direction, therefore the tip-to-tip interaction is reduced, as well as the associated broadband noise. In contrast, the BPF tones have higher levels (see Figure 3.46). This is probably because, when the tips of both propellers are in their closest position to each other, the associated forces have the same orientation for counter-rotating propellers. The net combined force is higher, which increases the tone levels when compared to the co-rotating case, even though the tip-to-tip interaction is reduced. Yet further investigation is needed to confirm the interpretation. Directivity patterns shown in Figure 3.47 are also in agreement with the aforementioned CTR propellers results. Although for some microphones and antenna positions, the sound seems to be equal, for most of the radiation angles the noise levels are higher for the CTR propellers in both the pressure and suction sides.

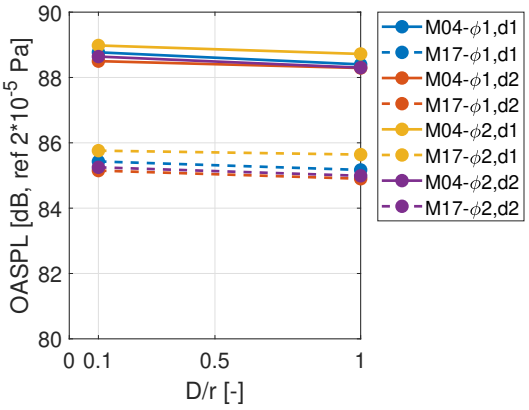

Figure 3.44: Effect of several parameters on the OASPL ($0.1-24\ kHz$) for CTR propellers. M04 = mic. 4, M17 = mic. 17.

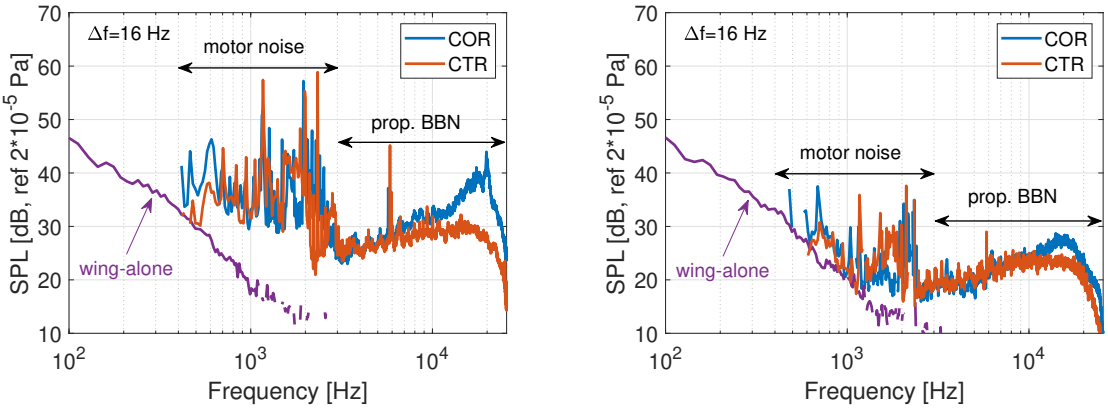

(a) Mic 4 (b) Mic 17

Figure 3.45: Compared broadband noise spectra in Max-ϕ0 configurations, in CTR and COR cases.

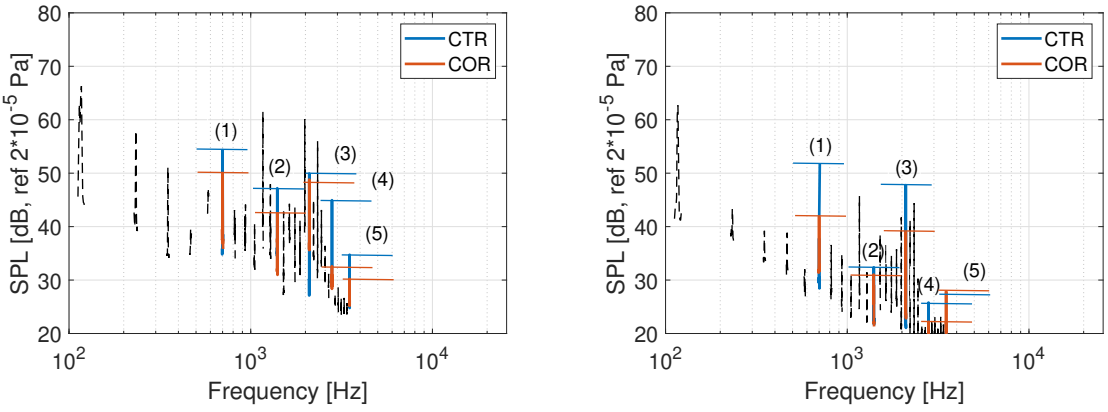

(a) Mic 4 (b) Mic 17

Figure 3.46: Compared tone levels in Max-ϕ0 configurations, in CTR and COR cases.

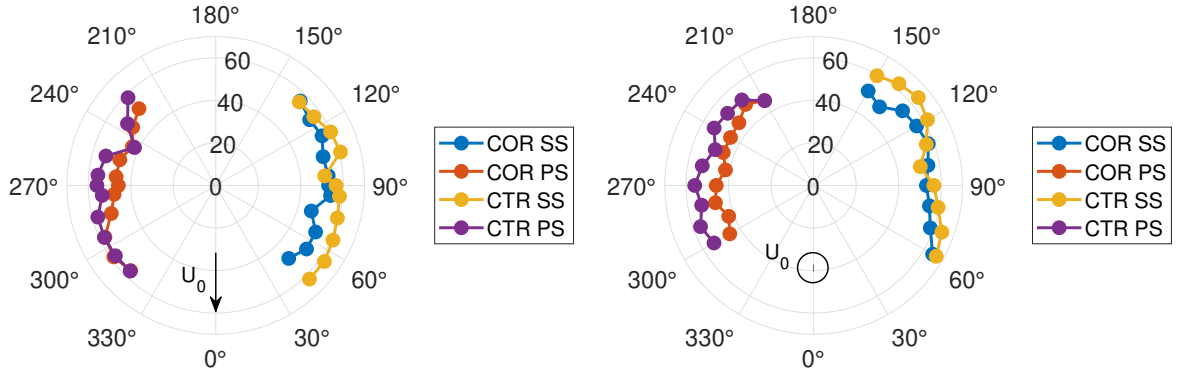

(a) Plane parallel to the wing airfoil (b) Plane parallel to the propeller discs

Figure 3.47: 2D directivity patterns of the 1st BPF (700 Hz) in Max-ϕ0 configurations, for CTR and COR arrangements. SS: suction side and PS: pressure side.

The same trends are confirmed in 3D in Figure 3.48(a,b) by comparing with Figure 3.42(c) and Figure 3.43(c). On the one hand, looking at the first BPF in Figure 3.48(a), it can be verified that the Max-ϕ0 configuration is louder with CTR propellers than COR propellers above and below the wing, whereas, on the other hand, the broadband noise is reduced. The first BPF tone increase with CTR propellers is around $5-10$ dB for microphones 4 and 17, respectively for the Max-ϕ0 case. The same trends regarding broadband noise, tones, and directivity, not shown here, are also obtained when comparing the Min-ϕ30 with COR and CTR propellers.

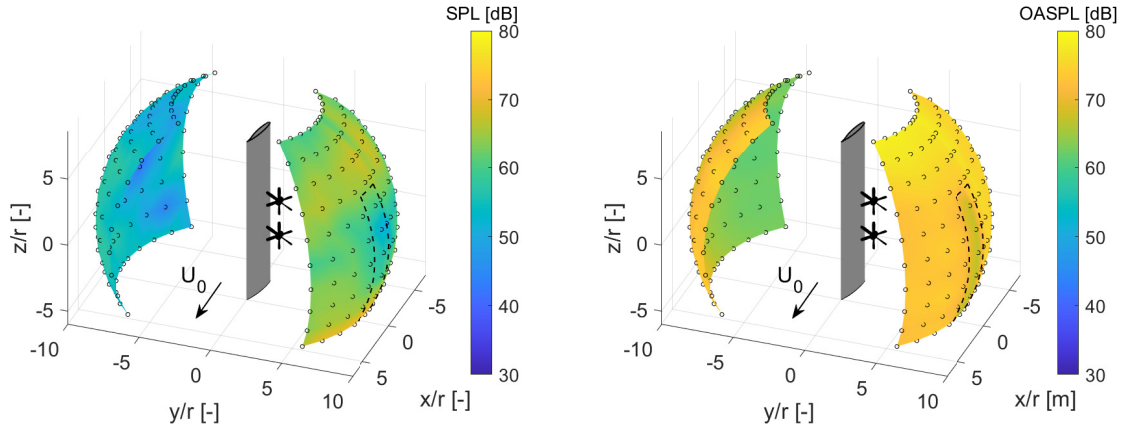

(a) 1st BPF (700 Hz) (b) Broadband-noise ($4-24$ kHz)

Figure 3.48: 3D directivity patterns of Max-ϕ0 configuration with CTR propellers.

Based on experimental results, it is clear that the optimal configuration regarding aerodynamic performance is detrimental to acoustic signature and vice-versa. However, an offset phase of $\phi = 0$ seems to be positive for both. Additionally, COR rotors demonstrate greater noise reduction potential than CTR rotors, as previously found in other investigations [162, 163], whereas the aerodynamic performance is higher with CTR.

Finally, the far-field sound from ceramic-printed propellers was also investigated. From Figure 3.49 is clear that for both microphones, the broadband noise increases with the ceramic propellers. This could be related to the already mentioned enhanced tip-to-tip interaction generated because of the possible additional curvature of the ceramic propellers at the high RPM achieved in the test.

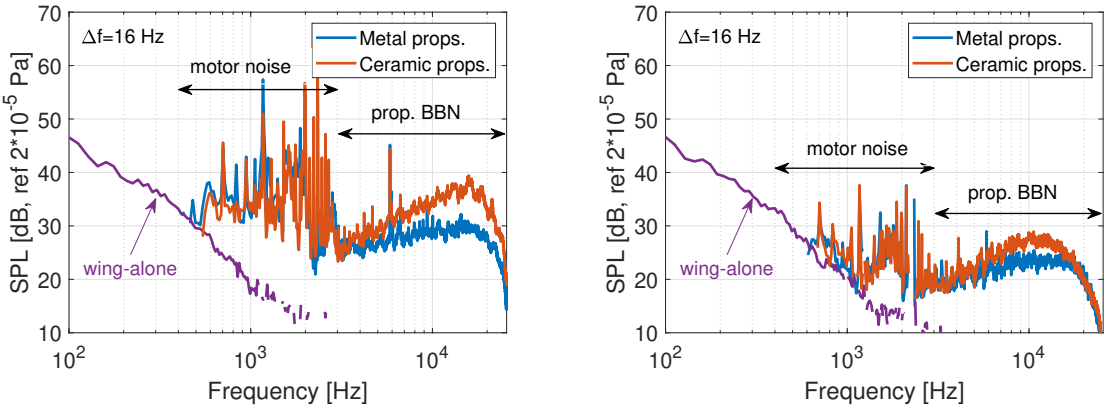

(a) Mic 4 (b) Mic 17

Figure 3.49: Broadband noise spectra in CTR Max-ϕ0 configurations. Comparison between metal and ceramic-printed.

The previous interpretation is also related to the results in Figure 3.50, where for most of the microphones and antenna positions, the BPF tone is similar or even lower with the ceramic blades, as the aerodynamic performance of the blades is not as good as with metal blades.

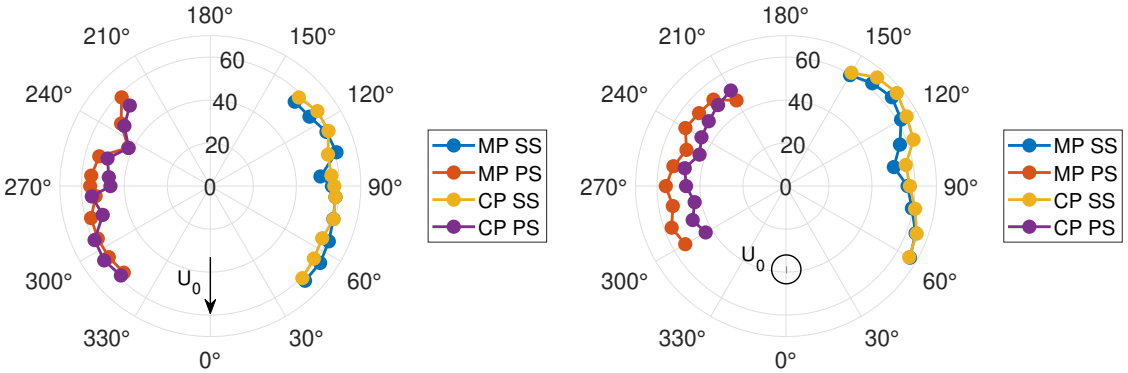

(a) Plane parallel to the wing airfoil (b) Plane parallel to the propeller discs

Figure 3.50: 2D directivity patterns of the 1st BPF (700 Hz) in CTR Max-ϕ0 configurations. Comparison between metal (MP) and ceramic-printed (CP) propellers. SS: suction side and PS: pressure side.

This chapter has demonstrated that wind tunnel tests can capture clear and pronounced noise and performance differences among the configurations. The experimental protocol is confirmed as well-suited for parametric studies of installation effects, on the one hand. On the other hand, the sensibility of the results suggests that many degrees of freedom can be explored for the identification of some optimal configurations. It is now necessary to reproduce the same by analytical means. The mathematical formulations presented in the following chapter will provide the theory for a more quantitative insight into the ranking between steady and unsteady noise source mechanisms presented in chapter 5. Rotating-blade noise modeling is based on the generic formula for a rotating dipole.

4 Analytical Approach I: Theory

Summary

Analytical models are understood as a way of exploring either promising or detrimental configurations at the early design stage, typically when a rotating-blade architecture has still unspecified geometrical details. Their lack of accuracy is balanced by their short computational times and minimum cost. Furthermore, they highlight the underlying physics. This approach might be integrated as well with optimization algorithms. This chapter introduces the theoretical background of the selected propeller noise analytical modeling in sections 4.1, 4.2, and 4.4. Then, the sound-scattering model is described in section 4.5. A novel analytical formulation for a more accurate noise calculation is reported in section 4.6. Finally, the analytical validation results and discussions are presented in section 4.7.

Contents

4.1 Analytical Propeller Noise

When analytical methods are used, the noise radiated by a propeller in a free field is often predicted, relying on Ffowcs Williams & Hawking's formulation of the acoustic analogy. The analogy states that, from the standpoint of a distant observer, the moving blades can be replaced by equivalent monopoles, dipoles, and quadrupoles [106, 164]. These types of sources correspond to thickness noise, loading noise, and flow noise, respectively. The analogy equation is solved with the free-space Green's function, either in the time domain or in the frequency domain. This formulation became a vital background, particularly for analytical modeling as well as for the derivation of scaling laws based on dimensional analysis. The mathematical formulation was in

the continuation of Lighthill's acoustic analogy [165] and its extension by Curle [166] and Lowson [167].

In installed configurations, the diffraction of propeller noise by the airframe or surrounding surfaces must be explicitly considered, because it can strongly restructure the sound field. For instance, the effect of having distributed sources interacting with surfaces has been identified as a very efficient mechanism by Crighton and Leppington [168], Doak [169], Howe [170], or Powell [171]. In this case, the wave or Helmholtz equation must be solved with additional boundary conditions imposed on the surfaces. In a general case, this is achieved with numerical methods. Alternatively, a tailored Green's function can be used, provided that the geometry of the surfaces can be simplified, preserving the dominant scattering effects. This enables the development of a complete analytical approach, including source modeling and diffraction. The present study aims to demonstrate the usefulness of this approach, particularly at the early design stage of a mechanical system, in the context of innovative, installed, and distributed propulsion systems.

In essence, the analytical approach has to start with the definition of a generic configuration, in which a propeller and a scattering surface are arranged with variable positioning parameters. The problem is formulated in the frequency domain because diffraction is a matter of comparing dimensions and wavelengths. For mathematical tractability, in particular separation of variables and homogeneity in the expression of boundary conditions for the Helmholtz equation, the surface is defined along iso-values of the coordinate system. The surface must also be compatible with a uniform fluid motion, corresponding to forward flight. The approach presented in the following sections for mimicking the real configuration is graphically explained in Figure 4.1. As a first step, the source model includes the estimation of steady loading and blade loading harmonics to determine the blade forces acting as equivalent dipoles, and a linear combination of equivalent source modes for modeling the propellers. The second step is the propagation model with the half-plane Green's function for predicting the sound scattering by the wing a finite-chord correction procedure, which allows more accurate results [91]. It is important to state that additional blade loading harmonics generated by the aerodynamic interaction between both propellers and between the propellers and the wing are not considered in the present formulation. Apart from the steady loading, the source model only includes the periodic loads produced by the distortions around the pylons of the propellers.

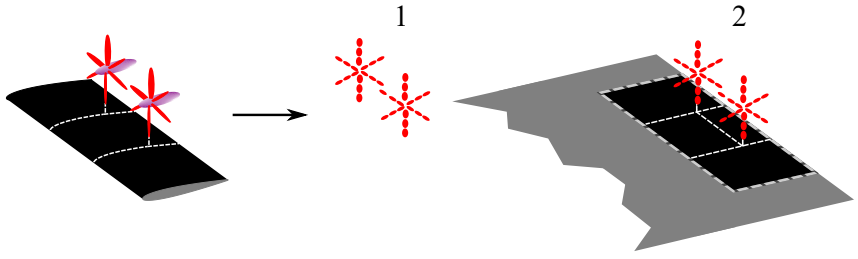

Figure 4.1: Analytical approach graphically explained in three steps.

4.2 Rotating Dipole

Propeller tonal noise is radiated at multiples of the BPF, noted $\omega/(2\pi) = mB\,\Omega/(2\pi)$, where ω stands for the angular rotational frequency, m an integer and B the number of blades. The noise radiated by a propeller with the real flow corresponding to an installed configuration can be formulated in free-field, thus the true sound sources and their radiation (ignoring additional scattering) are predicted relying on Ffowcs Williams & Hawking's formulation of the acoustic

analogy [106, 164], reduced to the dipole source terms. The tonal noise is formulated in the frequency domain, and the far-field is expressed in a way suited to highlight the modulation by the azimuthal flow distortions and interference properties between blades. The observer location is defined by its spherical coordinates (R_{obs}, Θ_{obs}, and ϕ_{obs}) in the reference frame attached to the circular path of the segment of radius r, where R' is the exact source-to-observer distance. At the multiple of order m, the general expression for the far-field complex-valued sound-pressure amplitude at observer point $\mathbf{x_{obs}}$ reads as follows, with the convention $\mathrm{e}^{-\mathrm{i}\,\omega t}$ for monochromatic waves:

$$p_{mB}(\mathbf{x_{obs}}) \;=\; \frac{\mathrm{i}\,k_{mB} r}{4\pi} \sum_{s=-\infty}^{\infty} F_s(r) \left\{ \cos\Theta_{obs}\, \cos\gamma(r)\, \mathrm{G}^{(1)}_{mB-s} + \sin\Theta_{obs}\, \sin\gamma(r)\, \mathrm{G}^{(2)}_{mB-s} \right\} \tag{4.1}$$

$$\text{with} \quad \mathrm{G}^{(j)}_n \;=\; \frac{\Omega}{2\,\pi} \int_0^{2\pi/\Omega} \mathrm{G}_j(t)\, \mathrm{e}^{\mathrm{i}\,n\Omega t}\, \mathrm{d}t\,, \quad \mathrm{G}_1(t) \;=\; \frac{\mathrm{e}^{\mathrm{i}\,k_{mB} R'}}{R'^2} \left[1 - \frac{1}{\mathrm{i}\,k_{mB} R'} \right] ,$$
$$\text{and} \quad \mathrm{G}_2(t) \;=\; \sin(\Omega t - \phi_{obs})\, \mathrm{G}_1(t)$$

where $k_{mB} = mB\,\Omega/c_0$. The stagger angle $\gamma(r)$ is defined as the blade-segment inclination with respect to the rotational plane, or equivalently as the angle between the force and the axial direction. The complex-valued factors $F_s(r)$ are the Fourier coefficients of the periodic force on the blade segment, referred to as the BLHs (see Figure 4.2). The expression is valid everywhere in space, as discussed, for instance, by Roger & Moreau [172, 76]. It holds for a pure axial-flow architecture, both terms in the brackets corresponding to the axial and tangential components of the blade force, respectively.

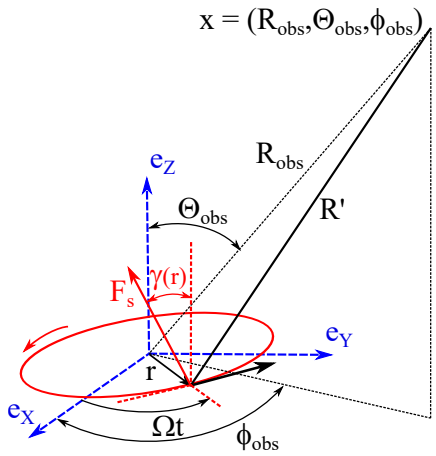

Figure 4.2: Reference frame attached to a rotating blade segment and associated coordinates.

Each term of the sum defines a free-field radiation mode of order $n = mB - s$. Its radiating structure expresses the coherent character of the sound sources and the associated interference between blades. The interference is better emphasized with the acoustic and geometric far-field approximation, corresponding to $k_{mB} R' \gg 1$ and leading to the following expression, with $k_{mB}\, r = mB\, M_t$, where $M_t = \Omega r/c_0$ is the tangential Mach number at the current radius. J_n stands for the Bessel function and the order n appears as the number of azimuthal lobes of the mode.

$$p_{mB}(\mathbf{x_{obs}}) = \frac{\mathrm{i}\,B\,k_{mB}}{4\pi\,R}\,\mathrm{e}^{\mathrm{i}\,k_{mB}R}\sum_{s=-\infty}^{\infty} F_s(r)\,\mathrm{e}^{\mathrm{i}\,n\,(\phi_{obs}-\pi/2)}\mathrm{J}_n\left(mB\,M_t\,\sin\Theta_{obs}\right)\times \left[\cos\Theta_{obs}\,\cos\gamma(r) - \frac{(mB-s)}{mB}\frac{\sin\gamma(r)}{M_t}\right] \tag{4.2}$$

The contribution of the near field terms is neglected in Equation 4.1; nonetheless, it is essential for installation-effect studies. Therefore, introducing the formalism of source modes (see next section) as an alternative to Equation 4.1 is well suited to illustrate the formation of acoustic wavefronts from the near-field of distributed sources. The far-field expression, Equation 4.2, highlights which BLHs are effectively contributing to a given BPF harmonic. Indeed, the Bessel function rapidly drops to zero as its order exceeds the value of its argument in absolute values. Thus, it operates as a "band-pass" filter on the BLH spectrum. Furthermore, Equation 4.2 is used to compare predictions with measurements directly, usually carried out with far-field microphones.

4.3 Blade-Design Considerations

Without going into aerodynamic details, the design of an axial-flow rotor is aimed at ensuring almost uniform axial speed at any radius, keeping an acceptable angle of attack on the blades. This is achieved by twist, being the angle $\gamma(r)$ larger at the hub and smaller at the tip. The aerodynamic conditions at different cross-sections are expressed by the velocity triangle, illustrated in Figure 4.3(a) for the extreme hub and tip radii in unwrapped representation.

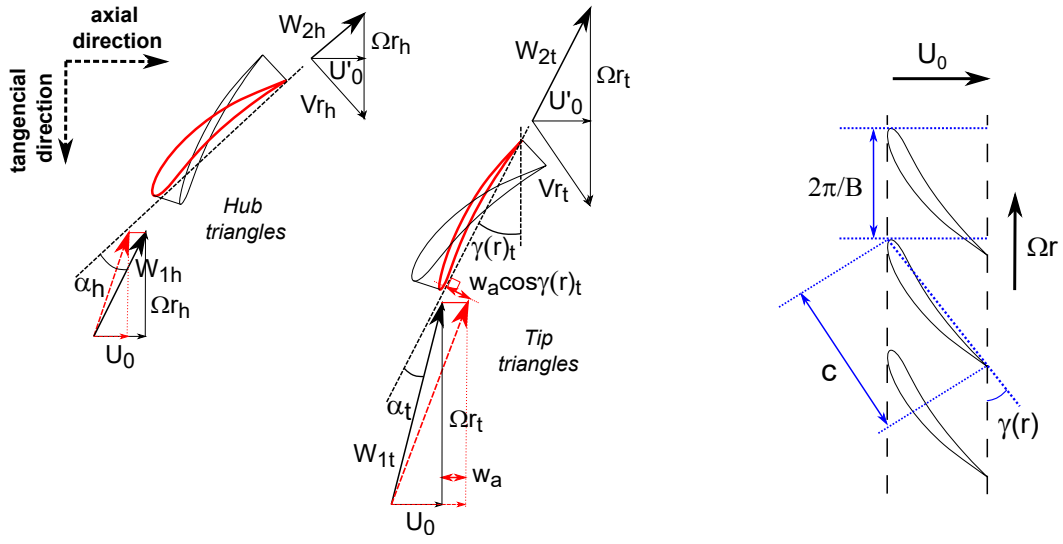

(a) Velocity triangles at the blade hub and tip (b) Unwrapped representation of a strip

Figure 4.3: Blade parameters and related definitions. Red triangles refer to distortions in a twisted blade due to a decrease (hub) or an increase (tip) in the axial flow speed.

For an incompressible flow, the axial velocity would be uniform. The tangential speed of the blades Ωr is much larger at the tip ($r = r_t$) than at the hub ($r = r_h$). The velocity triangle at exit is used for acoustic purposes only if the impingement of the rotor wake interacts with downstream structures which generates noise. For propeller noise due to in-flow distortion, only

the velocity triangle at the inlet and its azimuthal variations are of interest. They correspond to time variations of the angle of attack relative to the blades, thus inducing unsteady aerodynamic loads responsible for sound emission. A blade-response model will be discussed in chapter 5. The sweep angle, defined as the tangential deviation of the mid-chord point of a blade section from pure radial piling, and the lean parameter, defined as the deviation of blade cross-sections from radial piling in the axial direction, are not considered in the present investigation.

Key features of the unsteady aerodynamics of a propeller blade operating in inflow distortions are clearly understood from the two velocity triangles previously shown in Figure 4.3(a). At inlet the triangles express the relationship between the local axial flow speed U_0 at the considered azimuth of the blade section, the tangential speed Ωr, and the resulting relative speed as experienced by the blade, noted $W_{1(h,t)}$. The direction of the latter defines the angle of attack $\alpha(h,t)$ concerning the chord line. The same velocity triangle at the rotor outlet relates the relative velocity at exit $W_{2(h,t)}$, the same tangential speed, and the absolute velocity $Vr_{(h,t)}$ in a stationary reference frame. The tangential projection of Vr determines the swirl induced by the rotor. Any in-flow distortion described as an azimuthal variation w_a of the axial flow speed causes deformations of the velocity triangle as seen by the blade, thus variations of the angle of attack and the modulus of the relative velocity vector. This is illustrated by the red triangles in the figure. The framework of the linearized theories of unsteady aerodynamics introduced later assumes in particular that the angle of attack, the camber, and the disturbance w_a are small. Therefore W_1 is not far from parallel to the chord and the direction of the deficit w_a is not far from perpendicular to the chord, especially at the tip where the angle is smaller. This implies that the operating point is close to the best-efficiency point.

Rotor-noise modeling usually relies on the approach in which the rotor and its surrounding flow are split into annular strips that can be treated independently. A strip of mean radius r is bounded by adjacent cylindrical cuts at some radii $r - \Delta r/2$ and $r + \Delta r/2$. For mathematical tractability, the strip is unwrapped as illustrated in Figure 4.3(b), and the blades are represented as an infinite cascade of airfoils to ensure the periodicity of the system. This implies that the flow features are assumed spanwise homogeneous in the strip and imposed by the mean-velocity triangle at radius r in Figure 4.3.

4.4 Source-Mode Expansion

According to the general rotor tonal-noise formulation, Equation 4.1 and Equation 4.2, the sound radiated at the frequency $mB\,\Omega/(2\pi)$ by the array of the same element repeated on all blades is expressed as a sum of spinning radiation modes. Each isolated mode is defined by its amplitude, the number of lobes n, and azimuthal phase velocity $\Omega_s = mB\,\Omega/n$. Its acoustic field can be reproduced from a continuous circular distribution of stationary point dipoles of the same radius r as the true source of the mode, provided that a proper phase shift is applied to the distributed dipoles and their orientation is defined accordingly. Such a distribution is called a source mode. For the source mode n associated with the BLH of order s, the strength of the dipole source at angle α_d on the circle and at time t reads as follows:

$$F_t(\alpha_d, t) = F_d \mathrm{e}^{-\mathrm{i}\,mB\,\Omega t} \quad \text{with} \quad F_d = F_s \mathrm{e}^{-\mathrm{i}\,n\alpha_d}$$

where F_s is the BLH defining the dipole strength [143, 136]. Practical implementation is achieved by discretizing the source-mode as an array of point dipoles. For each dipole, the contribution to the sound is expressed by the scalar product of the dipole strength by the gradient of the

free-space Green's function for the Helmholtz equation.

The source-mode identity could be thought of as redundancy for free-field calculations. However, it is well suited for understanding the formation of rotating-blade noise wavefronts close to the sources. Moreover, it is very convenient to model the acoustic scattering by surrounding solid surfaces of arbitrary shape. Indeed, scattering is a matter of the relative position of a source to the surfaces and the distance-to-wavelength ratio. The total sound field can be reproduced by a linear superposition of the scattered and direct fields calculated for all stationary dipoles of a source-mode circle, as diffraction problems are usually formulated in the frequency domain for stationary sources. This can be achieved in a semi-analytical way if a tractable expression of the tailored Green's function is available (see the application in section 4.7). Otherwise, the source-mode identity can be combined with a numerical integral formulation of the diffraction problem [86].

4.5 Propeller Noise Scattering

For complete acoustic estimates, it is crucial to consider the diffraction of emitted acoustic waves by the propulsive system or by solid bodies located near a wing, such as landing gears and/or high-lift devices. The complicated geometry of an aircraft makes numerical tools necessary to quantify this effect accurately. However, for simpler assessment at the early design stage, analytical formulations can be preferred as alternatives at the price of crucial geometrical simplifications. In the present work, the retained dominant mechanism is the scattering of propeller noise by the wing trailing edge. For this, in the first step, the wing is mimicked by a zero-thickness rigid half-plane extending to infinity upstream and embedded in a uniform flow. This allows us to use the half-plane Green's function for the convected Helmholtz equation, the problem being solved in the frequency domain. This approach has been thoroughly addressed in the aeroacoustic literature for predicting sound scattering by trailing edges in the presence of a mean fluid motion [173, 174, 143]. Such an approach also requires that the true sound sources are described in terms of stationary sources, which is ensured by the source-mode formalism. Nevertheless, suppose these simplifications are representative of the underlying source and diffraction mechanisms. In that case, they may provide a quick estimate of the radiated sound, reliable enough to compare various installed propeller configurations. In particular, the simplifications must enable us to infer orders of magnitude of the possible amount of reduction brought by a masking strategy, for instance, installing propellers just above a wing, closely upstream of the trailing edge.

Figure 4.4 illustrates the test configuration, involving two side-by-side co/contra-rotating source modes, which mimic a pair of co/contra-rotating propellers, and the half-plane accounting for the rear part of a wing. Results shown hereafter will be displayed on three planes. The first one is the streamwise plane containing the axis of the right source circle, aimed at characterizing the scattering from a lateral point of view. Then, the front plane provides a view towards the upstream direction, introduced to assess the radiation in a plane parallel to the shifted mode circles. Both modes are spinning in the same frontal plane. Finally, the horizontal plane located below the scattering half-plane is considered to assess the noise perceived by an observer on the ground under the flight path of an aircraft, even if the relatively moderate distance is not fully representative yet of the acoustic and geometric far-field. In addition, it provides an insight into the masking effect as a function of the source position relative to the plate.

Use is made of the analytical expression of the half-plane Green's function introduced first by MacDonald [175] in a quiescent medium and readdressed by Jones [176], Rienstra [174], and

Roger *et al.* [143] in two-dimensional and three-dimensional forms with a uniform flow normal to the edge. Ffowcs Williams & Hall also applied this function in their far-field approximation of turbulence scattering into sound in the vicinity of a trailing edge [164]. An important outcome is that some amplification operates on dipoles, with the factor $(kr_0)^{-1/2}$, for sources approaching the edge [143]. This compact scattering regime corresponds to a cardioid radiation pattern. In the present investigation, the sources of propeller noise are distributed on a circle of arbitrary radius and distance to the trailing edge. If the diameter is sufficiently large with respect to the wavelength, some source positions can get very close to the edge, whereas others remain well apart, leading to some imbalance between the scattered source components of a rotor. The exact formulation of Green's function is therefore needed.

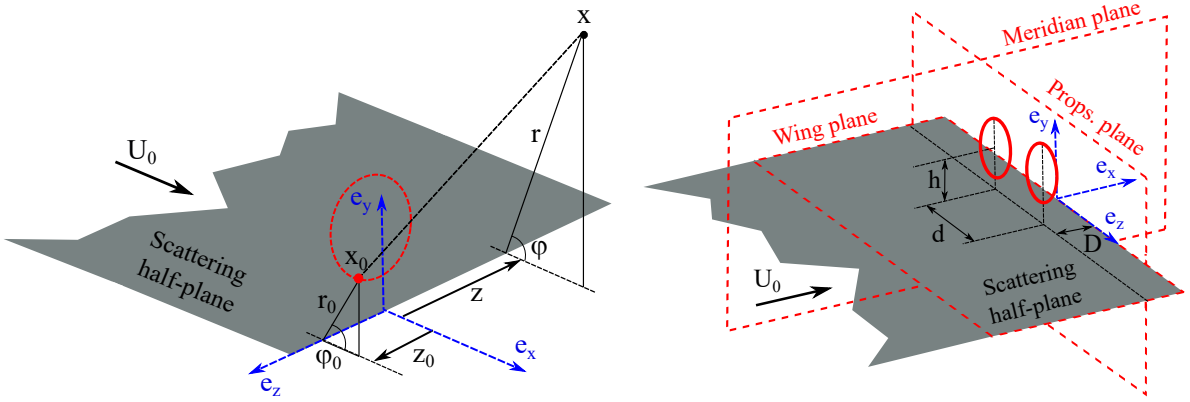

(a) Planes and source modes positions (b) Source and observer locations notation

Figure 4.4: General half-plane reference frames.

The Green's function is valid for arbitrary positions of the sources and the observer but ignores span/chord-end effects. It provides an approximation by reproducing the main physical features for sources close enough to a trailing edge in terms of geometrical parameters and radiating at wavelengths sufficiently lower than the actual chord and span. In the case of rotating-blade noise, this can be achieved by using the source modes introduced in section 4.2. The half-plane Green's function formulation could include an optional correction accounting for a full Kutta condition at the trailing edge. However, previous investigations suggest that, as long as a dipole or a quadrupole is not very close to the edge, the effect of the Kutta correction can be ignored for subsonic flows of Mach numbers up to 0.3 [172].

If expressed in cylindrical coordinates for an observer at point $\mathbf{x_{obs}} = (r_{obs}, \theta_{obs}, z_{obs})$ and a source point $\mathbf{x_0} = (r_0, \theta_0, z_0)$, with the z-axis along the edge and θ_0 being π along the half-plane and zero in its continuation (see Figure 4.4), the three-dimensional form of the half-plane Green's function in a medium at rest reads:

$$\mathrm{G}^{(0)}_{1/2}(\mathbf{x_{obs}}, \mathbf{x_0}) = \frac{-\mathrm{i}k}{4\pi^2} \left\{ \int_{-\infty}^{u0} \frac{K_1^*(\mathrm{i}kR\sqrt{1+u^2})}{\sqrt{1+u^2}} \mathrm{d}u + \int_{-\infty}^{u1} \frac{K_1^*(\mathrm{i}kR'\sqrt{1+u^2})}{\sqrt{1+u^2}} \mathrm{d}u \right\}, \tag{4.3}$$

where K_1^* is the complex conjugate of the modified Bessel function of order 1. $\mathbf{x_0} = (x_0, y_0, z_0)$ and $\mathbf{x_{obs}} = (x_{obs}, y_{obs}, z_{obs})$ are the source and observer vectors respectively and $k = \omega/c_0$. The exact acoustic pressure field of a point dipole is given by the scalar product between its strength $\mathbf{F}$ and the gradient of the Green's function, as $\mathrm{P}^{(0)}_{1/2} = \mathbf{F} \cdot \nabla \mathrm{G}^{(0)}_{1/2}$. Thus Equation 4.3 is the basis for deriving the uniformly valid radiated field of arbitrary source distributions accounting for the diffraction by the edge, at the price of numerical treatment of the integrals and derivatives

concerning the source coordinates. The dependence $e^{-i\omega t}$ of monochromatic waves is implicitly assumed. The distance variables and upper bounds of the integrals are given by the following expressions, where the subscript 0 is the notation referring to the source location:

$$u_0 = \frac{2}{R}\sqrt{r_{obs}r_0}\cos\frac{\theta_{obs}-\theta_0}{2} \quad \text{and} \quad u_1 = -\frac{2}{R'}\sqrt{r_{obs}r_0}\cos\frac{\theta_{obs}+\theta_0}{2}$$

$$\begin{aligned} \text{where} \quad & R^2 = r_{obs}^2 + r_0^2(z_{obs}-z_0) - 2r_{obs}r_0\cos(\theta_{obs}-\theta_0) \\ \text{and} \quad & R'^2 = r_{obs}^2 + r_0^2(z_{obs}-z_0) - 2r_{obs}r_0\cos(\theta_{obs}+\theta_0) \end{aligned}$$

Flow effects associated with forward flight can be included in the scattering model by considering a uniform mean flow of Mach number M_0 as in Equation 4.4, keeping the reference frame attached to the half-plane. The Green's function accounting for the presence of a uniform flow normal to the spanwise direction is obtained from the corresponding Green's function in a quiescent fluid by a Lorentz transform and stretching the space variables and by multiplying by the factor $\frac{1}{\beta}e^{iKM_0(x_{obs}-x0)}$. The rigid half-plane Green's function in the presence of a uniform flow in the positive x_{obs}-direction reads:

$$G_{1/2}^{(M_0)}(\mathbf{x_{obs}}, \mathbf{x_0}) = \frac{1}{\beta}e^{iKM_0(x_{obs}-x_0)}G_{1/2}^{(0)}(\mathbf{X_{obs}}, \mathbf{X_0}), \tag{4.4}$$

$\mathbf{X_{obs}}$ and $\mathbf{X_0}$ are coordinate vectors for which the streamwise coordinate x has been replaced by $X = x/\beta$, the wavenumber being rescaled as $K = k/\beta$ with $\beta^2 = 1 - M_0^2$, β being the Prandtl-Glauert factor. The flow direction is in the positive coordinate x to fit with the scattering by the trailing edge. The angles θ and θ_0 must be redefined as the corrected angles from the wake direction $x > 0$. The stretching of coordinates generates the following transformed variables:

$$\bar{r} = \sqrt{X^2 + y^2}, \qquad X = \bar{r}\cos\bar{\theta}, \quad \text{and} \quad y = \bar{r}\sin\bar{\theta}$$

4.6 Finite-Chord Correction

In the current approach of a simplified geometry, considering the finite chord length C of the wing in the analysis requires replacing the rigid half-plane with an infinite strip of coordinates $(-C \leq x \leq 0,\ -\infty \leq z \leq \infty)$. The scattering of a source-mode by the strip may strongly differ from the ideal trailing-edge scattering deduced from the half-plane Green's function, especially if the chord length is not much larger than the acoustic wavelength λ. Sound is scattered by both the leading edge and the trailing edge, so that more sound is expectedly regenerated in what would be the shadow region, if any, with significant interference between sounds coming from both edges. The interference is also incomplete in the reflection region. Such effects must be accounted for when searching for some optimized configurations, which would require the exact Green's function for a strip of an arbitrary chord. Unfortunately, no uniformly-valid, closed-form expression for this Green's function is available to the knowledge of the author.

High-frequency solutions for the diffraction of an acoustic plane wave by an infinite rigid strip in a fluid at rest, derived with a two-step application of the Wiener-Hopf technique, are

reported, for instance, by Noble [177]. For this, two complementary half-plane problems are solved iteratively, the scattering by the second edge being understood as a correction to the scattering by the first edge. However, the two-step approach is a high-frequency approximation, typically valid for non-compact chords, that is, high values of kC. Higher-order iterations should be determined for moderate values of kC. Moreover, the plane-wave assumption is restrictive. Howe has derived a Green's function for a strip, in the case of low Mach numbers and sources close to an edge [178], using an iterative procedure and a matching with a compact Green's function for low frequencies. These reference solutions only address limited cases. The uniformly valid formalism needed for the present investigation is missing. Therefore, a somewhat empirical correction procedure is proposed and validated in the next subsections as an alternative.

4.6.1 Analytical Approximation

The aim is to reproduce finite chord effects as illustrated in Figure 4.5, with only minor modifications to the approach detailed in the previous section, yielding estimates of the leading edge scattering rather than exact predictions. This will address issues such as selecting suitable candidates for the propeller position and sorting out poor configurations in an optimization strategy.

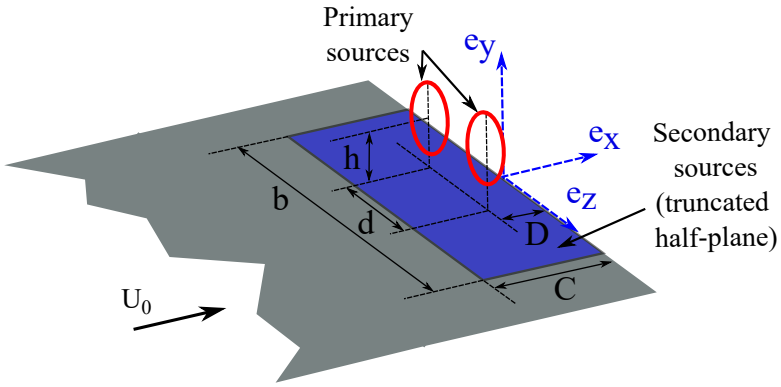

Figure 4.5: Representation of the approximate solution for finite-chord effects.

The idea can be summarized as follows. In the first step, the total sound from the source-mode is calculated with the half-plane Green's function, but for the observer, locations are distributed over the finite-chord strip. For this, the observer point $\mathbf{x}$ is approached to the surface $y = 0$ from any side. The source-mode defines the primary sources, the total sound field of which includes the direct field and the scattered field. The latter is obtained by subtracting the former from the total field. According to Green's formalism, the scattered field is exactly the direct field of secondary dipole sources distributed over the strip. After subtracting the direct field, the strength of these dipoles per unit area equals the acoustic pressure jump between both sides of the strip, which is equivalent to considering twice the scattered sound pressure at the wall $y = 0^+$. Once the secondary sources are known, their radiation is calculated in a second step with the free-field Green's function, but only considering the actual surface corresponding to the rectangular wing, and combined with the direct field of the primary sources, which finally provides a modified total field, an "incomplete half-plane scattering", hopefully, more reliable. Though the final combination of primary and secondary sources is fully relevant, the secondary sources are only approximate since they are deduced from a Green's function tailored to the half-plane but not to the strip. Furthermore, the strip is also truncated spanwise in the present practical implementation, with some span length b. The effect of this truncation is not addressed specifically in the present model. However, a dimensional argument suggests that a finite span would not significantly modify the radiation for $b/\lambda \geq 1$ and for observation angles that are not

too shallow in the spanwise direction. Because of greater importance, the effect of chordwise truncation is assessed below.

4.6.2 Numerical Validation

To assess the accuracy of the proposed analytical approximation, a comparison is made in this section with a numerical simulation, implemented by Siemens Group in the framework of a personal collaboration [179]. The comparison is performed in a two-dimensional case, including a finite-chord segment or a true airfoil shape, and a point dipole source, in the presence of a uniform mean flow. The numerical model solves the convected Helmholtz equation using a p-adaptive finite element method [180]. In this approach, an *a priori* error indicator is used to adjust the order automatically in the elements to maintain a target accuracy, accounting for the local mesh size, frequency, mean flow magnitude, and direction [181]. In this study, all computations were performed using an engineering target accuracy of $E_t = 0.1\%$. The finite element unstructured mesh is generated using Gmsh [182]. An automatic Perfectly Matched Layer is applied on the outer boundaries to efficiently absorb the outgoing waves [183]. The dipole source is implemented as a right-hand side in the convected Helmholtz formulation. Note that a uniform mean flow is considered, in the case of a thin plate, as well as for the true airfoil shape.

4.7 Results and Discussions

The relevance of the analytical approximation is assessed in this subsection by comparisons with the numerical approach of section 4.6. The test, reported in Figure 4.6 is computed with a 2D reduction of the formalism. A point dipole is placed at some short distance of a finite plate of chord lengths $C = \lambda$ (Figure 4.6(a,b)) and $C = \lambda/2$ (Figure 4.6(c,d)). Very similar wavefront patterns are found. The test corresponds to a main lobe of the direct field from the source, impinging on the trailing edge. This condition is known as responsible for the significant regeneration of sound in the geometrical shadow region. In fact, for both frequencies, there is no masking by the plate but rather a wavefront restructuring with multiple directivity lobes. The analytical approximation is found to reproduce these features realistically.

For a more quantitative assessment, results were extracted along horizontal and vertical lines featured by the red dots shown in Figure 4.7 and located just above and at the end of the flat plate, respectively. Figure 4.8 and Figure 4.9 display the phase agreement in the compared sound-pressure profiles. Additionally, some discrepancies can be observed in the amplitude, probably due to the lost information in the truncation process of the Green's function. However, the differences remain very acceptable when it comes to noise estimates in terms of decibels. This confirms the validity of the truncation procedure introduced in section 4.6.

Figure 4.10 shows further computed sound-pressure maps of a dipole source in the presence of a NACA-0012 airfoil. In this case, the simulated wave-front patterns are similar to those with the flat-plate, in Figure 4.6(a,c). Despite the significant thickness at the rounded leading edge, the precise airfoil shape has a weak effect on the sound radiation. This is attributed to the fact that, for the considered source position, the key scattering features are imposed by the trailing edge, which is "sharp" in both cases, therefore with the same degree of singularity. Different conclusions could be drawn for sources close to the leading edge; this aspect has not been considered in the present work. By the way, the result suggests that, at least for sources in the rear part of an airfoil or wing and for the investigated values of the chord-to-wavelength ratio,

the main sound features are a matter of this ratio and source positioning. Therefore, the true shape of the airfoil can be ignored for a first insight into the scattering mechanism. Finally, the analytical model appears as a good candidate for fast and repeated calculations within the scope of parametric studies or optimization algorithms. It will be used with confidence for subsequent three-dimensional inspection of the wing-propellers configuration.

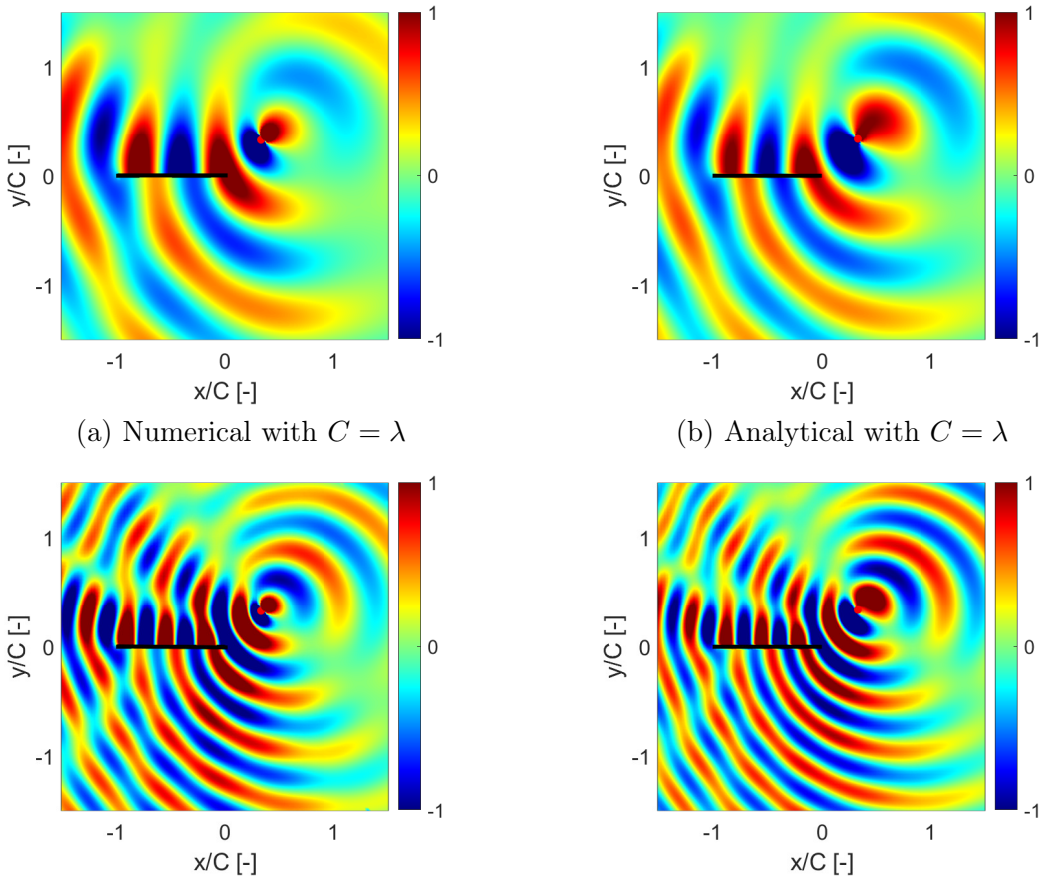

(a) Numerical with $C = \lambda$

(b) Analytical with $C = \lambda$

(c) Numerical with $C = \lambda/2$

(d) Analytical with $C = \lambda/2$

Figure 4.6: 2D instantaneous sound-pressure maps of a dipole in the presence of a finite-chord plate. The dipole is featured by the red dot and the plate is shown in black.

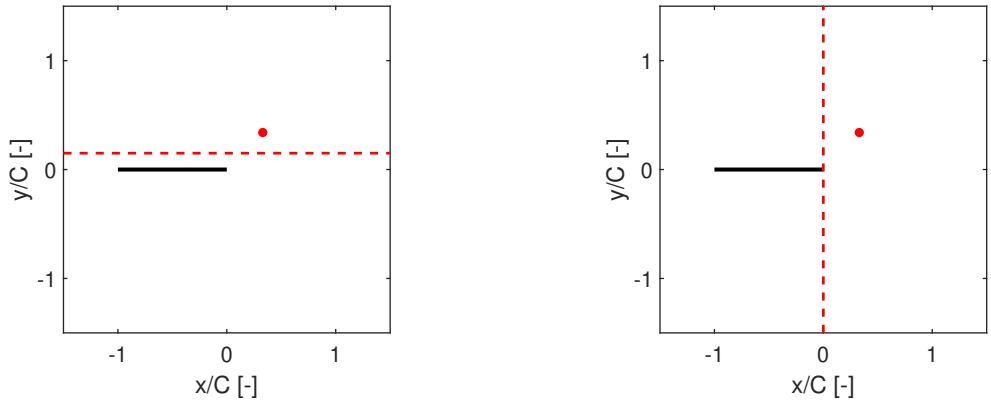

(a) Horizontal line

(b) Vertical line

Figure 4.7: Selected lines for comparisons between analytical and numerical approaches.

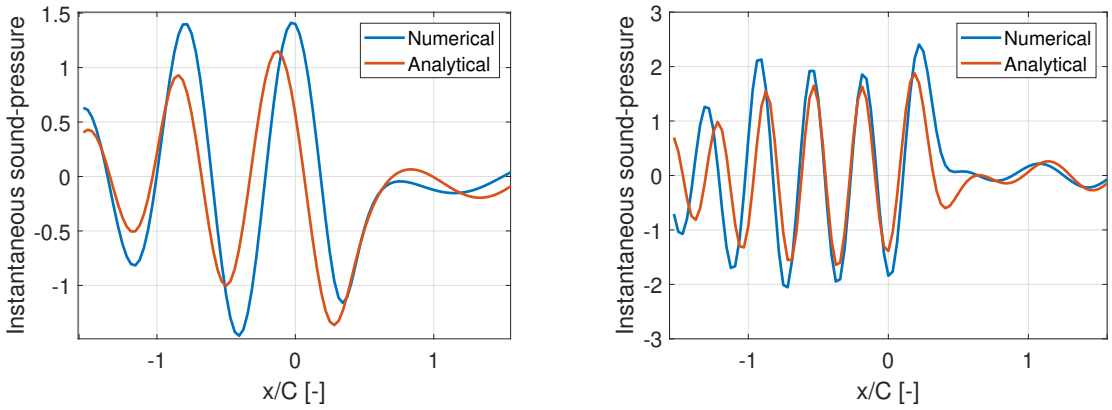

(a) $C = \lambda$ (b) $C = \lambda/2$

Figure 4.8: Compared horizontal-line extractions from numerical and analytical instantaneous sound-pressure maps of a dipole in the presence of a finite-chord plate (Figure 4.6).

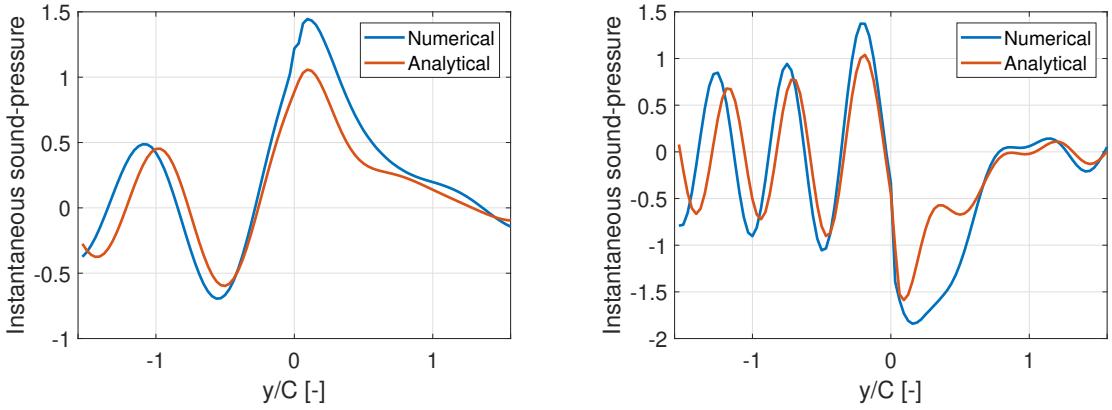

(a) $C = \lambda$ (b) $C = \lambda/2$

Figure 4.9: Compared vertical-line extractions from numerical and analytical instantaneous sound-pressure maps of a dipole in the presence of a finite-chord plate (Figure 4.6).

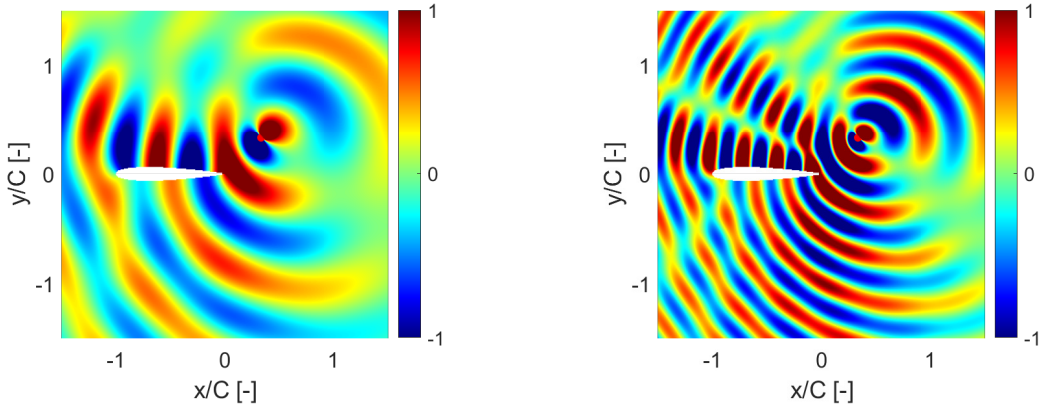

(a) $C = \lambda$ (b) $C = \lambda/2$

Figure 4.10: 2D numerical instantaneous sound-pressure maps of a dipole in the presence of the NACA-0012 airfoil. The dipole is featured by the red dot and the airfoil is shown in white.

After explaining the theory of propeller noise modeling and having validated the sound-scattering model in 2D, chapter 5 will discuss the implementation of the model in the same DEP configurations previously tested. First, it is necessary to calculate by analytical means steady and unsteady-loading noise and then use them as input to compute the total noise produced by changing the parameters listed in Table 3.2.

5 Analytical Approach II: Predictions of Steady and Unsteady Loading Noise

Summary

Once the theory behind the analytical propeller noise model is known, new approximations are provided in this chapter as an easy way of comparing the orders of magnitude of steady-loading and unsteady-loading noise in section 5.1 and section 5.2, respectively. Unsteady blade-loading harmonics are calculated with two different methods by taking numerical inputs obtained from an ENODISE project partner. Finally, the results are discussed in section 5.3.

Contents

5.1 Blade Element Momentum Theory

For subsonic installed rotors, steady-loading noise is most often of secondary importance compared to unsteady-loading noise because of the higher radiation efficiency of blade-loading harmonics induced by the azimuthal mean-flow distortions. Indeed, the associated rotor-locked modes, simulated by source-modes with orders equal to multiples of the blade number, produce an evanescent sound field. However, this general free-field status obviously holds in the presence of a sufficient amount of distortion and becomes questionable for small blade numbers. Moreover, the scattering by obstacles in close vicinity of the source circle, particularly by the trailing edge of a wing, can convert evanescent modes into effectively radiating patterns, leading to reconsidering the ranking. Therefore, the analysis must consider steady-loading noise and unsteady-loading noise as two competing mechanisms. For both, the same approach consists of splitting a blade into annular strips, assuming homogeneous flow conditions along with a strip's spanwise extent, for mathematical tractability. For steady-loading noise, shortly discussed in this section, this reduces to a simple implementation of the BEMT.

The BEMT is a model used to evaluate the performance of a propeller based on its mechanical and geometric parameters and the characteristics of the interacting flow. This model results from the combination of the Blade Element Theory and the Momentum Theory [184, 185]. The BEMT model consists of a system that links three variables a, a', and ϕ_a associated with a fluid annulus. The two former are usually called axial and angular speed-induction factors, respectively. The latter is the relative angle deviation of a fluid annulus. They are defined by:

$$a = \frac{U_\infty - U_0}{U_\infty} \ , \quad a' = \frac{\omega}{2\Omega} \quad \text{and} \quad \tan(\phi_a) = \frac{1-a}{\lambda_r(1+a')}$$

where U_∞ and U_0 are the velocities far downstream and in the vicinity of the rotor, respectively. ω is the induced swirl of the considered annulus and Ω is the angular speed of the rotor. The model also considers the local speed ratio $\lambda_r = \Omega(r)/U_\infty$.

The relative fluid speed perceived from this blade element while rotating is defined as follows:

$$U_{rel} = \frac{U_0}{\sin\phi_a}$$

From momentum theory, the thrust T can be obtained using the following relation when assuming that the blades could produce power without rotation. ρ is the density of the fluid.

$$\mathrm{d}T = 4a(1-a)\rho U_\infty^2 \pi r \mathrm{d}r \tag{5.1}$$

However, when rotation is introduced in the model, the torque Q can be obtained as follows.

$$\mathrm{d}Q = 4a'(1-a)\rho U_\infty \Omega \pi r^3 \mathrm{d}r \tag{5.2}$$

In the blade element theory, the elements are considered to have an infinitesimal extent. Therefore, the annular strips are aerodynamically independent and do not interfere. With those assumptions, the elementary thrust and torque components can be written as:

$$\mathrm{d}T = \frac{1}{2}\rho B c U_\infty^2 \mathrm{d}r \left[C_L \cos\phi_a - C_D \sin\phi_a\right] \tag{5.3}$$

$$\mathrm{d}Q = \frac{1}{2}\rho B c U_\infty^2 r \mathrm{d}r \left[C_L \sin\phi_a + C_D \cos\phi_a\right] \tag{5.4}$$

where B is the number of blades, c is the airfoil chord, and C_L and C_D are the lift and drag coefficients, respectively. For a given blade profile, the lift and drag coefficients are defined as follows, where L_b and D_b are the elementary lift and drag forces applying to a blade element of thickness $\mathrm{d}r$ as seen in Figure 5.1. The parameter α is called the angle of attack and is defined as the angle between the chord and the flow direction, as in the following relation: $\alpha = \phi_a - \gamma$.

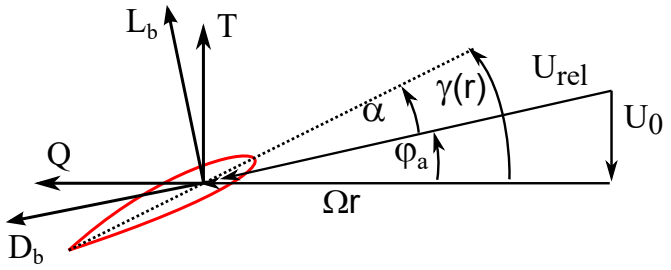

Figure 5.1: Blade element profile and associated angles, velocities, and forces.

$$L_b = C_L(\alpha)\frac{1}{2}\rho U_{rel}^2 c dr \quad \text{and} \quad D_b = C_D(\alpha)\frac{1}{2}\rho U_{rel}^2 c dr$$

The main principle of the BEMT is to combine the equations from momentum theory and blade element theory to obtain the following relations by combining Equation 5.1 with Equation 5.3 and Equation 5.2 with Equation 5.4.

$$\frac{a}{(1-a)} = \frac{\sigma_r}{4}\frac{[C_L \cos\phi_a + C_D \sin\phi]}{\sin^2\phi_a} \tag{5.5}$$

$$\frac{a'}{(1+a')} = \frac{\sigma_r}{4}\frac{[C_L \sin\phi_a - C_D \cos\phi_a]}{\sin\phi_a \cos\phi_a} \tag{5.6}$$

where σ_r is known as the local solidity ratio which can be written as:

$$\sigma_r = \frac{Bc}{2\pi r}$$

Once a blade is split into a series of segments, the BEMT is applied for each segment, at a specified rotational speed and advance ratio $J = \pi U_0/(\Omega r)$, where U_0 is assumed parallel to the axis. The induced speed v_i on the segment numbered j is defined by:

$$\frac{v_i}{\Omega r_j} = \frac{1}{2}\left[-\frac{U_0}{\Omega r_j} + \sqrt{\left(\frac{U_0}{\Omega r_j}\right)^2 + \frac{B c_j}{2\pi r_j}\left(C_L \cos\phi_a - C_D \sin\phi_a\right)}\right] \tag{5.7}$$

The local angle of attack α_j is defined as

$$\alpha_j = \gamma_j - \tan^{-1}\left(\frac{U_0 + v_i}{\Omega r_j}\right) \tag{5.8}$$

where r_j is the mid-span radius of the segment. The coupled Equation 5.7 and Equation 5.8 are solved iteratively, starting from a zero-induced speed. Convergence to the values (α_j, v_i) is reached after a couple of iterations. The lift $(C_L(\alpha_j))$ and drag $(C_D(\alpha_j))$ coefficients are computed with the XFOIL software, using the actual blade cross-section shapes and operational conditions. The converged values of the coefficients determine the forces needed for sound predictions. Tests made on a configuration reported by Romani [77], not shown here, were found

in good overall agreement with both measured data and numerical simulations performed with a Lattice Boltzmann Method (LBM) based software. This confirms that relevant steady-loading noise predictions can be obtained with the BEMT for the sake of further indicative comparison with unsteady-loading noise calculations.

5.2 Unsteady Loading

Steady-loading noise produces the main contribution associated with the global performances, namely the thrust and torque. But as soon as significant flow disturbances or distortions are encountered, for instance, when propellers are close to a cylinder [186] or a pylon [187], unsteady-loading noise takes over, except maybe at high Mach numbers and at the lowest frequencies. Therefore installation effects and associated distortions are the main concern to deal with and the aforementioned steady-state contributions are of secondary importance.

5.2.1 Numerical Simulations

Accompanying numerical simulations were performed by Siemens Group, a partner of the ENODISE project, for the case of a single propeller mounted on its pylon, the wing being removed. The numerical strategy adopted by Siemens for tonal and broadband noise predictions consists of a two-step approach. In the first step, a three-dimensional incompressible Large-Eddy Simulation (LES) of the pylon-mounted propeller configuration is carried out, to compute both the time-averaged velocity field around the propeller, as well as the instantaneous unsteady pressure field on the blades. This allows to extract distorted velocity distributions in upstream and downstream planes. In a second step, a Finite-Element (FE) simulation is performed to compute the noise field accounting for installation effects. From the results obtained in the first step, the unsteady loading noise, which will produce sound in additional modes, different from the steady-loading noise mode, is calculated independently, using the present analytical approach.

Numerical details are beyond the scope of this thesis. A minimum is given in this paragraph, from Le Bras *et al.* [188]. The LES of the configuration is carried out using the implicit unsteady flow solver available in CFD (Computational Fluid Dynamics) software Simcenter STAR-CCM+ [189]. The CFD domain is made of a cylindrical rotating region surrounding the propeller and of a static region in the rest of it. The LES is performed using the WALE subgrid-scale model [190]. The temporal scheme is of second order with eight inner iterations per time step (under-relaxation factors of 0.8 and 0.6 are set for the velocity and pressure, respectively). For the spatial discretization of the convective fluxes, a hybrid MUSCL third-order/central-differencing discretization scheme is chosen. The amount of numerical dissipation of the scheme is prescribed by an upwind blending factor varying between 0 and 1. This factor is set to 0.1 to maximize accuracy. The least-square gradient reconstruction approach is used with the Venkatakrishnan limiter method. Two polyhedral meshes have been considered for the CFD simulations: a coarse grid of 28 M cells and a finer grid of 67 M cells. The main characteristics of the meshes are reported in Table 5.1. The meshes are designed to ensure that the normalized wall-normal distance verifies $y^+ \leq 5$ at the propeller blades.

Table 5.1: Main parameters of the CFD meshes.

Parameter	Coarse grid	Finer grid
Total number of cells	28 M	67 M
Number of cells in rotating area	8 M	16 M
Number of blade prism layers	10	12
Blade prism layer thickness	5×10^{-4} m	7×10^{-4} m
Blades mesh surface size	5×10^{-4} m	5×10^{-4} m
Pylon mesh surface size	2×10^{-3} m	2×10^{-3} m
Mesh size in rotating region	1×10^{-3} m	5×10^{-4} m

After the flow initialization corresponding to a few rotations, unsteady pressure data are recorded on the propeller blades for a period of about 10 rotations for the coarse grid and a period of about 7.5 rotations for the finer grid. The time step for data acquisition is $60/RPM/720$ or $1.1905e-05$ s. In Figure 5.2, an overview of the computational domain is shown alongside an instantaneous view of the Q-criterion iso-surface colored by the velocity magnitude from the LES with the finer grid is provided.

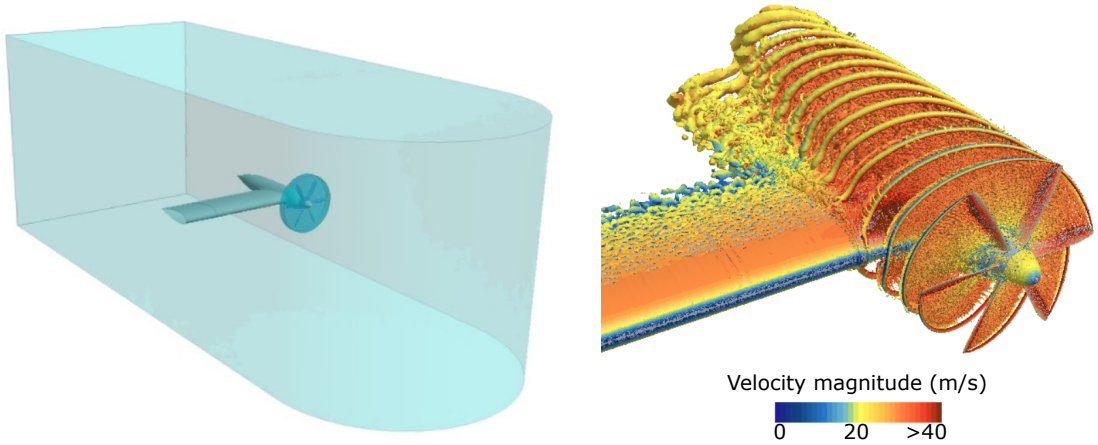

(a) LES computational domain (b) Q-criterion

Figure 5.2: Representation of the CFD domain and instantaneous snapshot of Q-criterion iso-surfaces colored by velocity magnitude in LES with finer grid. Siemens computations.

From the CFD simulations, the time-averaged velocity components in the axial and tangential directions are computed from two 0.125 m radius disks located at about 0.015 m from the rotor center in the axial direction upstream and downstream of the propeller center, respectively, as seen in Figure 5.3(a). The information is taken at these two planes instead of the plane of rotation because the rotating mesh generated in this zone does not allow easily extracting the time-averaged velocity components. However, both disks are close enough to the propeller and the obtained data is reliable. Figure 5.4 and Figure 5.5 show the velocity results over both disks, from which the profiles plotted in Figure 5.6 and Figure 5.7 are obtained for the five radii of the discretization. For the sake of defining input data in the analytical model, averaged profiles are calculated by combining the upstream and downstream ones. This is believed to provide a relevant estimate of the velocity fluctuations perceived by the propellers. Splitting the blades into five segments as illustrated in the figure is enough, each segment being acoustically compact at the frequencies of interest.

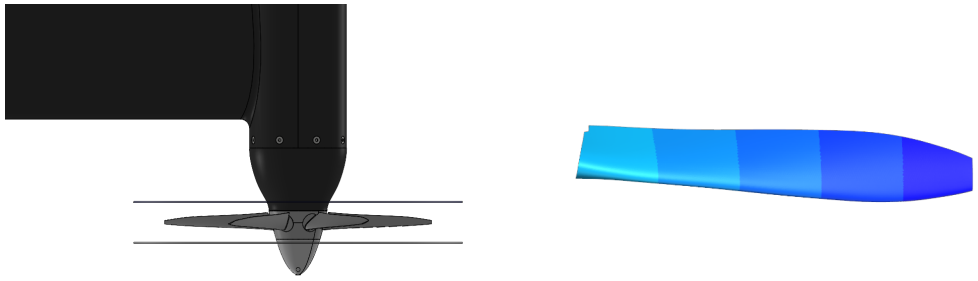

(a) Upstream and downstream planes (b) Segment size $\approx 0.017\ m$

Figure 5.3: Velocity components extraction planes (a) and 5-blade segmentation case (b).

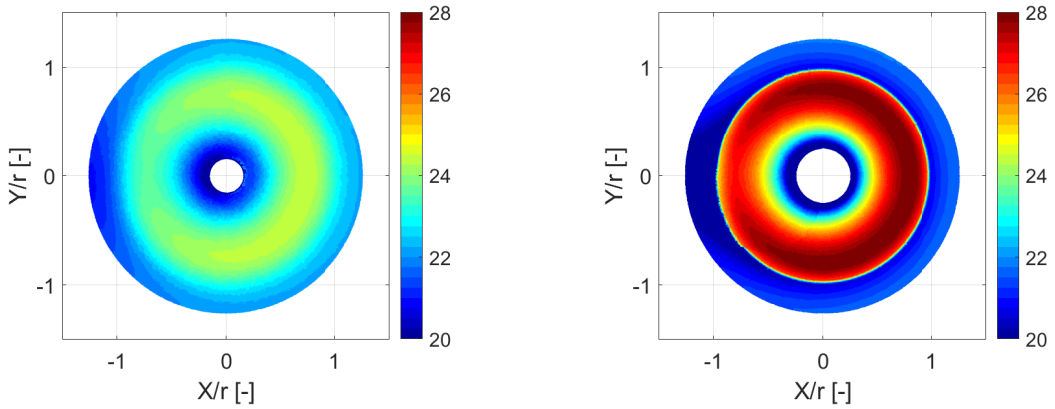

(a) Upstream (b) Downstream

Figure 5.4: Axial velocity on fixed planes upstream and downstream the propeller.

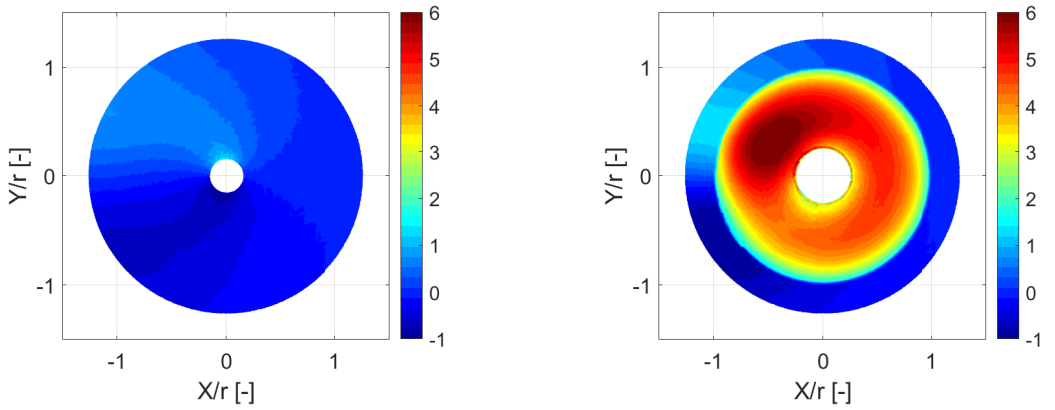

(a) Upstream (b) Downstream

Figure 5.5: Tangential velocity on fixed planes upstream and downstream the propeller.

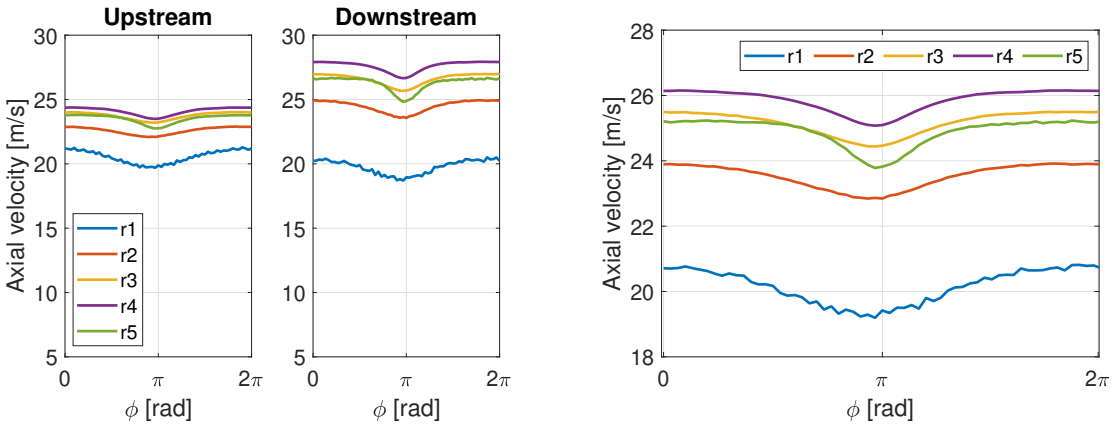

(a) Upstream and downstream profiles (b) Mean profiles

Figure 5.6: Axial velocity profiles along the blade span.

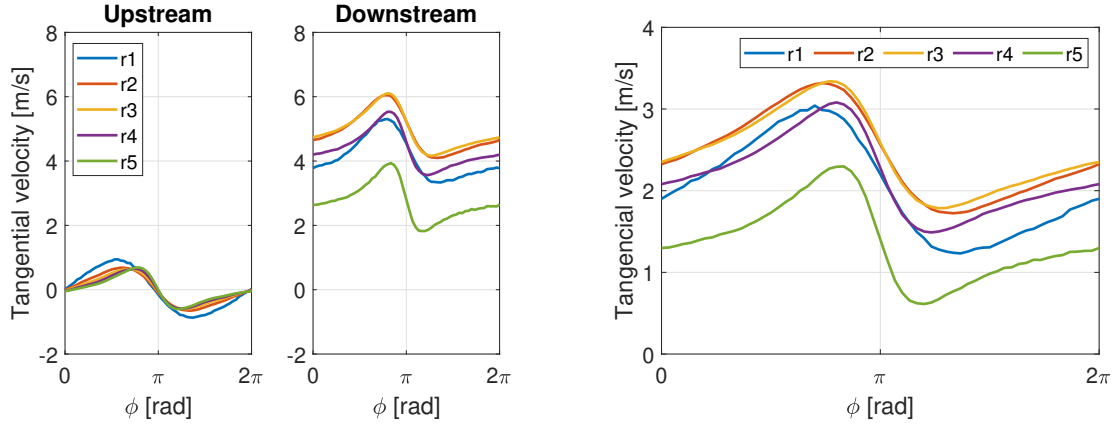

(a) Upstream and downstream profiles (b) Mean profiles

Figure 5.7: Tangential velocity profiles along the blade span.

As the mean axial and tangential velocities, defined in Figure 5.6(b) and Figure 5.7(b) are periodic in the angular coordinate (ϕ), they can be expressed in the form of Fourier series as follows:

$$V_{\mathrm{i}}(\phi) = \sum_{s=-\infty}^{\infty} V_s(\mathrm{i})\, \mathrm{e}^{\mathrm{i}s\phi} \quad \text{with} \quad V_s(\mathrm{i}) = \frac{1}{2\pi} \int_0^{2\pi} V_{\mathrm{i}}(\phi)\, \mathrm{e}^{-\mathrm{i}s\phi}\, \mathrm{d}\phi$$

Given the chordwise compactness of the blades (chord length smaller than the acoustic wavelengths) and of the moderate Mach numbers (about 0.2), the sectional BLH can be approximately inferred from Sears' theory, leading to the following expression, where S stands for the classical Sears' function [191, 192], c_j for the chord length of the blades at the radius r_j, Δr for the spanwise blade segmentation, and w_s the total upwash velocity variation felt by the blades because of the distortion. U_0^p is the chordwise phase speed of the interaction in the blade frame of reference. w_s is related to the axial (w_a) and tangential (w_t) velocity variations.

$$F_s = \pi\, \rho\, c_j\, \Delta r\, U_0^p\, w_s\, \mathrm{S}\left(\frac{s c_j}{2 r_j}\right)$$

$$\text{with} \quad w_s = w_a \cos(\gamma) + w_t \sin(\gamma) \quad \text{and} \quad U_0^p = \cos(\alpha)\sqrt{(\Omega r_j)^2 + (U_0 + U_{ind})^2}$$

with γ the local stagger angle as shown in Figure 4.2.

As an alternative to this BLH calculation, the unsteady forces experienced by the propellers can also be obtained directly from the numerical simulation. In the present study, a 5-blade segmentation is considered, as illustrated in Figure 5.3(b). The forces shown in Figure 5.8 and computed for each segment in the time domain are extracted from Simcenter 3D [193].

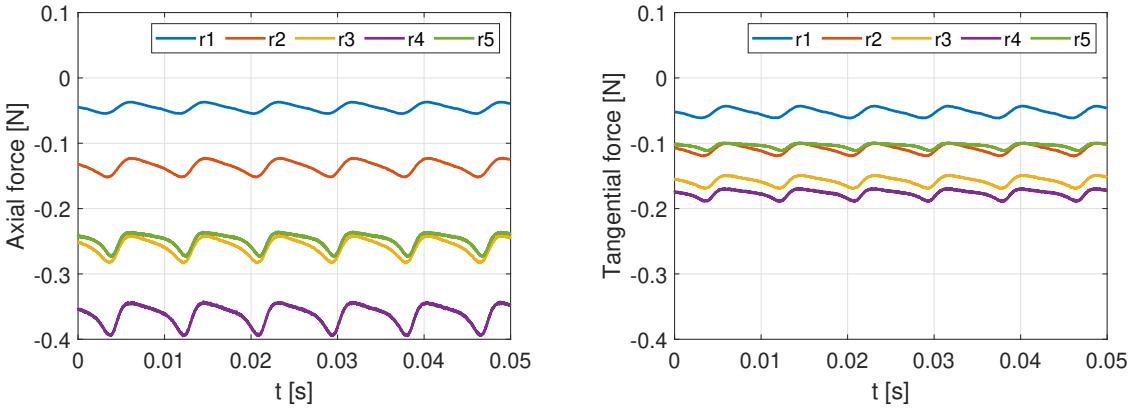

(a) Axial (b) Tangential

Figure 5.8: Force fluctuations for the 5-blade segmentation case.

Estimates of the coefficients F_s of the Fourier series of $F(t)$, not shown for conciseness, have been calculated from the definition:

$$F(t) = \sum_{s=-\infty}^{\infty} F_s \, \mathrm{e}^{-\mathrm{i}s\Omega t} \quad \text{with} \quad F_s = \frac{\Omega}{2\pi} \int_0^{2\pi/\Omega} F(t) \, \mathrm{e}^{\mathrm{i}s\Omega t} \, \mathrm{d}t$$

Regarding the numerical post-processing for calculating the sound, Siemens implements the following approach. Noise predictions are obtained using the FE approach available in Simcenter 3D [193] for unsteady propeller noise. The propeller noise sources are modeled as discrete dipoles. The dipole source strength is obtained by integrating the transient incompressible pressure obtained from CFD over compact blade segments. The number of segments per blade denoted b_s, is defined as a function of the speed of sound c_0 and the maximum frequency of interest f_{max} for the noise predictions. N_s stands for the number of segments per wavelength:

$$b_s = \frac{c_0}{f_{max} N_s}$$

Once computed, the dipolar contributions are then mapped onto the local degrees of freedom of the FE mesh, which are then used as right-hand side terms in the FEM (Finite-Element Method) problem. To account for installation effects, the FE simulations can include scattering surfaces. It can also account for the sound sources originating from these surfaces using Curle's acoustic analogy fed with unsteady pressure data preliminary computed from CFD.

5.3 Results and Discussions

5.3.1 Blade-Loading Harmonics

The first step is to estimate the steady blade forces responsible for steady-loading noise. For this, the simplest implementation of BEMT, neglecting swirl, is computed for different J values ranging from 0.6 to 1.2. Figure 5.9 displays the variations of some parameters along the blade span. The plots indicate that the angle of attack and consequently the lift coefficient are highest between $\approx$ 30% and 70% of the blade span, whereas the induced velocity and the Reynolds number are higher at around 80% of it.

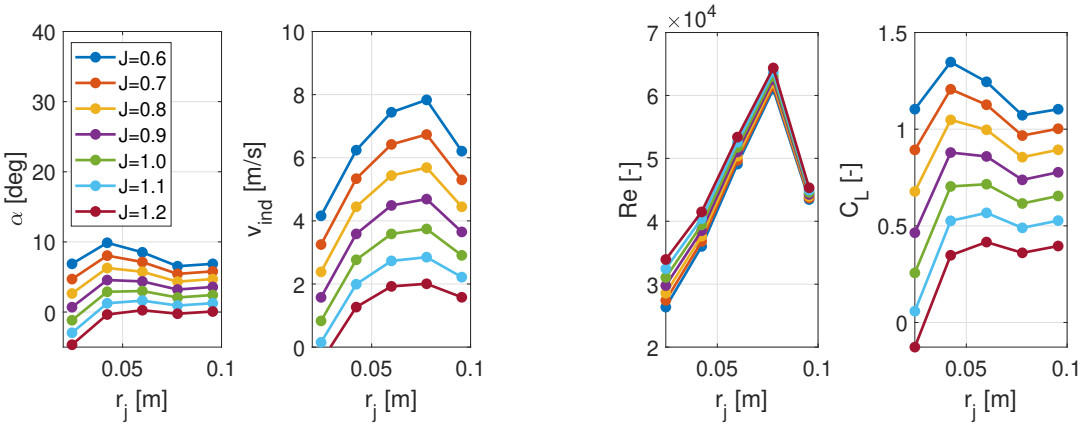

(a) Angle of attack and induced velocity (b) Reynolds number and lift coefficient

Figure 5.9: Variations of main parameters along blade span at different J, according to the BEMT model.

The next step is to estimate the thurst. Figure 5.10 shows the comparison between the analytical approximation of the thrust and the experimental value measured with the load cell in the single-propeller configuration. The prediction overestimates the thrust for all J values. This could be attributed to differences between the modeled airfoil cross-section for computing the BEMT and the real one at each radius of the blade. But the most probable explanation is the fact that tip-effects and swirl are ignored in the simplified BEMT. However, the differences are acceptable for steady-loading noise calculations.

Finally, the steady-state force component F_0 and the BLH F_s coefficients are presented in Figure 5.11 and Figure 5.12, respectively. The mean value F_0 associated with steady-loading noise was found to be typically 10 times higher than the BLH amplitudes $F_{s\pm1}$, whereas higher harmonics up to $F_{s\pm5}$ were much lower. However, as will be shown in the next subsection, those higher harmonics still produce an important noise contribution when compared to steady-loading noise. Higher harmonics from $F_{s\pm6}$ are not plotted as they are negligible.

BLH estimates are made with two different post-processing approaches of the CFD data. The first approach uses the averaged velocity maps in the rotor disc (Figure 5.12(a)) and the second one is a direct computation of the force on each blade segment (Figure 5.12(b)). As can be seen, both predictions present very similar and consistent results, not only regarding the order of magnitude but also the phase and sectional contribution in each BLH, which confirms the reliability of Sears' theory in the present case.

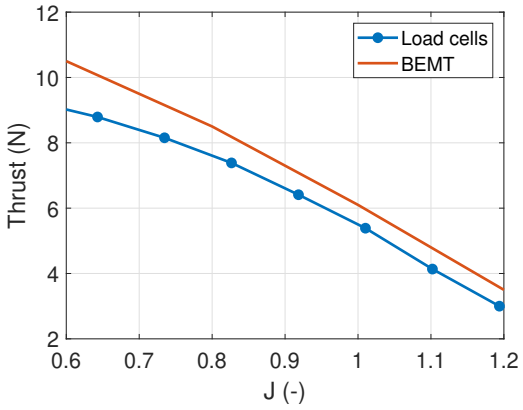

Figure 5.10: Thrust comparison between experimental results and BEMT.

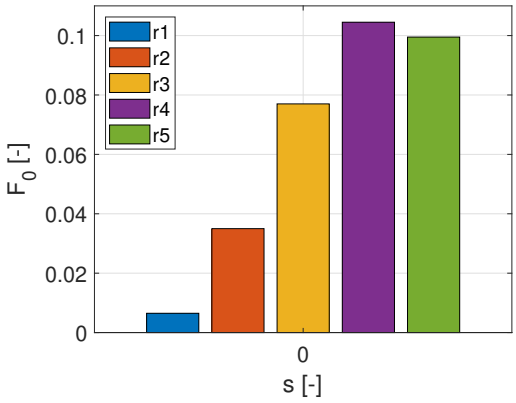

Figure 5.11: Steady-loading.

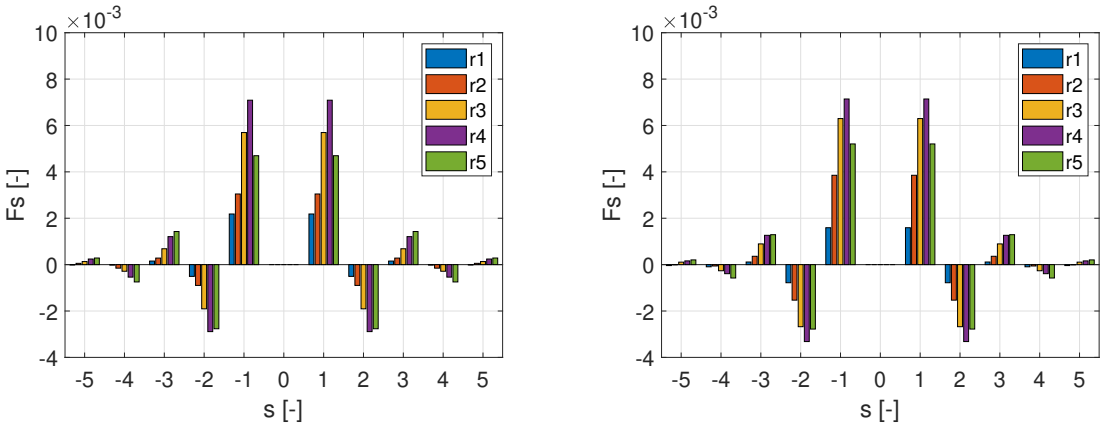

(a) From velocity disks

(b) From unsteady blade forces

Figure 5.12: Unsteady-loading harmonics.

5.3.2 Wing-Propellers Test-Case

Analytical sound predictions in the test cases defined in Figure 3.5 are presented and discussed in the present subsection. They complement a previous study performed with a single propeller

[84]. First, a test case is defined to validate the analytical approximation of the BLH (obtained from unsteady blade forces) by comparisons with the numerical approach previously described in section 5.2. The test is computed with the two propellers placed close to the trailing edge and with $\phi = 0$, assuming that the blade loading harmonics determined in the single-propeller test without the wing are still the same after installation on the wing. Though this is highly questionable, the test makes sense for the validation of the analytical approach; it separates sound-scattering effects from additional aerodynamic distortions due to the vicinity of the wing. As shown in Figure 5.13, very similar wavefront patterns are found by comparing the noise calculated with both methods. In this figure and the following, the propellers are featured in red circles and the wing is shown in black. For installed subsonic propellers, the steady-state aerodynamics of the blades can radiate loud sound and present significant regeneration of sound under the wing, whereas it is relatively ineffective in ideal free-field conditions. Furthermore, the color maps in subplots (a) and (b), and also (c) and (d), exhibit very similar wavefront patterns.

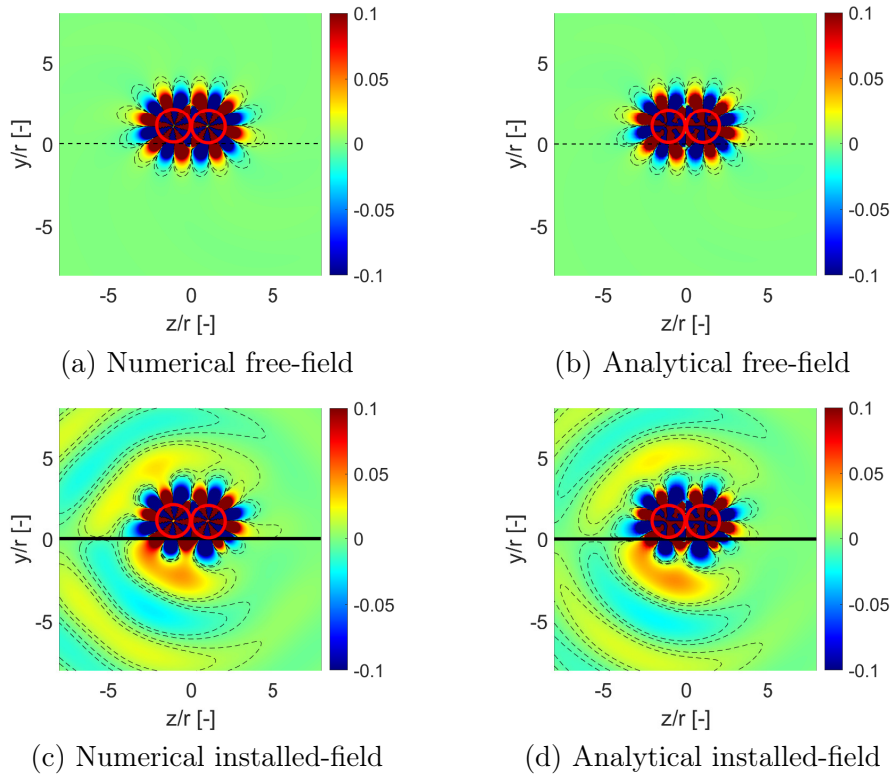

(a) Numerical free-field (b) Analytical free-field

(c) Numerical installed-field (d) Analytical installed-field

Figure 5.13: Instantaneous steady-loading sound-pressure maps in propellers plane for Min-ϕ0 configuration with co-rotating propellers. Iso-contours over ±10% of the range.

Once the analytical approximation is validated, the steady and unsteady-loading noise contributions are compared in the following Figure 5.14 for the loudest configuration with COR propellers (Min-ϕ30). Again, calculations are performed for fixed BLH values, only paying attention to changes in the scattering effect. As can be seen, the difference is larger in the free-field case when compared to the installed field. This effect is attributed to the fact that unsteady-loading noise radiates in several efficient modes, whereas, the rotor-locked mode $n = B = 6$, associated with steady-loading noise at the BPF, is not efficient. This mode only generates an evanescent wave in the free field, because of its low tangential phase Mach number. This is a typical property of low Mach number propellers with significant blade numbers [91]. Therefore, the intrinsic steady-loading contribution is poor. In contrast, for the installed-field case, the steady-loading contribution is higher because the interaction with the wing makes this mode efficient, whereas,

for the unsteady case, all modes are already efficient. Hence, there are no significant differences with the free-field case. Finally, because of the steady-loading noise contribution, the total noise, as expected, is higher for the installed case.

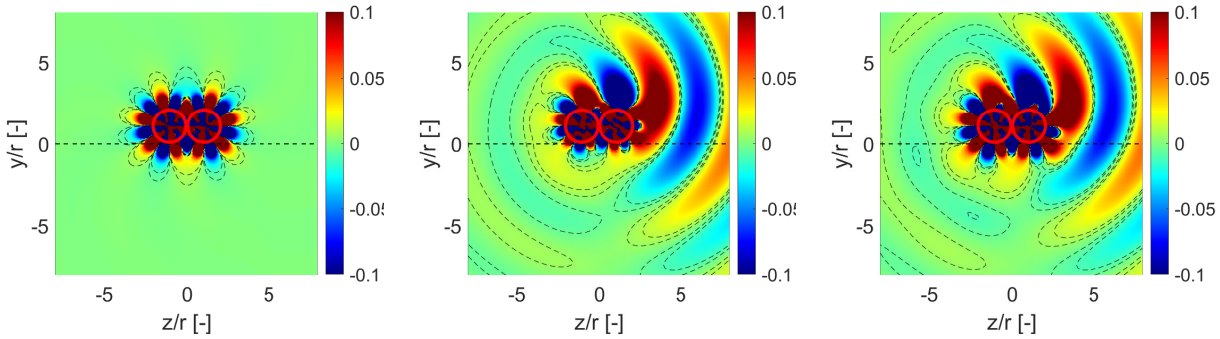

(a) Steady-loading noise (b) Unsteady-loading noise (c) Total noise

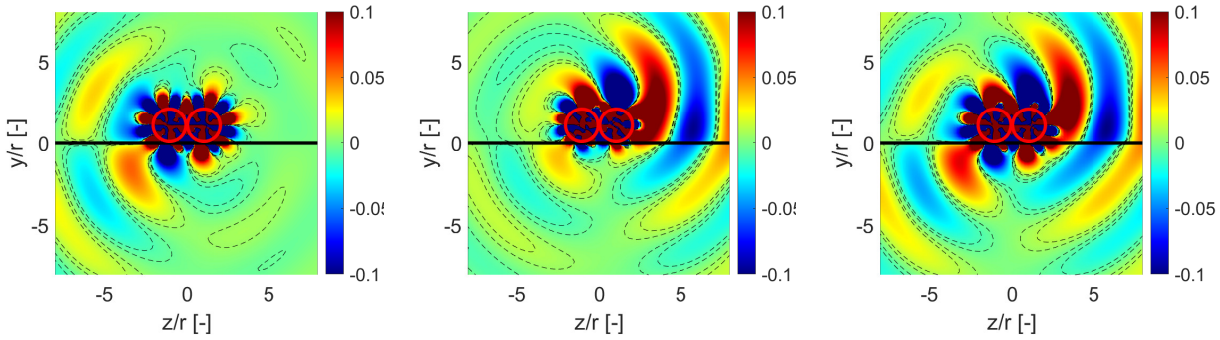

(d) Steady-loading noise (e) Unsteady-loading noise (f) Total noise

Figure 5.14: Instantaneous free-field (a,b,c) and installed-field (d,e,f) sound-pressure maps in propellers plane for Min-ϕ30 configuration with COR propellers. Iso-contours over $\pm 10\%$ of the range.

The noise contribution is not the same for each blade segment. It depends on its associated BLH and radius. Figure 5.15 illustrates the total loading noise differences when computing separately the contribution of each isolated segment, for the Min-ϕ30 case. The plot indicates that, for what is determinant for far-field radiation, the highest contribution corresponds to the tip of the blades, whereas the lowest one is not from the hub but from the second blade segment.

Unsteady loading is also defined as the sum of the noise produced by different modes. The analytical model has the interest of giving easy access to the separated contributions of the modes, as shown in Figure 5.16. The radiation efficiency of each mode is emphasized by the Bessel function acting as a weighting factor on the BLH, according to the far-field formulation. The mean value of the sectional blade force F_0, referred to as the steady loading, must be distinguished from all other BLH resulting from the blades' operation through a steady-state but azimuthally distorted mean flow. As intrinsic to the blade design, F_0 is the only contributor to the thrust, whereas all other coefficients F_s are produced as a result of the distortions and have no direct effect on the aerodynamic performances. In that sense, there is no obvious relationship between aerodynamic efficiency and tonal noise in the general case. As pointed out before, even though the BLH of highest orders have the lowest values, for all radii, they can be the most effective ones. This is seen in Figure 5.16(a,b,c) for the modes $1-3$, whereas the modes 4 and 5 have a lower noise contribution.

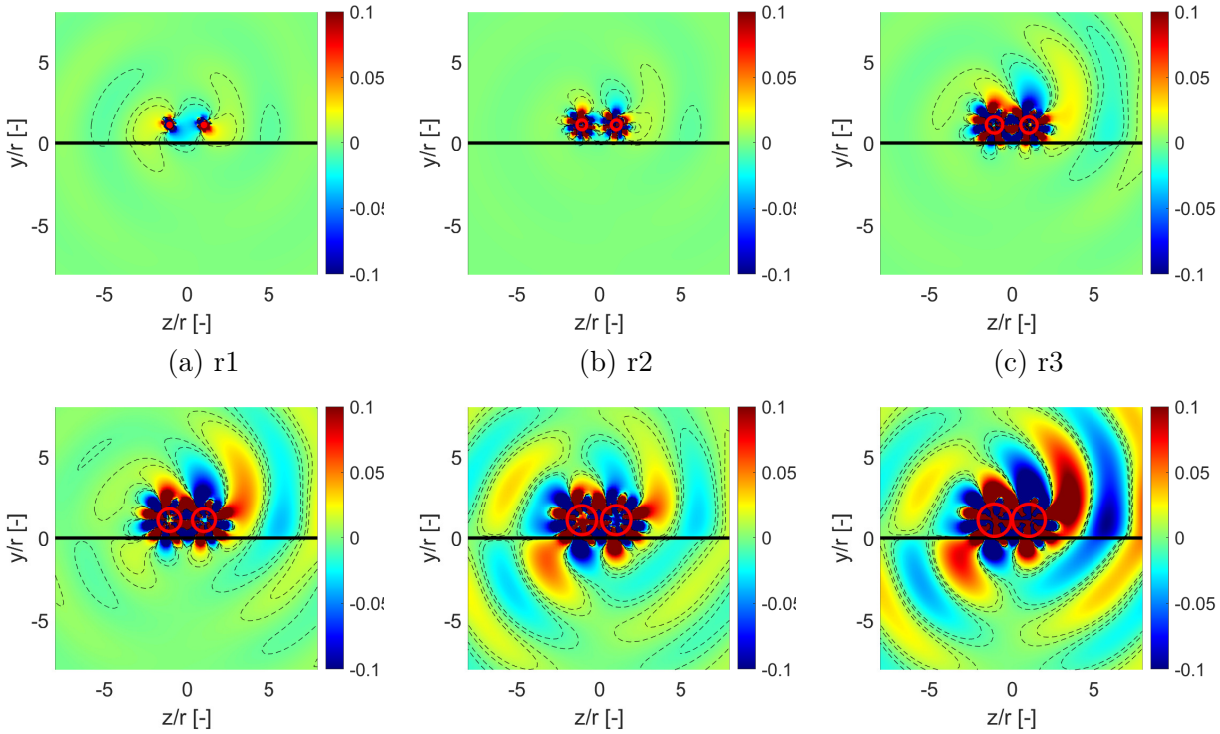

(a) r1 (b) r2 (c) r3

(d) r4 (e) r5 (f) r1 to r5

Figure 5.15: Instantaneous installed-field sound-pressure maps for total loading noise sources at different radii, in the Min-ϕ30 case with COR propellers. Iso-contours over $\pm$10% of the range.

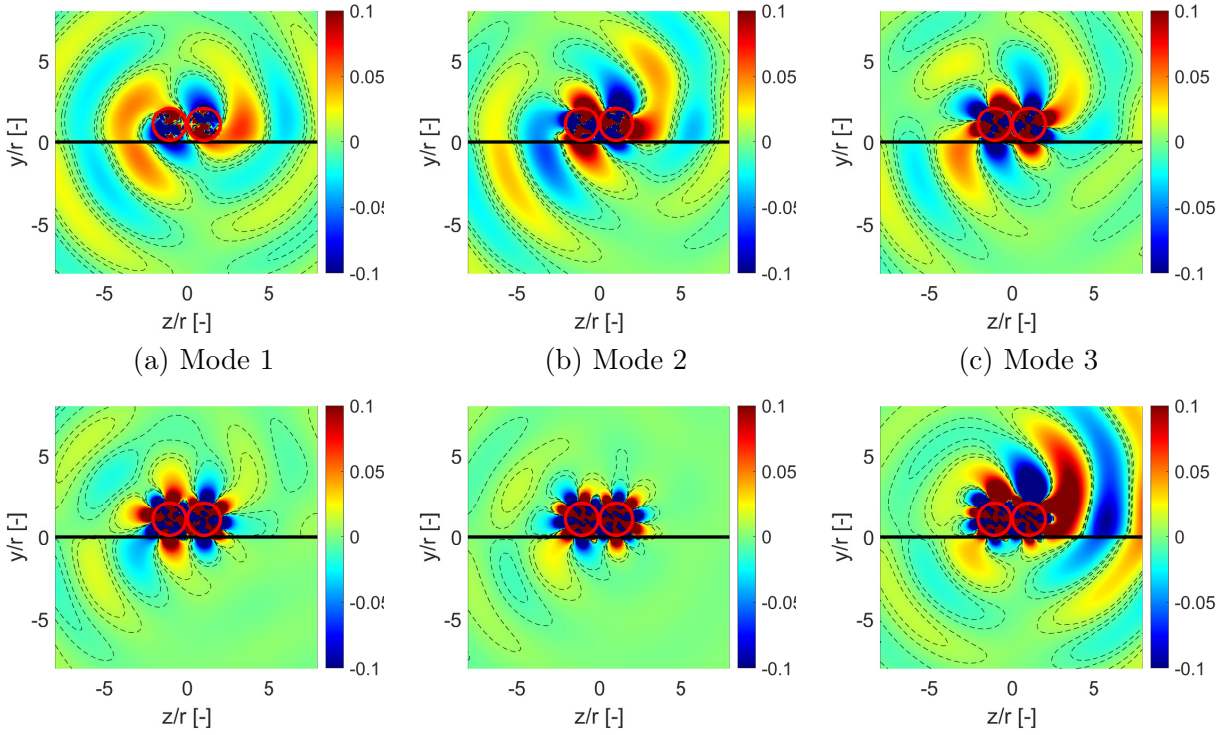

(a) Mode 1 (b) Mode 2 (c) Mode 3

(d) Mode 4 (e) Mode 5 (f) Mode 1 to 5

Figure 5.16: Instantaneous installed-field sound-pressure maps of different modes for Min-ϕ30 case with COR propellers. Iso-contours over $\pm$10% of the range.

Free-field sound-pressure maps of the loudest and quietest cases, Min-ϕ30 and Max-ϕ0 configurations, respectively, are shown in Figure 5.17, for co-rotating propellers. Results are now shown in complementary perpendicular planes, namely the propellers plane $x = X$, the meridian plane $z = 0$, and the wing plane $y = Y$. Important differences are evidenced when comparing both configurations. For the Min-ϕ30 case, sound waves are expanding mainly along the plane of the (removed) wing $z > 0$, corresponding to the upward vertical direction in the experiment, as shown in Figure 5.17(a,b), whereas, for the Max-ϕ0 case, the waves radiate laterally, as displayed in Figure 5.17(d to f).

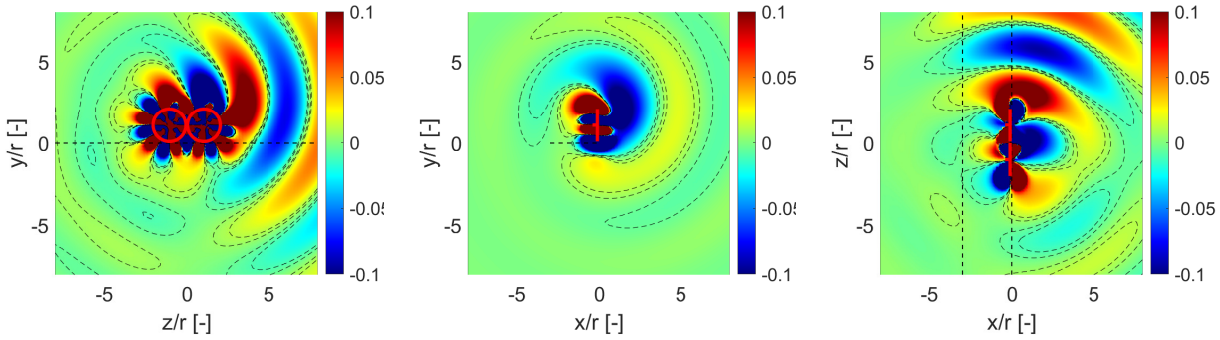

(a) Min-ϕ30 - props. plane (b) Min-ϕ30 - meridian plane (c) Min-ϕ30 - wing plane

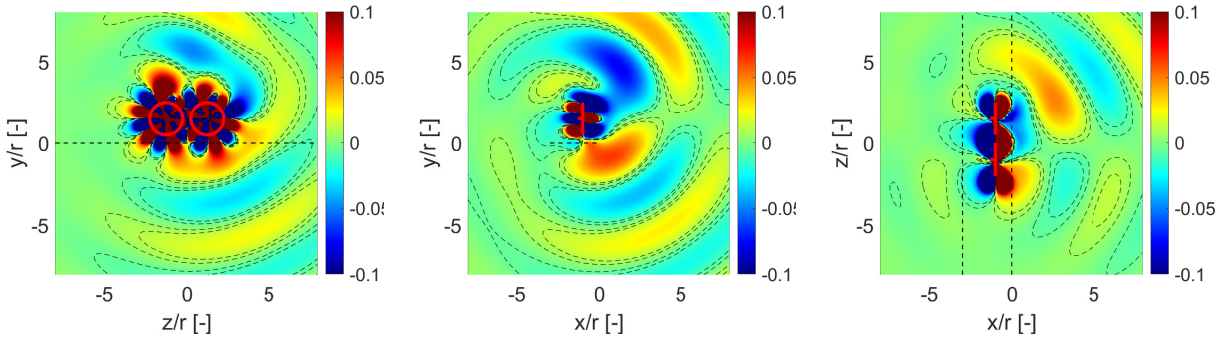

(d) Max-ϕ0 - props. plane (e) Max-ϕ0 - meridian plane (f) Max-ϕ0 - wing plane

Figure 5.17: Instantaneous free-field sound-pressure maps for total loading noise sources and COR propellers. Iso-contours over $\pm$10% of the range.

Figure 5.18 compares the corresponding instantaneous installed-field maps for total loading noise at the BPF for co-rotating propellers. The plotted results are for the same two selected installed configurations and three aforementioned planes, using the same arbitrary color scale. Significant amplification, featured by higher color saturation, is found in all cases with the Min-ϕ30 configuration. The radiation is strongly enhanced by the presence of the wing because of the vicinity of the scattering edge. This is attributed to the dipole nature of the blade forces acting as sound, especially because the blade-tip to trailing-edge distance is smaller than in the Max-ϕ0 configuration and much smaller than the wavelength, leading to a theoretical condition for amplification according to section 4.5. In addition, the sound regeneration effect is seen even though the blades are located above the trailing edge. The apparent silent zone seen below the wing in Figure 5.18(b) corresponds to a cut in the map of Figure 5.18(a) through an extinction area, therefore, the sound regeneration in the shadow region cannot be identified on this subplot. In the Max-ϕ0 cases, there is no sound amplification because of the wing compared to the free-field results, even though there is still a significant noise in the shadow region. On the contrary, there is partial noise-masking below the wing, as expected. Finally, Figure 5.19 illustrates the 3D directivity of the aforementioned configurations, which can be compared with

the ones in Figure 3.42 obtained experimentally. By looking at the maps, it can be seen that the analytical model is able to capture some details noticed in the tests. For the loudest case, the sound is strongly radiated in the upper half of the sphere because of the direction of rotation of the propellers. Additionally, the masking effect is evident in the quietest case, alongside lower radiation over the wing compared to the loudest configuration.

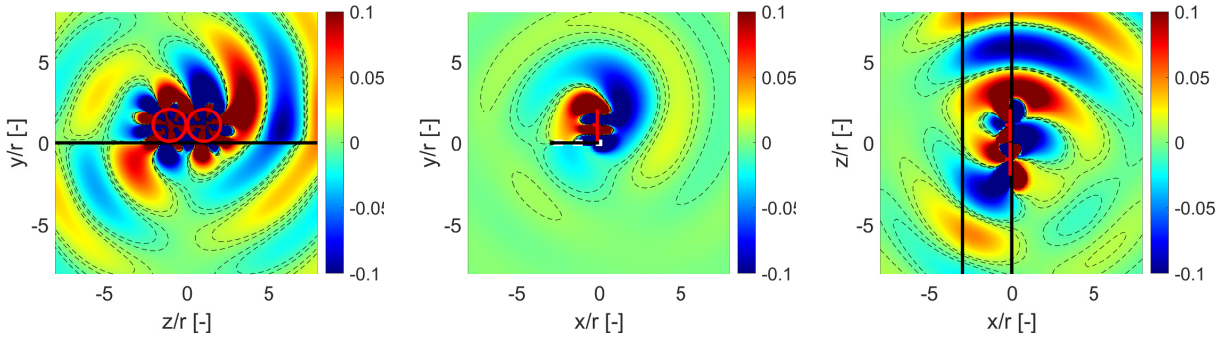

(a) Min-ϕ30 - props. plane (b) Min-ϕ30 - meridian plane (c) Min-ϕ30 - wing plane

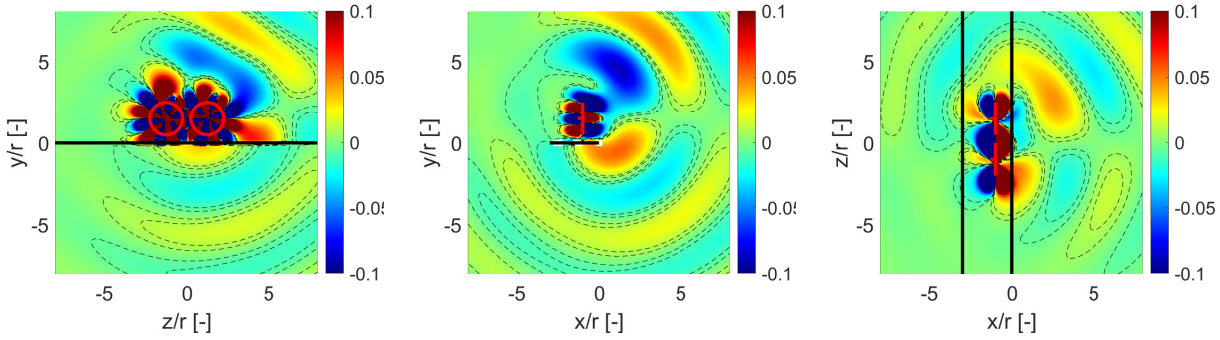

(d) Max-ϕ0 - props. plane (e) Max-ϕ0 - meridian plane (f) Max-ϕ0 - wing plane

Figure 5.18: Instantaneous installed-field sound-pressure maps for total loading noise sources and COR propellers. Iso-contours over ±10% of the range.

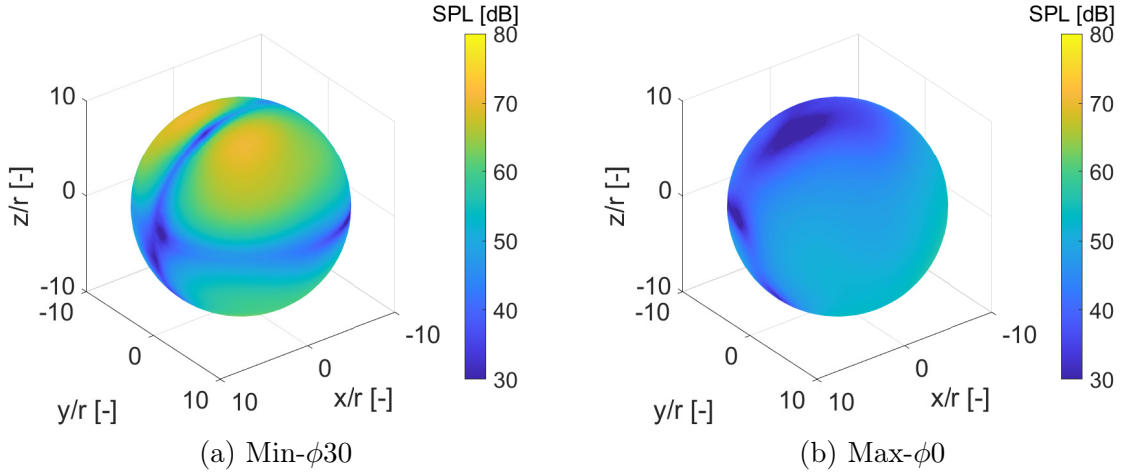

(a) Min-ϕ30 (b) Max-ϕ0

Figure 5.19: 3D directivity patterns of the 1st BPF (700 Hz) for total loading noise sources in loudest (a) and quietest configurations (b) with COR propellers.

Once the COR cases are analyzed, the CTR configuration is also discussed. It is worth noting that the minimum-noise and maximum-noise conditions are more essentially determined by edge-scattering effects, either in the sense of masking or in the sense of regeneration/amplification.

Therefore, the minimum-noise configuration for COR can be used with CTR, with no need to repeat the complete test matrix. The results in Figure 5.20 show that the Max-ϕ0 case presents higher noise radiation in all planes when compared with the COR architecture in Figure 5.18(d,e,f). The same is obtained with the Min-ϕ30 (see Figure 5.20(a,b,c)), however, this is a special case that produced an extinction plane in the meridian plane because of different phase angles in both propellers which cancel the sound of each other. Except for the meridian plane in the counter-rotating case, which coincides with the extinction one, the Min-ϕ30 is again louder for the CTR case. The tonal 3D directivity of the CTR cases is also shown in Figure 5.21. The maps confirm that, for both configurations, the sound increases with CTR propellers, as explained before. This is in agreement with the results obtained in chapter 3. Additionally, to better compare both propeller rotations, Figure 5.22 and Figure 5.23 display the SPL maps in the three observation planes for both configurations. On the one hand, the COR case radiates the noise towards the z-axis in both the propeller plane and the wing plane, whereas in the CTR configuration, high-level sound is radiated, symmetrically with respect to the z-axis. The symmetry is expected from the zero phasing between blades, combined with contra-rotation, because the interaction between the blades and the distortion around the pylons is occurring simultaneously and symmetrically on both propellers. On the other hand, as emphasized in all planes, the CTR configuration radiates louder sound above and below the wing. Therefore, the Max-ϕ0 case might no longer be the quietest case with CTR propellers, as decibel levels are higher for all the planes. This suggests that this is not the best option for selecting propellers' rotation sense.

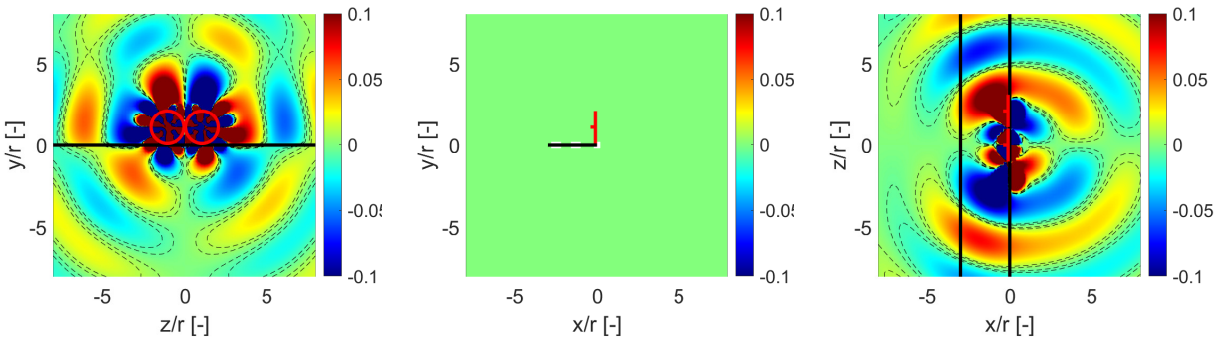

(a) Min-ϕ30 - props. plane (b) Min-ϕ30 - meridian plane (c) Min-ϕ30 - wing plane

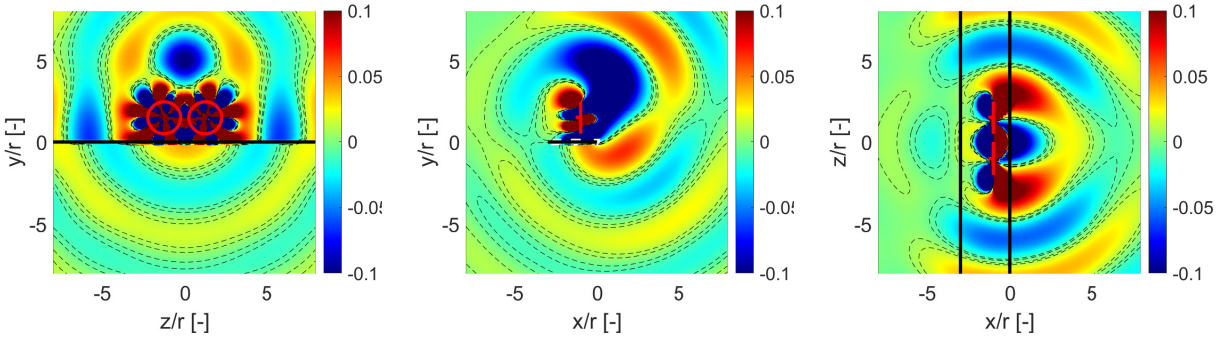

(a) Max-ϕ0 - props. plane (b) Max-ϕ0 - meridian plane (c) Max-ϕ0 - wing plane

Figure 5.20: Instantaneous installed-field sound-pressure maps for total loading noise sources with CTR propellers. Iso-contours over ±10% of the range.

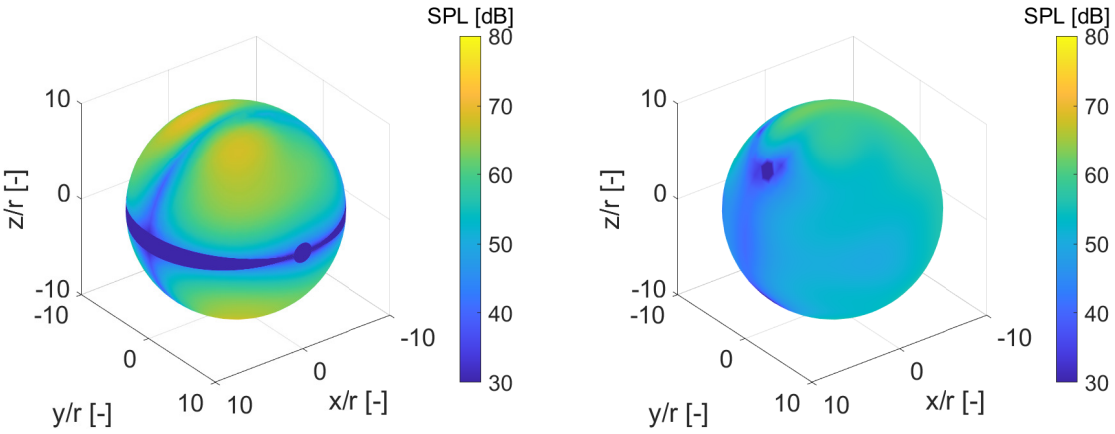

(a) Min-ϕ30 (b) Max-ϕ0

Figure 5.21: 3D directivity patterns of the 1st BPF (700 Hz) for total loading noise sources in loudest (a) and quietest configurations (b) with CTR propellers.

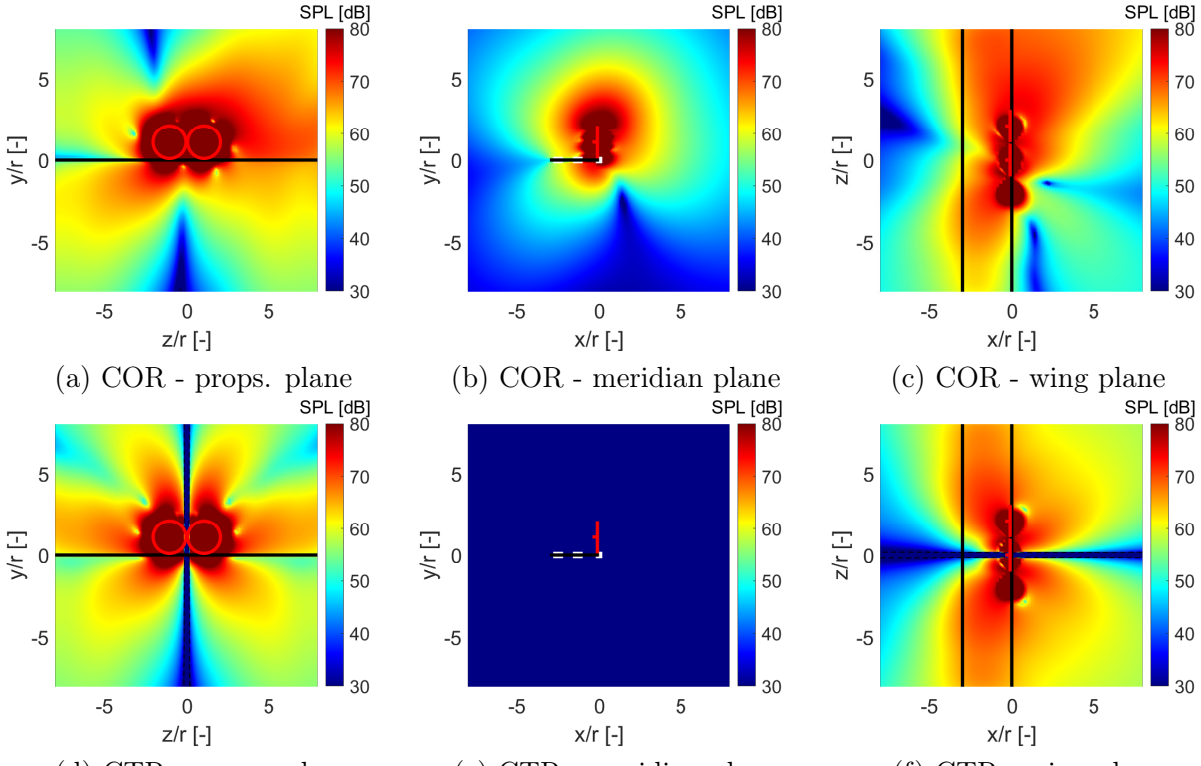

(a) COR - props. plane (b) COR - meridian plane (c) COR - wing plane

(d) CTR - props. plane (e) CTR - meridian plane (f) CTR - wing plane

Figure 5.22: Predicted sound-pressure level maps in relative decibels at the BPF in the configuration Min-ϕ30, for the COR/CTR propellers.

Finally, apart from the qualitative comparison maps, a more quantitative correlation is made in Figure 5.24 by plotting the analytical results alongside the experimental ones previously presented in Figure 3.47. As can be seen, the predicted sound has similar levels and global trends as the measured one for most of the comparison points. This suggests that the additional distortions around the wing, not considered in the analysis, do not play a dominant role. The pylon-induced distortion remains dominant.

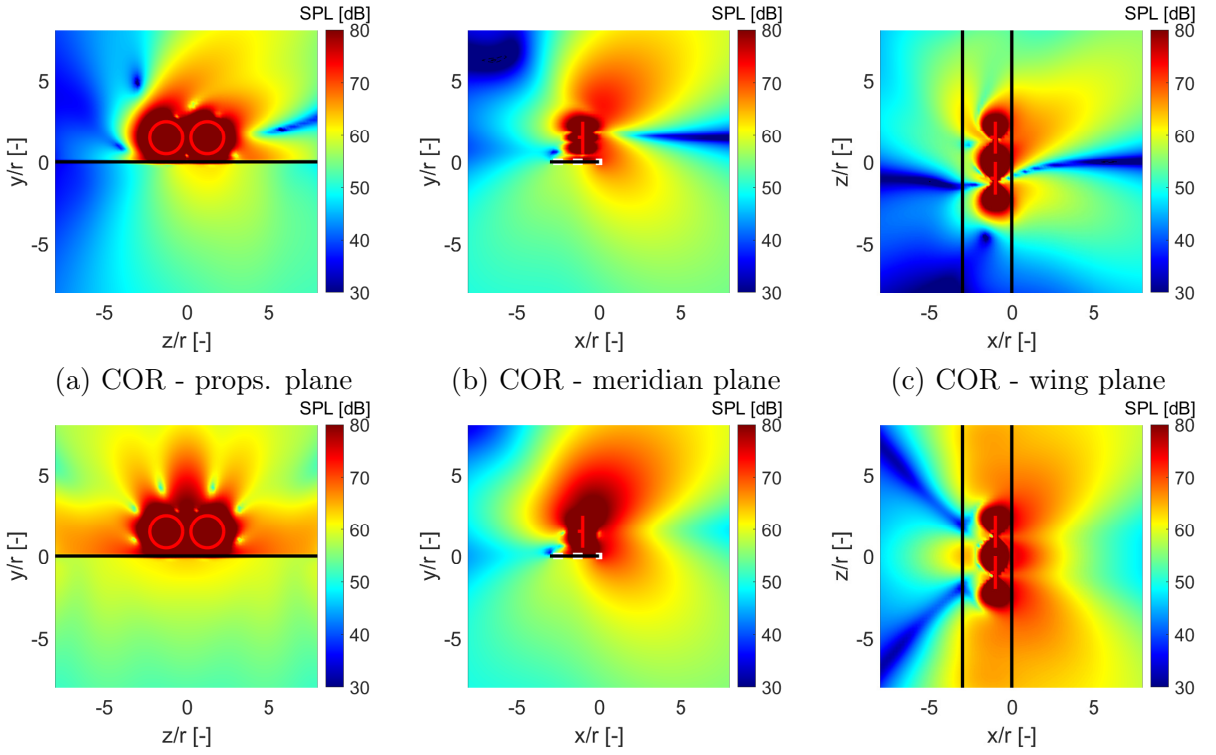

(a) COR - props. plane (b) COR - meridian plane (c) COR - wing plane

(d) CTR - props. plane (e) CTR - meridian plane (f) CTR - wing plane

Figure 5.23: Predicted sound-pressure level maps in relative decibels at the BPF in the configuration Max-ϕ0, for the COR/CTR propellers.

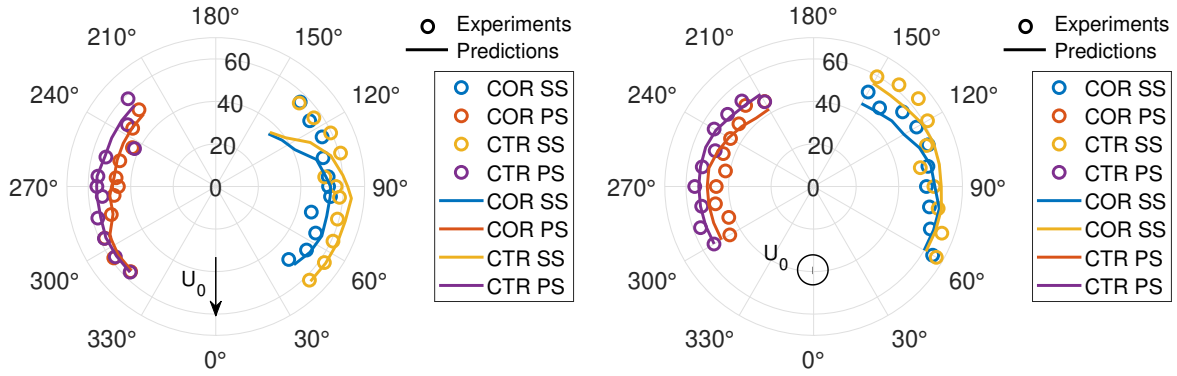

(a) Plane parallel to the wing airfoil (b) Plane parallel to the propeller discs

Figure 5.24: Experimental and analytical 2D directivity patterns of the 1st BPF (700 Hz) in Max-ϕ0 configurations, for CTR and COR arrangements. SS: suction side and PS: pressure side.

Yet clear under-estimates are also evidenced in the suction side of the directivity plots in the horizontal plane (Figure 5.24(a)), and some less critical discrepancies remain (for instance, in the range 120° to 150° in Figure 5.24(b)). This could be attributed to various vauses. Firstly, regarding the experiments, the results on the antenna position points 115°, 125° and 135° could probably be contaminated by sound scattering at the edges of the diffuser. It is worth mentioning that because of the position of the antenna, the diffuser does not affect the pressure side measurements (see Figure 3.14(b)). Secondly, this could be also related to some extinction zones abusively predicted with the simplified half-plane Green's function. Finally, it is not excluded that the aforementioned ignored wing-flow distortion becomes dominant at some observation angles.

Completed predictions could be achieved in a future work, for instance using mean-flow simulations in the presence of the wing, once available. However, it is still positive that all observed relative variations are comparable to those measured. In particular, the same difference between COR and CTR cases is observed with both approaches for the complete directivity pattern.

This chapter has analyzed the importance of calculating both, steady-loading and unsteady-loading noise contributions to obtain the total noise in a typical DEP configuration. Additionally, the analytical model was used to perform parametric calculations of the sound produced by different configurations. The main trends have been found to agree with the wind-tunnel tests. The next chapter summarizes the main findings of this investigation alongside the concluding remarks.

6 Concluding Remarks and Way Forward

Summary

The chapter summarizes the outcomes of the presented thesis. First, a summary of the analytical analyses and the experimental tests is found in section 6.1. The main findings and conclusions are depicted in section 6.2. Finally, opportunities for future extensions of the work are given in section 6.3.

Contents

6.1 Methodology

As part of the European Union's Horizon 2020 research and innovation program ENODISE project [93], the present investigation, done in the Fluid Mechanics and Acoustics Laboratory of *École Centrale de Lyon*, was aimed to understand the flow features and sound-scattering phenomena involved in a generic configuration of wing-propeller architecture for DEP systems, in order to search for an optimum configuration, both in terms of acoustic signature and of aerodynamic efficiency. To achieve the expected results, some intermediary objectives have been defined:

The first part of this work was dedicated to improving the understanding of underlying mechanisms for noise mitigation, and to assessing the ability of the experimental approach to determine optimized configurations, from both aerodynamic and acoustic standpoints. The configuration includes two co-rotating (COR) or contra-rotating (CTR), six-bladed propellers installed above an instrumented lifting wing of a large aspect ratio, close to the trailing edge. Aerodynamic and acoustic measurements have been performed, aimed at assessing the effects of installation parameters on tonal and broadband noise, and on aerodynamic performances. In particular, attention was paid to the positioning of the propellers in terms of distances to the wing surface and to the trailing edge, to the separation between the propellers, and to their phasing in terms of relative blade angular shift. Two advance ratios were investigated, zero and 0.95, and two propeller materials were tested, metal and ceramic.

Additionally, an analytical approach was developed to investigate fundamental features of

the tonal noise radiated by propellers installed on a rectangular wing by combining various analytical models. The focus was on relatively low frequencies, typically first multiples of the blade-passing frequency, representative of future distributed electric propulsion architectures. This technological context implies blades operating close to the rear part of the wing, possibly including interaction with a wake-like distortion. A two-step analytical prediction method has been proposed. The first step is the calculation of the free field from the blade forces, based on a blade segmentation technique. Steady-loading noise and unsteady-loading noise sources are estimated from the blade-element momentum theory and linearized unsteady-aerodynamic theories, respectively, for each segment. The second step is the calculation of the sound scattering by the trailing edge of the wing, starting from the exact half-plane Green's function for the convected Helmholtz equation in a uniformly moving fluid. For this, an approximate finite-chord correction to the Green's function has been proposed. Sound generation and scattering models are coupled by replacing the true, rotating sources with equivalent circular distributions of stationary phased dipoles, called source-modes.

6.2 Main Findings

Different parameters have been found to produce dominant effects on various aerodynamic or acoustic quantities, important for the identification of either detrimental or beneficial configurations. The streamwise distance D from the propeller plane to the trailing edge is the only common critical parameter, for both aerodynamic performances and noise. The normal distance from the propeller axis to the wing surface h mainly affects the wing C_p distribution and lift. The axis-to-axis distance d between the propellers mainly affects their thrust, whereas their relative phase angle ϕ has a significant effect on the far-field sound. It is important to state that the best configuration regarding the aerodynamic performances is detrimental to the acoustic signature, and *vice versa*. In particular, sound radiation is strongly increased when the blade tips operate close to the trailing edge; in the same conditions, both the wing lift and propeller thrust reach their maximum, for fixed advance ratio and rotational speed.

More quantitatively, depending on the positions of the propellers, in the COR cases, the lift coefficient of the wing can be increased by up to 30%, compared to the wing-alone configuration, and the thrust of one of the propellers can be up to 45% higher than in the case of only one propeller without the wing. For the CTR propellers, there is an additional increase in both, wing lift coefficient and propellers' thrust up to 7% regarding the same COR configurations. Furthermore, ceramic propellers produce around 10% less wing C_p and generate up to 30% less force for the same configurations with metal blades.

Sound reductions, mainly by masking, of up to 5 dB in the overall sound pressure level and 20 dB at the blade passing frequency, were observed with COR propellers. The results also indicate that the installation effect is very crucial for tonal propeller noise, leading to either masking or regeneration of sound for noise exposure on the ground, depending on propeller positions above the wing. This high sensitivity to the parameters confirms that the present experiment is relevant for the parametric investigation. In addition, the CTR cases present broadband noise reduction whereas the BPF tones increase by up to 10 dB, which confirms what was found in the literature about the greater noise reduction potential from COR rotors regarding CTR ones. Ceramic blades were as expected, quieter than the metal propellers regarding the first BPF tone, as the aerodynamic performance is affected by the behavior of the material at the selected RPM, probably because of deformation.

Moving on now to consider the analytical and given its partially approximate character, it has been assessed against numerical simulations performed with FEM software in 2D and 3D. The analytical and numerical predictions of a zero-thickness flat plate were found in good agreement. Furthermore, the FEM simulations exhibited small differences between a flat plate and a true airfoil shape of 12% thickness for sources close to the trailing edge. This makes the analytical model an attractive and reliable tool for fast and repeated calculations in an optimization process, as long as variations in terms of decibels are considered.

A key outcome is that source-modes that would be evanescent in free-field can be converted into very effectively radiating patterns if their radii, thus the blade tips of the installed propellers, are at a compact distance from the wing trailing edge. In particular, steady-loading noise involving rotor-locked modes enters this category. This detrimental effect of installing propellers over a wing could balance some other beneficial ones in future distributed propulsion systems. Indeed, for instance, the wing-propeller vicinity possibly reduces drag by compensating for the velocity deficit in the wake or the boundary layers. Moreover, an over-the-wing installation makes some masking expected for noise exposure on the ground. The present results suggest that the amplification by compact scattering leads to reconsidering the competition between steady-loading and unsteady-loading noise contributions. The propeller-pylon flow distortion generates specific efficient source modes in free-field. However, steady-loading noise is most often of secondary importance compared to unsteady-loading noise. Estimation of the BLH as sources of noise can be performed either from the velocity field or from blade forces data. Finally, similar results in terms of absolute sound levels and, even more importantly, relative variations were found in the analytical predictions and the measurements. Therefore, the analytical tools presented in the thesis are believed to be a very efficient way of quantifying these combined effects at the early design stage.

The study was aimed at producing a database, usable for finding an optimum configuration, rather than directly proposing an optimum. Indeed, the definition of the latter is a multi-disciplinary end-user task, for which criteria must be defined, leading to some relevant aeroacoustic cost function. This is a matter of possible future work. The database is also now available for the validation of numerical prediction strategies.

Having concluded the findings of the investigation, the final section of this work addresses the way forward to improve the obtained results.

6.3 Perspectives

Experimental and analytical perspectives are numerous for such an investigation. Each of them has not only its limitations but also possibilities for improvement.

Concerning the wind tunnel test, a large-scale setup including a wing of extensive chord and more propellers of bigger diameter will bring accurate aerodynamic and acoustic results. This will also help to advance the DEP configurations to a higher TRL.

Regarding the analytical model, there are several corrections to obtain accurate comparisons with measurements, which are listed in the following.

The sound propagation from the sources to a far-field microphone includes sound convection inside the nozzle-jet flow and propagation in the air at rest outside. The refraction through the jet shear layer is known to deviate sound propagation, therefore the measurement angle does not

coincide with the true emission angle. This is an issue when comparing the measurements to predictions based on an analytical model assuming a flow of infinite extent, for which only the total angle is involved. To cope with this issue, measurements performed in open-jet wind tunnels are often corrected, typically to determine sound-refraction corrections for shear-layer refraction to be able to compare what is measured at a given microphone position. In the literature can be found some models to account for sound-refraction corrections [194, 99] but recently another way of assessing the shear-layer refraction by the lateral nozzle-jet shear layer was described by applying the Kirchhoff's integral theorem [195]. It assimilates the shear layer to a plane interface of arbitrary extent completed by a sphere at infinity and is based on Kirchhoff's integral formulation. In view of the presently obtained agreement between measurements and predictions, the corrections are not essential. They would probably be at higher Mach numbers.

Finally, it is also important to model the flow distortion instead of using numerical information. An analytical potential-interaction noise model assimilating the pylon to an equivalent cylinder will allow the calculation of the BLH analytically. There are already available previous studies using this modeling for drones (rotor-support interaction) [76] and shrouded helicopters (tail-rotor interaction) [86]. Modal expansion of wing-flow distortions and/or wake velocity deficit for other installation effects can also be computed for correcting the current model [196]. Having a full analytical model will be a faster way to assess the noise from DEP configurations while accounting for flow distortions.

Bibliography

[1] ATAG. Aviation benefits beyond borders 2020. *Technical report*, 2020.

[2] ICAO. Icao long-term traffic forecasts. *Technical report*, 2018.

[3] Airbus. Global market forecast: Cities, airports & aircraft 2019-2038. *Technical report*, 2019.

[4] EASA-EEA. European aviation environmental report 2019. *Technical report*, 2019.

[5] European-Commission. Flightpath 2050: Europe's vision for aeronautics. maintaining global leadership & serving society's needs. *Report of the High Level Group on Aviation Research*, 2011.

[6] International Air Transport Association. Aircraft technology roadmap to 2050. *IATA report*, 2019.

[7] ICAO. Environmental report 2019: Aviation and environment. *Technical report*, 2019.

[8] Alan H. Epstein. Aeropropulsion for commercial aviation in the twenty-first century and research directions needed. *AIAA Journal*, 52(5):901–911, 2014.

[9] Kay O. Ploetner, Raoul Rothfeld, Marcia Urban, Mirko Hornung, Gilbert Tay, and Oluwaferanmi Oguntona. Technological and operational scenarios on aircraft fleet-level towards atag and iata 2050 emission targets. In *17th AIAA Aviation Technology, Integration, and Operations Conference*. Denver, United States, 2017.

[10] Hyun D. Kim, Aaron T. Perry, and Phillip J. Ansell. A review of distributed electric propulsion concepts for air vehicle technology. In *2018 AIAA/IEEE Electric Aircraft Technologies Symposium (EATS)*, pages 1–21. IEEE, 2018.

[11] Simon Watkins, Jane Burry, Abdulghani Mohamed, Matthew Marino, Samuel Prudden, Alex Fisher, Nicola Kloet, Timothy Jakobi, and Reece Clothier. Ten questions concerning the use of drones in urban environments. *Building and Environment*, 167:106458, 2020.

[12] Hyun Dae Kim. Distributed propulsion vehicles. In *27th International Congress of the Aeronautical Sciences*. Nice, France, 2010.

[13] Institut von Karman de Dynamique des Fluides. Grant agreement number 860103 — enodise. In *EUROPEAN COMMISSION - Innovation and Networks Executive Agency*, pages 1–283, 2019.

[14] Hyun Dae Kim, Gerald V. Brown, and James L. Felder. Distributed turboelectric propulsion for hybrid wing body aircraft. In *9th International Powered Lift Conference, London, United Kingdom*. Citeseer, 2008.

[15] Ning Qin, Armando Vavalle, Alan Le Moigne, M. Laban, K. Hackett, and P. Weinerfelt. Aerodynamic considerations of blended wing body aircraft. *Progress in Aerospace Sciences*, 40(6):321–343, 2004.

[16] Francesco Centracchio, Monica Rossetti, and Umberto Iemma. Approach to the weight estimation in the conceptual design of hybrid-electric-powered unconventional regional aircraft. *Journal of Advanced Transportation*, 2018, 2018.

[17] Russell H. Thomas, Yueping Guo, Jeffrey Berton, and Hamilton Fernandez. Aircraft noise reduction technology roadmap toward achieving the nasa 2035 goal. In *23rd AIAA/CEAS aeroacoustics conference*, page 3193, 2017.

[18] Laurie A. Garrow, Brian J. German, and Caroline E. Leonard. Urban air mobility: A comprehensive review and comparative analysis with autonomous and electric ground transportation for informing future research. *Transportation Research Part C: Emerging Technologies*, 132, 2021.

[19] Eric Greenwood, Kenneth S. Brentner, Robert F Rau, and Ze Feng Ted Gan. Challenges and opportunities for low noise electric aircraft. *International Journal of Aeroacoustics*, 21(5-7):315–381, 2022.

[20] EASA. Study on the societal acceptance of urban air mobility in europe 2021. *Technical report*, 2021.

[21] Benjamin J. Brelje and Joaquim R. R. A. Martins. Electric, hybrid, and turboelectric fixed-wing aircraft: A review of concepts, models, and design approaches. *Progress in Aerospace Sciences*, 104:1–19, 2019.

[22] CAA. Emerging aircraft technologies and their potential noise impacts. *Technical report - Civil Aviation Authority*, 2019.

[23] Jernej Drofelnik, Matej Andrejasic, Blaz Mocan, Tadej Kosel, Julien Christophe, Joachim N Dominique, Christophe F Schram, Antoine Hajczak, Corneliu Stoica, Raluca Balasa, et al. Measurement and modelling of aero-acoustic installation effects in tractor and pusher propeller architectures. In *AIAA Aviation Forum*, page 2301, 2021.

[24] ICAO. Environmental report 2022: Innovation for a green transition. *Technical report*, 2022.

[25] Ivan Terekhov. Assessing noise effects of the urban air transportation system. In *2018 AIAA/CEAS Aeroacoustics Conference*, page 2954, 2018.

[26] Michael Bauer. First assessment of community noise for a simulated scenario of new urban air traffic. In *International Congress on Sound and Vibration (ICSV)*, pages 7–11, Montréal, Canada, 2019.

[27] Damiano Casalino, Wouter C van der Velden, and Gianluca Romani. Community noise of urban air transportation vehicles. In *AIAA SciTech Forum*, page 1834, 2019.

[28] Vishwanath Bulusu, Valentin Polishchuk, and Leonid Sedov. Noise estimation for future large-scale small uas operations. In *INTER-NOISE and NOISE-CON Congress and Conference Proceedings*, volume 254, pages 864–871. Institute of Noise Control Engineering, 2017.

[29] Michael Bauer. Assessment of en-route noise by simulated scenarios for future urban air traffic. In *INTER-NOISE and NOISE-CON Congress and Conference Proceedings*, volume 261, pages 1002–1008. Institute of Noise Control Engineering, 2020.

[30] Michael Bauer. Community noise from urban air mobility (uam) and its control by traffic management. In *INTER-NOISE and NOISE-CON Congress and Conference Proceedings*, volume 263, pages 187–193. Institute of Noise Control Engineering, 2021.

[31] WHO. Environmental noise guidelines for the european region. *Report of the World Health Organization - Regional Office for Europe*, 2018.

[32] Stephen Morrell, Richard Taylor, and David Lyle. A review of health effects of aircraft noise. *Australian and New Zealand Journal of Public Health*, 21(2):221–236, 1997.

[33] Jean Hermetz, Michael Ridel, and Carsten Doll. Distributed electric propulsion for small business aircraft a concept-plane for key-technologies investigations. In *30th International Congress of the Aeronautical Sciences*, 2016.

[34] Andy Ko, Joseph A. Schetz, and William H. Mason. Assessment of the potential advantages of distributed-propulsion for aircraft. In *XVI International Symposium on Air Breathing Engines (ISABE)*. Citeseer, 2003.

[35] Athanasios Synodinos, Rod Self, and Antonio Torija. Preliminary noise assessment of aircraft with distributed electric propulsion. In *2018 AIAA/CEAS Aeroacoustics Conference*, page 2817, 2018.

[36] Andrew T Wick, John R Hooker, and Cale H Zeune. Integrated aerodynamic benefits of distributed propulsion. In *53rd AIAA Aerospace Sciences Meeting*, page 1500, 2015.

[37] Benjamin Choi, Gerald V. Brown, Carlos Morrison, and Timothy Dever. Propulsion electric grid simulator (pegs) for future turboelectric distributed propulsion aircraft. In *12th International Energy Conversion Engineering Conference*, page 3644, 2014.

[38] Benjamin B. Choi and Gerald Brown. Propulsion powertrain real-time simulation using hardware-in-the-loop (hil) for aircraft electric propulsion system. In *53rd AIAA/SAE/ASEE Joint Propulsion Conference*, page 4703, 2017.

[39] Kurt V. Papathakis, Kurt J. Kloesel, Yohan Lin, Sean Clarke, Jacob J. Ediger, and Starr Ginn. Design and development of a 200-kw turbo-electric distributed propulsion testbed. *AIAA Paper*, 4611, 2016.

[40] James Felder, Michael Tong, and Julio Chu. Sensitivity of mission energy consumption to turboelectric distributed propulsion design assumptions on the n3-x hybrid wing body aircraft. In *48th AIAA/ASME/SAE/ASEE Joint Propulsion Conference & Exhibit*, page 3701, 2012.

[41] Hyoungjin Kim and Meng-Sing Liou. Shape design optimization of embedded engine inlets for n2b hybrid wing-body configuration. *Aerospace Science and Technology*, 30(1):128–149, 2013.

[42] Jason Welstead and James L Felder. Conceptual design of a single-aisle turboelectric commercial transport with fuselage boundary layer ingestion. In *54th AIAA Aerospace Sciences Meeting*, page 1027, 2016.

[43] Airbus. Url: https://www.airbus.com/innovation/zero-emission/electric-flight/e-fan-x.html, Last accessed 16 September 2021.

[44] Brian Yutko, Neil Titchener, Christopher Courtin, Michael Lieu, Larry Wirsing, David Hall, John Tylko, Jeffrey Chambers, Thomas Roberts, and Clint Church. Design and development of the d8 commercial transport concept. In *31st Congress of the International Council of the Aeronautical Sciences, ICAS*. International Council of the Aeronautical Sciences, 2018.

[45] Alejandra Uranga, Mark Drela, Edward M Greitzer, David K Hall, Neil A Titchener, Michael K Lieu, Nina M Siu, Cécile Casses, Arthur C Huang, Gregory M Gatlin, et al. Boundary layer ingestion benefit of the d8 transport aircraft. *AIAA journal*, 55(11):3693–3708, 2017.

[46] Gianluca Romani, Qingqing Ye, Francesco Avallone, Daniele Ragni, and Damiano Casalino. Numerical analysis of fan noise for the nova boundary-layer ingestion configuration. *Aerospace Science and Technology*, 96:105532, 2020.

[47] Daniel C Mincu, Thomas Le Garrec, Stephanie Peron, and Marc Terracol. Immersed boundary conditions for high order caa solvers-aeroacoustics installation effects assessment. In *23rd AIAA/CEAS Aeroacoustics Conference*, page 3504, 2017.

[48] Peter Schmollgruber, Olivier Atinault, Italo Cafarelli, Carsten Döll, Christophe François, Jean Hermetz, Romain Liaboeuf, Bernard Paluch, and Michael Ridel. Multidisciplinary exploration of dragon: an onera hybrid electric distributed propulsion concept. In *AIAA Scitech Forum*, page 1585, 2019.

[49] Michael Ridel, Eric Nguyen Van, Tatiana Prosvirnova, David Donjat, Christel Seguin, and Philippe Choy. Dragon: hybrid electrical architecture for distributed fans propulsion. In *MEA 2021*, 2021.

[50] Benjamin Schiltgen, Michael Green, Andrew Gibson, David Hall, Darold Cummings, and Craig Hange. Benefits and concerns of hybrid electric distributed propulsion with conventional electric machines. In *48th AIAA/ASME/SAE/ASEE Joint Propulsion Conference & Exhibit*, page 3769, 2012.

[51] Michael Green, Benjamin Schiltgen, and Andrew Gibson. Analysis of a distributed hybrid propulsion system with conventional electric machines. In *48th AIAA/ASME/SAE/ASEE Joint Propulsion Conference & Exhibit*, page 3768, 2012.

[52] Eviation. Url: https://www.eviation.com/, Last accessed 07 March 2022.

[53] Zunum-Aero. Url: https://zunum.aero/, Last accessed 16 September 2021.

[54] EAG. Url: https://www.electricaviationgroup.com/, Last accessed 12 October 2022.

[55] Nicholas K. Borer, Michael D. Patterson, Jeffrey K. Viken, Mark D. Moore, JoeBen Bevirt, Alex M Stoll, and Andrew R Gibson. Design and performance of the nasa sceptor distributed electric propulsion flight demonstrator. In *16th AIAA Aviation Technology, Integration, and Operations Conference*, page 3920, 2016.

[56] Karen A Deere, Jeffrey K Viken, Sally Viken, Melissa B Carter, Michael Wiese, and Norma Farr. Computational analysis of a wing designed for the x-57 distributed electric propulsion aircraft. In *35th AIAA applied aerodynamics conference*, page 3923, 2017.

[57] Airbus. Url: https://www.airbus.com/innovation/zero-emission/urban-air-mobility/cityairbus.html, Last accessed 16 September 2021.

[58] EHANG. Url: http://www.ehang.com/ehang184, Last accessed 16 September 2021.

[59] Volocopter. Url: https://www.volocopter.com, Last accessed 16 September 2021.

[60] Lift. Url: https://www.liftaircraft.com/, Last accessed 12 October 2022.

[61] Embraer. Url: https://embraerx.embraer.com/global/en, Last accessed 16 September 2021.

[62] Aurora-Flight-Sciences. Url: https://www.aurora.aero/urban-air-mobility/, Last accessed 16 September 2021.

[63] Uber. Url: https://www.uber.com/us/en/elevate/, Last accessed 12 October 2022.

[64] Wisk. Url: https://wisk.aero/, Last accessed 16 September 2021.

[65] Opener aero. Url: https://www.opener.aero/, Last accessed 16 September 2021.

[66] Airbus. Url: https://www.airbus.com/innovation/zero-emission/urban-air-mobility/vahana.html, Last accessed 16 September 2021.

[67] Airbus. Url: https://www.airbus-sv.com/projects/1, Last accessed 16 September 2021.

[68] Lilium. Url: https://lilium.com/technology, Last accessed 16 September 2021.

[69] Alex M. Stoll, Edward V. Stilson, JoeBen Bevirt, and Percy P. Pei. Conceptual design of the joby s2 electric vtol pav. In *14th AIAA Aviation Technology, Integration, and Operations Conference*, page 2407, 2014.

[70] Vertical-Aerospace. Url: https://vertical-aerospace.com/vx4/, Last accessed 16 September 2021.

[71] Bell. Url: https://www.bellflight.com/products/bell-nexus, Last accessed 12 October 2022.

[72] Aurora-Flight-Science. Url: https://www.aurora.aero/lightningstrike, Last accessed 16 September 2021.

[73] Patrick C. Murphy and Drew Landman. Experiment design for complex vtol aircraft with distributed propulsion and tilt wing. In *AIAA Atmospheric Flight Mechanics Conference*, page 0017, 2015.

[74] Alessandro Bacchini and Enrico Cestino. Electric vtol configurations comparison. *Aerospace*, 6(3):26, 2019.

[75] Xingyu Zhang, Wei Zhang, LI Weilin, Xiaobin Zhang, and LEI Tao. Experimental research on aero-propulsion coupling characteristics of a distributed electric propulsion aircraft. *Chinese Journal of Aeronautics*, 36(2):201–212, 2023.

[76] Michel Roger and Stéphane Moreau. Tonal-noise assessment of quadrotor-type uav using source-mode expansions. In *Acoustics*, volume 2, pages 674–690. Multidisciplinary Digital Publishing Institute, 2020.

[77] Gianluca Romani, Edoardo Grande, Francesco Avallone, Daniele Ragni, and Damiano Casalino. Performance and noise prediction of low-reynolds number propellers using the lattice-boltzmann method. *Aerospace Science and Technology*, 125:107086, 2022.

[78] Antoine Hajczak, Julien Christophe, Cansev Y Kucukosman, and Christophe F Schram. Numerical parametric investigation of aeroacoustic installation effects in a distributed electric propulsion system. In *28th AIAA/CEAS Aeroacoustics Conference*, page 3006, 2022.

[79] Nur Syafiqah Jamaluddin, Alper Celik, Kabilan Baskaran, Djamel Rezgui, and Mahdi Azarpeyvand. Experimental characterisation of small-scaled propeller-wing interaction noise. In *28th AIAA/CEAS Aeroacoustics Conference*, page 2973, 2022.

[80] Chaitanya C. Paruchuri, Deepak C. Akiwate, Sergi Palleja-Cabre, Amin Karimian, Phillip Joseph, and Anthony Parry. Investigation into the mechanisms of propeller-wing interaction noise. In *28th AIAA/CEAS Aeroacoustics Conference*, page 2936, 2022.

[81] Federico Petricelli, Sergi Palleja-Cabre, Chaitanya C Paruchuri, Phillip Joseph, Amin Karimian, Stefano Meloni, and Roberto Camussi. On the effect of inflow distortions of propeller noise. In *28th AIAA/CEAS Aeroacoustics 2022 Conference*, page 2938, 2022.

[82] Seyed Mohsen Alavi Moghadam, Jürgen Dierke, Michael Moessner, Roland Ewert, and Jan Delfs. A mid-to-high fidelity aerodynamic noise simulation framework for installed propeller configurations. In *28th AIAA/CEAS Aeroacoustics Conference*, page 3007, 2022.

[83] Federico Petricelli, Paruchuri Chaitanya, Sergi Palleja-Cabre, Stefano Meloni, Phillip F Joseph, Amin Karimian, Suresh Palani, and Roberto Camussi. An experimental investigation on the effect of in-flow distortions of propeller noise. *Applied Acoustics*, 214:109682, 2023.

[84] Michel. Roger, Daniel Acevedo-Giraldo, and Marc C. Jacob. Acoustic versus aerodynamic installation effects on a generic propeller-driven flying architecture. *Internationa Journal of Aeroacoustics*, 2022.

[85] Alessandro Zarri, Edoardo Dell'Erba, Wim Munters, and Christophe Schram. Aeroacoustic installation effects in multi-rotorcraft: Numerical investigations of a small-size drone model. *Aerospace Science and Technology*, 128:107762, 2022.

[86] Michel Roger and Korcan Kucukcoskun. Near-and-far field modeling of advanced tail-rotor noise using source-mode expansions. *Journal of Sound and Vibration*, 453:328–354, 2019.

[87] Liam P Hanson, Kabilan Baskaran, Bin Zang, and Mahdi Azarpeyvand. Aeroacoustic interactions of a trailing edge mounted propeller and flat plate. In *28th AIAA/CEAS Aeroacoustics 2022 Conference*, page 2937, 2022.

[88] Deepak C. Akiwate, Anthony Parry, Phillip Joseph, and Chaitanya C. Paruchuri. Analytical investigation of propeller-wing interaction noise. In *28th AIAA/CEAS Aeroacoustics Conference*, page 2877, 2022.

[89] Stephen A. Rizzi, Dennis L. Huff, David D. Boyd, Paul Bent, Brenda S. Henderson, Kyle A. Pascioni, D. Caleb Sargent, David L. Josephson, Mehmet Marsan, Hua Bill He, et al. Urban air mobility noise: Current practice, gaps, and recommendations. Technical report, NASA, 2020.

[90] Joe Posey, Ana Tinetti, and Mark Dunn. The low-noise potential of distributed propulsion on a catamaran aircraft. In *12th AIAA/CEAS Aeroacoustics Conference (27th AIAA Aeroacoustics Conference)*, page 2622, 2006.

[91] Daniel Acevedo Giraldo, Michel Roger, Marc C. Jacob, and Hadrien Beriot. Analytical study of the aerodynamic noise emitted by distributed electric propulsion systems. In *28th AIAA/CEAS Aeroacoustics 2022 Conference*, page 2830, 2022.

[92] Daniel Acevedo Giraldo, Michel Roger, and Marc C. Jacob. Experimental study of the aerodynamic noise of a pair of pusher-propellers installed over a wing. In *AIAA AVIATION 2023 Forum*, page 3359, 2023.

[93] ENODISE. Url: https://www.vki.ac.be/index.php/about-enodise, Last accessed 20 October 2022.

[94] Michael J. T. Smith. Aircraft noise. *Cambridge University Press*, 3, 1989.

[95] Harvey H. Hubbard. *Aeroacoustics of flight vehicles: theory and practice. Volume 1: Noise sources.* NASA, 1991.

[96] Harvey H. Hubbard. Aeroacoustics of flight vehicles: Theory and practice. volume 2: Noise control. Technical report, NASA, 1991.

[97] D. W. Kurtz and J. E. Marte. A review of aerodynamic noise from propellers, rotors, and lift fans. *NASA Technical Report*, 1970.

[98] William K Blake. Mechanics of flow-induced sound and vibration. volume 1 general concepts and elementary source. volume 2-complex flow-structure interactions. *Journal of Applied Mathematics*, 1, 1986.

[99] Stewart Glegg and William Devenport. *Aeroacoustics of low Mach number flows: fundamentals, analysis, and measurement.* Academic Press, 2017.

[100] Thomas F. Brooks, D. Stuart Pope, and Michael A. Marcolini. Airfoil self-noise and prediction. Technical report, NASA, 1989.

[101] K. Knowles. Importance of broadband noise for advanced turboprops. *Journal of Aircraft*, 24(6):386–391, 1987.

[102] Michel Roger and Stéphane Moreau. Back-scattering correction and further extensions of amiet's trailing-edge noise model. part 1: theory. *Journal of Sound and Vibration*, 286(3):477–506, 2005.

[103] S. Pröbsting and S. Yarusevych. Laminar separation bubble development on an airfoil emitting tonal noise. *Journal of Fluid Mechanics*, 780:167–191, 2015.

[104] Thomas Node-Langlois, Fabien Wlassow, Vianney Languille, Yann Colin, Bastien Caruelle, James R. Gill, Xiaoxian Chen, Xin Zhang, and Anthony B Parry. Prediction of contra-rotating open rotor broadband noise in isolated and installed configurations. In *20th AIAA/CEAS Aeroacoustics Conference*, page 2610, 2014.

[105] A. McAlpine and Michael J. Kingan. Far-field sound radiation due to an installed open rotor. *International Journal of Aeroacoustics*, 11(2):213–245, 2012.

[106] John E. Ffowcs Williams and David L. Hawkings. Sound generation by turbulence and surfaces in arbitrary motion. *Philosophical Transactions of the Royal Society of London. Series A, Mathematical and Physical Sciences*, 264(1151):321–342, 1969.

[107] Edmane Envia. Contra-rotating open rotor tone noise prediction. In *20th AIAA/CEAS Aeroacoustics Conference*, page 2606, 2014.

[108] H. Yu Yung. Rotor blade–vortex interaction noise. *Progress in Aerospace Sciences*, 36(2):97–115, 2000.

[109] Michael Kingan and Rod Self. Counter-rotation propeller tip vortex interaction noise. In *15th AIAA/CEAS Aeroacoustics Conference (30th AIAA Aeroacoustics Conference)*, page 3135, 2009.

[110] David Coleman, Atanu Halder, Farid Saemi, Carl Runco, Hunter Denton, Bochan Lee, and M. Benedict. Development of "aria", a compact, ultra-quiet personal electric helicopter. In *77th Annual Vertical Flight Society Forum and Technology Display*, pages 10–14, 2021.

[111] Thomas F. Brooks, Michael A. Marcolini, and D. Stuart Pope. Main rotor broadband noise study in the dnw. *Journal of the American Helicopter Society*, 34(2):3–12, 1989.

[112] Dhwanil Shukla and Narayanan Komerath. Multirotor drone aerodynamic interaction investigation. *Drones*, 2(4):43, 2018.

[113] Wenwu Zhou, Zhe Ning, Haixing Li, and Hui Hu. An experimental investigation on rotor-to-rotor interactions of small uav propellers. In *35th AIAA applied aerodynamics conference*, page 3744, 2017.

[114] Charles E. Tinney and Jayant Sirohi. Multirotor drone noise at static thrust. *AIAA Journal*, 56(7):2816–2826, 2018.

[115] Ryan McKay and Michael J. Kingan. Multirotor unmanned aerial system propeller noise caused by unsteady blade motion. In *25th AIAA/CEAS Aeroacoustics Conference*, page 2499, 2019.

[116] Charles F. Wisniewski, Aaron Byerley, Kenneth W. Van Treuren, and Andrew Hays. Experimentally testing commercial and custom designed quadcopter propeller static performance and noise generation. In *23rd AIAA/CEAS Aeroacoustics Conference*, page 3711, 2017.

[117] Andreas Peters and Zoltan S Spakovszky. Rotor interaction noise in counter-rotating propfan propulsion systems. *Journal of Turbomachinery*, 2012.

[118] Arne Stuermer and Jianping Yin. Aerodynamic and aeroacoustic installation effects for pusher-configuration cror propulsion systems. In *28th AIAA Applied Aerodynamics Conference*, page 4235, 2010.

[119] Patricia Ventura Diaz, Rafael Caracuel Rubio, and Seokkwan Yoon. Simulations of ducted and coaxial rotors for air taxi operations. In *AIAA Aviation Forum*, page 2825, 2019.

[120] Donald B. Hanson. Noise of counter-rotation propellers. *Journal of Aircraft*, 22(7):609–617, 1985.

[121] Arnulfo Carazo, Michel Roger, and Magdi Omais. Analytical prediction of wake-interaction noise in counter-rotating open rotors. In *17th AIAA/CEAS aeroacoustics conference (32nd AIAA aeroacoustics conference)*, page 2758, 2011.

[122] Arnulfo Carazo Méndez. *Semi-analytical prediction of wake-interaction noise in counter-rotating open rotors*. PhD thesis, Ecully, Ecole centrale de Lyon, 2012.

[123] Anupam Sharma and Hsuan-nien Chen. Prediction of aerodynamic tonal noise from open rotors. *Journal of Sound and Vibration*, 332(16):3832–3845, 2013.

[124] P. J. W. Block. Noise radiation patterns of counter-rotation and unsteadily loaded single-rotation propellers. *Journal of Aircraft*, 22(9):776–783, 1985.

[125] James H. Stephenson, Natasha L. Schatzman, Benny K. Cheung, Nikolas S. Zawodny, D. Caleb Sargent, and B. W. Sim. Aeroacoustic measurements from the aerodynamic and acoustic rotorprop test (aart) in the national full-scale aerodynamic complex (nfac) 40- by 80-foot wind tunnel. In *Vertical Flight Society International 77th Annual Forum & Technology Display*, pages 10–14, 2021.

[126] R. T. Johnston and J. P. Sullivan. Unsteady wing surface pressures in the wake of a propeller. In *30th Aerospace Sciences Meeting & Exhibit*, pages 644–651, 1992.

[127] Antonio Pagano, Mattia Barbarino, Damiano Casalino, and Luigi Federico. Tonal and broadband noise calculations for aeroacoustic optimization of a pusher propeller. *Journal of Aircraft*, 47(3):835–848, 2010.

[128] Nikolas S. Zawodny and Douglas D. Boyd. Investigation of rotor-airframe interaction noise associated with small-scale rotary-wing unmanned aircraft systems. *Journal of the American Helicopter Society*, 65(1):1–17, 2020.

[129] Giulia Chirico, George N Barakos, and Nicholas Bown. Numerical aeroacoustic analysis of propeller designs. *The Aeronautical Journal*, 122(1248):283–315, 2018.

[130] Yeongmin Jo, Thierry Jardin, Romain Gojon, Marc C. Jacob, and Jean-Marc Moschetta. Prediction of noise from low reynolds number rotors with different number of blades using a non-linear vortex lattice method. In *25th AIAA/CEAS Aeroacoustics Conference*, page 2615, 2019.

[131] Joon W. Lim. Fundamental investigation of proprotor and wing interactions in tiltrotor aircraft. In *75th Annual Vertical Flight Society Forum and Technology Display, Philadelphia, PA, USA*, pages 13–16, 2019.

[132] Jianhua Zhang, Kenneth S. Brentner, and Edward C. Smith. Prediction of the aerodynamic and acoustic impact of propeller-wing interference. In *Aeromechanics for Advanced Vertical Flight Technical Meeting 2020, Held at Transformative Vertical Flight 2020*, pages 452–463. Vertical Flight Society, 2020.

[133] Elina Cros, Michel Roger, and Gilles Serre. On the very low frequency scattering of propeller noise by a neighboring cylinder. In *AIAA Aviation Forum*, page 2251, 2021.

[134] Michael S. Howe. *Theory of vortex sound*. Cambridge University Press, 2003.

[135] Dale A Smith, Antonio Filippone, and Nicholas Bojdo. A parametric study of counter rotating open rotor noise. In *25th AIAA/CEAS Aeroacoustics Conference*, page 2570, 2019.

[136] Michel Roger. On combined propeller synchronization and edge scattering for the noise reduction of distributed propulsion systems. In *26th International Congress on Sound and Vibration, Montreal, Canada*, pages 7–11, 2019.

[137] Daniel Weitsman and Eric Greenwood. Parametric study of evtol rotor acoustic design trades. In *AIAA SciTech Forum*, page 1987, 2021.

[138] Nando van Arnhem, Reynard de Vries, Tomas Sinnige, Roelof Vos, Georg Eitelberg, and Leo LM Veldhuis. Engineering method to estimate the blade loading of propellers in nonuniform flow. *AIAA Journal*, 58(12):5332–5346, 2020.

[139] Reynard de Vries, Nando van Arnhem, Tomas Sinnige, Roelof Vos, and Leo L.M. Veldhuis. Aerodynamic interaction between propellers of a distributed-propulsion system in forward flight. *Aerospace Science and Technology*, 118:107009, 11 2021.

[140] Jochen Wild. Mach and reynolds number dependencies of the stall behavior of high-lift wing-sections. *Journal of Aircraft*, 50(4):1202–1216, 2013.

[141] Weerg. Url: https://www.weerg.com/guides/what-is-resin-3d-printing, Last accessed 04 December 2022.

[142] BASF Forward AM. Url: https://forward-am.com/material-portfolio/ultracur3d-photopolymers/rigid-line/ultracur3d-rg-3280/, Last accessed 04 December 2022.

[143] Michel Roger, Stéphane Moreau, and Korcan Kucukcoskun. On sound scattering by rigid edges and wedges in a flow, with applications to high-lift device aeroacoustics. *Journal of Sound and Vibration*, 362:252–275, 2016.

[144] M. Sunyach, B. Bruiel, and G. Comte-Bellot. Performance of the high-speed anechoic wind tunnel at lyon university. In *NASA Technical Memorandum*, 1986.

[145] Daniel Juve and Blanc-Benon Philippe. The acoustic center of ecole centrale de lyon from 1970 to today. In *Forum Acusticum*, page 2301, 2023.

[146] Alister Gleason D'souza, Joel I. Concessao, Jaimon Quadros, and Keith Williams. Study of aerofoil design parameters for low speed wind tunnel. *Journal of Mechanical Engineering and Automation*, 5:47–54, 2015.

[147] Zhixiong Li, Iman Moradi, Quyen Nguyen, Arash Karimipour, Masoud Afrand, Iskander Tlili, and Atilla Incecik. Three-dimensional simulation of wind tunnel diffuser to study the effects of different divergence angles on speed uniform distribution, pressure in outlet, and eddy flows formation in the corners. *Physics of Fluids*, 32(5):052006, 2020.

[148] Florian R. Menter. Two-equation eddy-viscosity turbulence models for engineering applications. *AIAA journal*, 32(8):1598–1605, 1994.

[149] M. H. Mohamed, A. M. Ali, and A. A. Hafiz. Cfd analysis for h-rotor darrieus turbine as a low speed wind energy converter. *Engineering Science and Technology, an International Journal*, 18(1):1–13, 2015.

[150] Suhas V. Patankar and D. Brian Spalding. A calculation procedure for heat, mass and momentum transfer in three-dimensional parabolic flows. *International Journal of Heat Mass Transfer*, pages 1787–1806, 1972.

[151] Bruel & Kjaer. Url: https://www.bksv.com/en/transducers/acoustic/microphones/special-microphones/4958, Last accessed 07 March 2022.

[152] Bruel & Kjaer. Url: https://www.bksv.com/en/transducers/acoustic/calibrators/sound-calibrator-4231, Last accessed 07 March 2022.

[153] National Instruments. Url: https://www.ni.com/fr-fr/support/model.pxi-4472.html, Last accessed 07 March 2022.

[154] National Instruments. Url: https://www.ni.com/fr-fr/support/model.pxi-1042q.html, Last accessed 07 March 2022.

[155] KIMO. Url: https://www.kimoinstruments.com/detail/pitot-tubes-type-l-npl-type-l-straight-, Last accessed 07 March 2022.

[156] Furnnes. Url: https://www.furness.com/product/fco560/, Last accessed 07 March 2022.

[157] Dantec Dynamics. Url: https://www.dantecdynamics.com/components/hot-wire-and-hot-film-probes/single-sensor-probes/gold-plated-wire/, Last accessed 8 March 2023.

[158] Dantec Dynamics. Url: https://www.dantecdynamics.com/solutions/fluid-mechanics/constant-temperature-anemometry-cta/streamline-pro/, Last accessed 8 March 2023.

[159] Kulite. Url: https://kulite.com/products/product-advisor/product-catalog/pressure-scanner-kmps-1-64/, Last accessed 07 March 2022.

[160] Futek. Url: https://www.futek.com/store/multi-axis-sensors/biaxial/torque-and-thrust-biaxial-sensor-MBA500, Last accessed 07 March 2022.

[161] Futek. Url: https://www.futek.com/store/instruments/analog-amplifier/strain-gauge-analog-amplifier-voltage-output-IAA100/FSH03863, Last accessed 07 March 2022.

[162] Noah H. Schiller, Kyle A. Pascioni, and Nikolas S. Zawodny. Tonal noise control using rotor phase synchronization. In *Vertical Flight Society Annual Forum and Technology Display*, page 12, 2019.

[163] Mengxue Shao, Yang Lu, Xice Xu, Shujun Guan, and Jiaxin Lu. Experimental study on noise reduction of multi-rotor by phase synchronization. *Journal of Sound and Vibration*, 539:18, 2022.

[164] John E. Ffowcs Williams and David L. Hawkings. Theory relating to the noise of rotating machinery. *Journal of Sound and Vibration*, 10(1):10–21, 1969.

[165] Michael James Lighthill. On sound generated aerodynamically i. general theory. *Royal Society of London. Series A. Mathematical and Physical Sciences*, 211(1107):564–587, 1952.

[166] N Curle. The influence of solid boundaries upon aerodynamic sound. *Royal Society of London. Mathematical and Physical Sciences*, 231(1187):505–514, 1955.

[167] M. V. Lowson. The sound field for singularities in motion. *Royal Society of London. Series A. Mathematical and Physical Sciences*, 286(1407):559–572, 1965.

[168] D. G. Crighton and F. G. Leppington. On the scattering of aerodynamic noise. *Journal of Fluid Mechanics*, 46(3):577–597, 1971.

[169] PE Doak. Acoustic radiation from a turbulent fluid containing foreign bodies. *Royal Society of London. Series A. Mathematical and Physical Sciences*, 254(1276):129–146, 1960.

[170] Michael S. Howe. Sound generation in a fluid with rigid boundaries. *Acoustics of Fluid-Structures Interactions*, pages 164–166, 1998.

[171] Alan Powell. Theory of vortex sound. *The Journal of the Acoustical Society of America*, 36(1):177–195, 1964.

[172] Michel Roger and Stéphane Moreau. Aeroacoustic installation effects in cooling fan systems part 1: Scattering by surrounding surfaces. In *International Symposium on Transport Phenomena and Dynamics of Rotating Machinery, Honolulu, HI, USA*, pages 17–22, 2008.

[173] Douglas Samuel Jones. Acoustic and electromagnetic waves. *Oxford/New York*, 1986.

[174] S. W. Rienstra. Sound diffraction at a trailing edge. *Journal of Fluid Mechanics*, 108:443–460, 1981.

[175] H. M. V. Macdonald. A class of diffraction problems. *London Mathematical Society*, 2(1):410–427, 1915.

[176] D. S. Jones. Aerodynamic sound due to a source near a half-plane. *Journal of Applied Mathematics*, 9(1):114–122, 1972.

[177] Ben Noble. *Methods based on the Wiener-Hopf technique for the solution of partial differential equations*, volume 332. Taylor & Francis US, 1958.

[178] Michael S. Howe. Edge-source acoustic green's function for an airfoil of arbitrary chord, with application to trailing-edge noise. *Journal of Mechanics and Applied Mathematics*, 54(1):139–155, 2001.

[179] Hadrien Bériot. Personal communication, 2022.

[180] Hadrien Bériot, Albert Prinn, and Gwénaél Gabard. Efficient implementation of high-order finite elements for helmholtz problems. *International Journal for Numerical Methods in Engineering*, 106(3):213–240, 2016.

[181] Hadrien Bériot and Gwénaél Gabard. Anisotropic adaptivity of the p-fem for time-harmonic acoustic wave propagation. *Journal of Computational Physics*, 378:234–256, 2019.

[182] Christophe Geuzaine and Jean-François Remacle. Gmsh: A 3-d finite element mesh generator with built-in pre-and post-processing facilities. *International journal for numerical methods in engineering*, 79(11):1309–1331, 2009.

[183] Hadrien Bériot and Axel Modave. An automatic perfectly matched layer for acoustic finite element simulations in convex domains of general shape. *International Journal for Numerical Methods in Engineering*, 122(5):1239–1261, 2021.

[184] Faisal Mahmuddin. Rotor blade performance analysis with blade element momentum theory. In *8th International Conference on Applied Energy*, pages 1123–1129. Elsevier, 2017.

[185] Jeremy Ledoux, Sebastián Riffo, and Julien Salomon. Analysis of the blade element momentum theory. *Journal of Applied Mathematics*, 81(6):2596–2621, 2021.

[186] Romain Gojon, Nicolas Doué, Hélène Parisot-Dupuis, Bertrand Mellot, and Thierry Jardin. Aeroacoustic radiation of a low reynolds number two-bladed rotor in interaction with a cylindrical beam. In *28th AIAA/CEAS Aeroacoustics Conference*, page 2972, 2022.

[187] Myles Morelli, Alberto Guardone, and Beckett Yx Zhou. Computational aeroacoustic analysis of a wing-tip mounted propeller and high-lift device. In *28th AIAA/CEAS Aeroacoustics Conference*, page 2939, 2022.

[188] Sophie Le Bras, Korcan Kucukcoskun, Daniel Acevedo Giraldo, and Michel Roger. Aeroacoustic simulations of a pylon-mounted propeller configuration at low reynolds number. In *Submitted to 30th AIAA/CEAS Aeroacoustics Conference*, 2024.

[189] Siemens Digital Industries Software. Simcenter star-ccm+. *Version 17.06.007-R8*, 2022.

[190] Franck Nicoud and Frédéric Ducros. Subgrid-scale stress modelling based on the square of the velocity gradient tensor. *Flow, turbulence, and Combustion*, 62(3):183–200, 1999.

[191] Marvin E Goldstein. Aeroacoustics. *New York*, 1976.

[192] Nelson H. Kemp and W. R. Sears. The unsteady forces due to viscous wakes in turbomachines. *Journal of the Aeronautical Sciences*, 22(7):478–483, 1955.

[193] Siemens Digital Industries Software. Simcenter nastran acoustics user's guide. *Version 2212*, 2023.

[194] Roy K. Amiet. Refraction of sound by a shear layer. *Journal of Sound and Vibration*, 58(4):467–482, 1978.

[195] Georgios Bampanis, Michel Roger, and Stéphane Moreau. On a three-dimensional investigation of airfoil turbulence-impingement noise and its reduction by leading-edge tubercles. *Journal of Sound and Vibration*, 520:116635, 2022.

[196] Michel Roger and Stéphane Moreau. Edge scattering of distributed sources – application to high-lift device noise. In *14th AIAA/CEAS Aeroacoustic Conference*, page 2866, 2008.

Public Dissemination

Journal Article

- Roger, M., **Acevedo-Giraldo, D.**, & Jacob, M. C. (2022). Acoustic versus aerodynamic installation effects on a generic propeller-driven flying architecture. International Journal of Aeroacoustics, 21(5-7), 585-609.
https://doi.org/10.1177/1475472X221107372

Conference Papers and Presentations

- **Acevedo-Giraldo, D.**, Roger, M., Jacob, M. C., & Beriot, H. (2022). Analytical study of the aerodynamic noise emitted by distributed electric propulsion systems. In 28th AIAA/CEAS Aeroacoustics Conference (p. 2830).
https://doi.org/10.2514/6.2022-2830

- **Acevedo-Giraldo, D.**, Roger, M., & Jacob, M. C. (2023). Experimental study of the aerodynamic noise of a pair of pusher-propellers installed over a wing. In AIAA AVIATION Forum (p. 3359).
https://doi.org/10.2514/6.2023-3359

- Le Bras S., Kucukcoskun K., **Acevedo-Giraldo, D.**, & Roger, M. (2024). Aeroacoustic simulations of a pylon-mounted propeller configuration at low-Reynolds number.
To be presented at the 30th AIAA/CEAS Aeroacoustics Conference.

Workshop Presentation

- **Acevedo-Giraldo, D.**, Roger, M., Jacob, M. C., Le Bras S., & Kucukcoskun K. (2023). Analytical study of the unsteady aerodynamic noise radiated by distributed electric propulsion systems. In DJINN-ENODISE workshop: Aeroacoustic Installation Effects in Conventional and New Aircraft Propulsion Systems.

Datasets

- **Acevedo-Giraldo, D.**, Roger, M., & Jacob, M. C. (2023). H2020 Enodise: Experimental dataset configuration B2 ECL. Zenodo.
https://doi.org/10.5281/zenodo.7925336

- **Acevedo-Giraldo, D.**, Roger, M., & Jacob, M. C. (2023). H2020 Enodise: Analytical dataset configuration B2 ECL. Zenodo.
https://doi.org/10.5281/zenodo.8182284

Curriculum Vitæ

Daniel ACEVEDO GIRALDO

Born March 26^{th} 1993 in Itagui, Colombia

https://linkedin.com/in/danielacevedogi/

WORK EXPERIENCE

2021 - 2024 **Doctoral Researcher**
École Centrale de Lyon. Écully, France
Department of Fluid Mechanics, Acoustics, and Energetic
European Union's Horizon 2020 project - ENODISE: enabling optimized disruptive airframe-propulsion integration concepts

2019 – 2020 **Research Engineer**
Kite Robotics - University of Twente. Enschede, The Netherlands
Department of Thermal and Fluid Engineering
European Union's Horizon 2020 project - HERO: highrise robot - safe and cost-effective window cleaning of skyscrapers by robots

2017 – 2019 **Research Assistant**
Embraer - University of São Paulo. São Carlos, Brazil
Department of Aeronautical Engineering
Brazilian aircraft project - SILENCE: solutions for integrating low external noise concepts

EDUCATION

2021 - 2024 **PhD in Acoustics**
École Centrale de Lyon. Écully, France
Thesis: Experimental and analytical investigation of the aerodynamic noise emitted by generic distributed electric propulsion wing-propellers configurations
Supervisors: Michel Roger and Marc C. Jacob

2017 – 2019 **MSc in Mechanical Engineering**
University of São Paulo. São Carlos, Brazil
Thesis: Experimental aeroacoustic and aerodynamic analysis of a large-scale flap side-edge model
Supervisor: Fernando M. Catalano

2016 **Aeronautical Engineering Exchange Program**
University of São Paulo. São Carlos, Brazil

2010 – 2016 **BSc in Aeronautical Engineering**
Pontifical Bolivarian University. Medellín, Colombia

dernière page de la thèse

AUTORISATION DE SOUTENANCE

Vu les dispositions de l'arrêté du 25 mai 2016 modifié par l'arrêté du 26 août 2022,

Vu la demande des directeurs de thèse

Messieurs M. ROGER et M. JACOB

et les rapports de

M. C. SCHRAM
Professeur - Institut Von Karman, VKI 72 Chaussée de Waterloo, 1640 Rhode-St-Genèse Belgique

et de

M. F. AVALLONE
Professeur - Politecnico Torino, Corso Castelfidardo, 39, 10129 Torino

Monsieur ACEVEDO GIRALDO Daniel

est autorisé à soutenir une thèse pour l'obtention du grade de **DOCTEUR**

Ecole doctorale Mécanique, Energétique, Génie Civil, Acoustique

Fait à Ecully, le 25 mars 2024

Pour le directeur de l'École Centrale de Lyon
Le directeur de la recherche

Christophe CORRE